Sustainable Feedstock to Acrylic Acid using H-Y zeolites

Master's Thesis

Ramin Majidov

Supervisors: **Prof. Dmitry Murzin,**

Associate Prof. Päivi Mäki-Arvela and Docent Narendra Kumar

Laboratory of Industrial Chemistry and Reaction Engineering

Faculty of Science and Engineering

Åbo Akademi University Turku/Åbo 2023, Finland

Abstract

Ramin Majidov	Sustainable feedstock to chemicals using H-Y zeolites
Master's Thesis	Carried out under the supervision of Professor Dmitry Murzin, Associate Professor Päivi Mäki-Arvela and Docent Narendra Kumar in the laboratory of Industrial Chemistry and Reaction Engineering (Teknisk kemi och reaktionsteknik), Åbo Akademi University, Åbo/Turku
Keynotes	Methyl lactate, lactic acid, methanol, zeolites, sugars, glucose transformations, catalyst characterizations

This academic master thesis focuses on the synthesis, characterization, and testing of H-Y zeolites as catalysts for the synthesis of methyl lactate from glucose. The objective of this work was to explore the potential of H-Y zeolites as catalysts for this reaction and to optimize their performance through various modifications.

The synthesis of H-Y zeolites was carried out using a hydrothermal method, and their structural characterization was done using X-ray diffraction (XRD) and scanning electron microscopy (SEM). The H-Y zeolites were modified using various methods such as dealumination, ion-exchange, and impregnation, and their properties were characterized using a range of techniques including Fourier transform infrared (FTIR) spectroscopy, nitrogen physisorption, and transmission electron microscopy (TEM).

The synthesized and modified H-Y zeolites were then tested as catalysts in the transformation of glucose to methyl lactate. The reaction conditions were optimized to achieve the maximum yield of methyl lactate. The performance of the catalysts was evaluated by measuring the conversion of glucose and selectivity and the yield of methyl lactate and other products.

The results demonstrated that the H-Y zeolites with the SiO_2/Al_2O_3 ratio 30, modified by Sn and K exhibited the highest performance resulting in 85% of yields and full conversions at 150 °C, 30 bar, 720 rpm with 0.9 g of the catalyst loading. The nitrogen physisorption analysis showed that

modification by Sn and K increased the surface area and pore volume of the zeolites, which may have contributed to their improved catalytic activity. The FTIR spectroscopy analysis revealed the importance of Lewis and Brønsted acid sites in the modified H-Y zeolites, which are known to be crucial for methyl lactate formation from glucose. A high Brønsted/Lewis acidity ratio is beneficial for the desired product. Moreover, absence of strong Brønsted and Lewis acid sites in the catalyst resulted in formation of more than 60% methyl lactate yield under the same reaction conditions.

Overall, this work demonstrates the immense potential of H-Y zeolites as effective catalysts in the transformation of glucose to methyl lactate. The comprehensive analysis of catalyst performance and the insights gained from various modifications pave the way for future research endeavors aimed at advancing the field of sustainable and efficient catalysis for biomass transformation.

Acknowledgements

I would like to express my sincere gratitude and appreciation to the following individuals and organizations who made significant contributions to this project.

Firstly, I extend my heartfelt appreciation to Åbo Akademi University (ÅAU) and Neste for their collaboration and support throughout this fascinating project. Their cooperation provided me with extensive knowledge and valuable experience.

I am deeply grateful to my supervisor, Prof. Dmitry Murzin, for sharing his profound knowledge and expertise in various courses such as chemical process/product technology and heterogeneous catalysis. His guidance and inspiration were instrumental in the successful completion of this work. I would like to express special thanks to Assoc. Prof. Päivi Mäki-Arvela for granting me the opportunity to embark on this marvelous project. Her continuous guidance and assistance were invaluable, and her openness to provide support whenever needed is deeply appreciated. I am also indebted to Docent Narendra Kumar for introducing me to the field of zeolites, from catalyst synthesis to characterization and testing. His kind guidance and mentorship played a significant role in expanding my knowledge and understanding.

I would like to acknowledge the Laboratory of Industrial Chemistry and Reaction Engineering at Åbo Akademi University, along with my colleagues, particularly Dr. Zuzana Vajglová, Dr. Atte Aho, and Dr. Kari Eränen, for their unwavering support and sharing their experience and knowledge.

I express my gratitude to Mr. Linus Silvander, Dr. Markus Peurla, Prof. Mika Lastusaari, and Dr. Robert Lassfolk for their invaluable assistance in characterizing the prepared catalysts. Their expertise greatly contributed to the success of this project.

Lastly, I want to express my deepest appreciation to my family and friends for their unwavering support and belief in me. Their encouragement and presence have been my pillar of strength, and without them, this achievement would not have been possible.

Sincerely,

Ramin Majidov

List of Tables

List of Figures

List of abbreviations

n/a	not available
AA	Acrylic acid
AIE	Alkaline ion exchange
BET	Brunauer-Emmett-Teller theory
CAGR	Compound annual growth rate
DCM	Dichloromethane
deAl	Dealuminated
DP	Deposition precipitation
EIM	Evaporation impregnation
FTIR	Fourier transform infrared spectroscopy
GC-MS	Gas chromatography-mass spectrometry
HMF	5-Hydroxymethylfurfural
IE	Ion exchange
LA	Lactic acid
LC	Liquid chromatography
ML	Methyl lactate
NMR	Nuclear magnetic resonance spectroscopy
PADA	Pyruvaldehyde dimethyl acetal
RT	Retention time
SAR	SiO_2/Al_2O_3 ratio
SEM	Scanning electron microscopy
SSA	Specific surface area
TEAOH	Tetraethyl ammonium hydroxide
TEM	Transmission electron microscopy
TMCS	Trimethylchlorosilane
TPD	Temperature programmed desorption
XRD	X-ray powder diffraction
Y	Faujasite

Table of Contents

1. Introduction

Tin-containing zeolites have demonstrated remarkable catalytic activity in a diverse range of Lewis acid-driven transformations involving various substrates[1]. These zeolites have been particularly effective in promoting reaction cascades leading to the production of γ-valerolactone or lactic acid/alkyl lactates, showcasing their exceptional catalytic performance across a wide array of chemical conversions. The focus on the latter transformation has intensified recently, driven by the quest for reliable and efficient chemo-catalytic routes for the production of lactic acid that can circumvent the challenges associated with its industrial production via fermentation[2]. The advancement of Sn-zeolite and its utilization in the one-pot conversion of sugar monosaccharides into alkyl lactates represent two significant breakthroughs in this field. However, research indicates that other Sn-containing zeolites, such as MWW or FAU-type zeolites, also exhibit notable catalytic activity in various transformations[3]. In fact, certain zeolite structures present more accessible and desirable options as starting materials for the synthesis of tin-containing zeolite catalysts, owing to their ease of preparation on a larger scale compared to other materials.

Lactic acid plays a pivotal role as an intermediate in the production of alkyl lactates, propylene glycol, propylene oxide, acrylic acid, and poly (lactic acid), making it a critical commodity chemical[4]. Its applications have been extended to various industries including food, medicine, cosmetics, and the growing interest in lactic acid-based biopolymers[1]. The lactic acid market was valued at USD 1.19 billion in 2021 and is projected to reach USD 3.35 billion by 2028, indicating a continuous surge in demand[5]. Traditionally, lactic acid is produced through fermentation using carbohydrates. However, the lactic acid obtained from this process is impure and the productivity is limited. It has been extensively documented that the conventional lactic acid production method, addressing engineering aspects and purification techniques, such as electrodialysis, is associated with fermentation-based lactic acid production[6]. There is a need for new catalytic processes to produce lactic acid efficiently from both carbohydrates and lignocellulosic materials, which are more abundant and cost-effective than carbohydrates. Hydrothermal crystallization techniques have been employed to synthesize defect-free tin-containing zeolites, but these processes are challenging and time-consuming, leading to limitations in metal loading and formation of large zeolite particles that hinder diffusion of reactants and products[3]. Dealumination and/or desilication

of the starting zeolite followed by metalation, which is a common post-synthesis zeolite metalation procedure, involves the creation of vacancies within the crystal framework that can be occupied by metal species[7].

Despite the wide range of applications and available resources concerning Sn-Beta zeolites, limited investigations have been conducted on Y zeolites. The distinctiveness of this study lies in the underexplored nature of USY zeolites, which captures attention and distinguishes it from existing research.

1.1. Short literature review

Sustainable chemistry is becoming increasingly important when mitigating the challenges of climate change and environmental degradation. In this context, one promising approach is the use of renewable feedstock to produce valuable chemicals and materials. Methyl lactate is one such chemical that has received attention due to its potential as a green solvent, a fuel additive, and an intermediate for the synthesis of other chemicals.

In the recent years, there has been growing interest in the use of Y zeolites as catalysts for the tranformation of sugars into methyl lactate. Y zeolites are a type of microporous aluminosilicate material with a high surface area and acidity, which make them suitable for a variety of catalytic applications. The use of Y zeolites in the transformation of sugars to methyl lactate has several advantages, including high yields, selectivity, and recyclability, as well as the ability to use a variety of sugar feedstocks.

Several studies have investigated the use of different types of Y zeolites in the synthesis of methyl lactate from sugars reporting a series of Y zeolites with different Si/Al ratios and their performance in the transformations of glucose to methyl lactate. It was found that the Si/Al ratio had a significant effect on the activity and selectivity of the catalyst, with a Si/Al ratio of 10 resulting in the highest methyl lactate yield of 46.6% at 160 °C[8]. Furthermore, the addition of a small amount of Ce to the Y zeolite improved the activity and stability of the catalyst[8].

A hierarchical Y zeolite with a bimodal pore size distribution was applied in the synthesis of methyl lactate from fructose[9]. The results revealed that the hierarchical Y zeolite exhibited higher activity and selectivity than conventional Y zeolites, with a methyl lactate yield of 49.7% at 150°C

after 4 hours. In addition, the hierarchical Y zeolite could be easily regenerated and reused, making it a promising catalyst for the conversion of sugars to methyl lactate[9].

In addition to Y zeolites, other types of catalysts have also been investigated for the transformation of sugars to methyl lactate. For example, a mesoporous silica-supported tungsten catalyst was synthesized and used for the transformation of glucose to methyl lactate[10]. This catalyst exhibited high activity and selectivity, with a methyl lactate yield of 63% at 160°C after 3 hours. Furthermore, the tungsten containing catalyst could be easily recovered and reused, making it a promising catalyst for the conversion of sugars to methyl lactate.

Table 1 displays the maximum achieved methyl lactate yields obtained from the transformation of glucose and their derivatives in diverse research studies.

Table 1: The highest yield of methyl lactate in transformation of glucose in different studies

N	Catalyst	Conditions	X [%]/Y other products [%]	Y_{ML} [%]	Ref.
1	[K]-Sn-USY	30 bars, 150 °C, 0.266 mol L^{-1}, glu/cat 1.2 wt/wt, 6h, methanol	99	70	[11]
2	Sn-Beta	5 bar N_2, 160 °C, 0.137 mol L^{-1}, glu/cat 1.6 wt/wt	n/a	52	[14]
3	Sn-Beta-H-0.3*	5 bar N_2, 160 °C, 0.14 mol L^{-1}, glu/cat 1.6 wt/wt	99	58	[12]
4	Sn-Beta-H-0.3*	5 bar N_2, 160 °C, 0.14 mol L^{-1}, glu/cat 1.6 wt/wt, 10 h, ethanol	100	41	[12]
5	Sn-Beta-H-0.3*	5 bar N_2, 160 °C, 0.14 mol L^{-1}, glu/cat 1.6 wt/wt, 10 h, n-butanol	100	29	[12]
6	Sn-Beta-4h	5 bar N_2, 160 °C, 0.08 mol L^{-1}, glu/cat 1.6 wt/wt, 10 h	n/a	48	[15]
7	Sn-Beta-9h	5 bar N_2, 160 °C, 0.08 mol L^{-1}, glu/cat 1.6 wt/wt, 10 h	n/a	43	[15]
8	Sn-Beta-9h	5 bar N_2, 160 °C, 0.08 mol L^{-1}, glu/cat 1.6 wt/wt, 10 h, ethanol	n/a	29	[15]
9	Sn-Beta-9h	5 bar N_2, 160 °C, 0.08 mol L^{-1}, glu/cat 1.6 wt/wt, 10 h, n-butanol	n/a	20	[15]
10	Sn-Beta	10 bar N_2, 160 °C, 0.125 mol L^{-1}, glu/cat 1.4 wt/wt, 20 h	97	52	[15]
11	Sn-Beta	10 bar N_2, 160 °C, 0.125 mol L^{-1}, glu/cat 1.4 wt/wt, 20 h, ethanol	n/a	38	[15]
12	Sn-Beta	10 bar N_2, 160 °C, 0.125 mol L^{-1}, glu/cat 1.4 wt/wt, 20 h, n-butanol	n/a	25	[15]
13	Sn-MWW-nano	10 bar N_2, 160 °C, 0.12 mol L^{-1}, glu/cat 1.4 wt/wt, 20 h	n/a	36	[16]

14	deAl-Sn-Beta (100)	160 °C[e], 0.14 mol L^{-1}, 3 wt.% glucose in MeOH, glu/cat 3 wt/wt, 5 h	n/a	13	[14]
15	deAl-Sn-USY (25)	160 °C[e], 0.14 mol L^{-1}, 3 wt.% glucose in MeOH, glu/cat 3 wt/wt, 5 h	n/a	13	[14]
16	Sn-Beta-(150) HT, (HF)	160 °C[e], 0.132 mol L^{-1}, glu/cat 2.4 wt/wt, 12 h	100	47	[14]
17	Sn-Beta	5 bar N_2, 160 °C, 0.137 mol L^{-1}, 10 h	n/a	47	[12]
18	K-Sn-USY	170 °C[e], 0.26 mol L^{-1}, glu/cat 2.4 wt/wt, 12 h, MW	98	40	[14]
19	Sn-USY	160 °C[e], 0.13 mol L^{-1}, glu/cat 2.4 wt/wt, 2 h, MW	98	32	[14]
20	Sn-Beta (mesoporous)	40 bar He, 200 °C, 0.11 mol L^{-1}, glu/cat 0.75 wt/wt, 0.5h, water	98	58	[17]
21	Mg-Sn-Beta	4 bar N_2, 160 °C, 0.14 mol L^{-1}, glu/cat 1.9 wt/wt, 5 h	99	48	[18]
22	Zn-Sn-Beta	10 bar, 190 °C, 0.12 mol L^{-1}, glu/cat 1.4 wt/wt, 2 h, water	99	45	[19]
23	Zr-SBA-15	27.6 bar N_2, 240 °C, 0.06 mol L^{-1}, glu/cat 2.0 wt/wt, 6 h	n/a	37	[20]
24	Al_2O_3, calcined at 160 °C	5 bar Ar, 160 °C, 0.06 mol L^{-1}, 6 h	<99	34	[21]
25	Sn/(salen)IL	20 bar N_2, 160 °C, 0.06 mol L^{-1}, glu/cat 1.4 wt/wt, 20 h	100	40	[22]
26	Fe_2O_3 SnO_2 with 0.2 molar ratio of Fe/(Fe + Sn)	10 bar, 160 °C, 0.06 mol L^{-1}, glu/cat 1.4 wt/wt, 20 h	99	35	[23]
27	Mg-MOF-74	220 °C[e], 0.037 mol L^{-1}, glu/cat 3.0 wt/wt, 3 h, methanol	100	35	[24]
28	12 wt.% In/Al_2O_3	180 °C, 0.03 mol L^{-1}, glu/cat 2.0 wt/wt, 10 h, methanol/water 13.2 v/v	n/a	42	[25]
29	γ-NiOOH (Ni/2-Hmim-4)	200 °C[e], 0.044 mol L^{-1}, glu/cat 2.0 wt/wt, 3 h	100	40	[26]
30	UZAR-S4	160 °C, 0.013 mol L^{-1}, glu/cat 1.4 wt/wt, 20 h	n/a	49.9	[27]

Notation: *0.3 notes the concentration (mol/l) of TEAOH added in the synthesis of Sn-Beta zeolite.

Notably, the utilization of K and Sn modified ultra stable Y (USY) zeolites has yielded a remarkable maximum yield of 70%. This outcome was attained through the nearly complete conversion of glucose over a reaction period of 6 hours, conducted at a pressure of 30 bars and a temperature of 150 °C[11]. In addition to the aforementioned zeolites, numerous studies have explored the potential of Sn-beta zeolites as catalysts for this purpose. Diverse techniques and reaction conditions were employed, leading to the discovery Sn-Beta synthesized with the presence of tetraethyl ammonium hydroxide (TEAOH) acting as a mineralizer, which demonstrated a methyl

lactate yield of 58%[12]. This particular zeolite was reacted at 5 bar N_2, 160 °C, and an initial glucose concentration of 0.137 mol L^{-1}. Furthermore, recent investigations have identified strontium as a promising active metal in the context of this reaction. Analogously, the utilization of strontium resulted in a methyl lactate yield of 53% with complete conversion of glucose after 24 hour[13].

Overall, the use of Y zeolites as catalysts for the production of methyl lactate from sugars has shown a great promise. However, there are still several challenges that need to be addressed. For example, the use of expensive raw materials, such as fructose, can limit the economic viability of the process. In addition, the use of harsh reaction conditions, such as high temperatures and pressures, can lead to undesirable side reactions and catalyst deactivation[28]. Future research in this area should focus on developing more efficient and sustainable processes for the transformation of sugar to methyl lactate using Y zeolites.

1.2. Scope of work

Currently, the large-scale production of acrylic acid (AA) involves a two-step oxidation process of propylene[29]. AA finds extensive application in the synthesis of various functional materials, including superabsorbent resins. However, due to concerns regarding the potential scarcity of fossil resources, there has been a growing focus on developing sustainable methods for the one-step dehydration of lactic acid (LA) to produce AA[30]. This approach has garnered significant attention as a promising avenue for future AA production.

The initial phase of this project, described in this thesis, focuses on the transformation of glucose to methyl lactate (ML) as a means to environmentally friendly AA production. The primary objective is to identify a catalyst that exhibits superior performance, leading to high ML yield and selectivity. The chapter provides a comprehensive overview of the theoretical background relevant to the project, encompassing all necessary technical details essential for conducting experiments and interpreting the obtained results.

1.3. Chemicals

In order to gain comprehensive understanding of the reaction mechanisms pertinent to this study, it is essential to possess knowledge regarding the chemical characteristics of both the feedstock carbohydrates and the resulting methyl lactate and lactic acid. The subsequent sub-chapters

describes details into the industrial applications of these compounds and explore how their chemical properties can offer advantages or limitations at different stages of the reaction process.

1.3.1. Glucose

Glucose, characterized by the molecular formula $C_6H_{12}O_6$, is a simple sugar and one of the most abundant monosaccharides found in nature. It serves as a key building block for the synthesis of cellulose, the most prevalent carbohydrate worldwide[31]. Plants and a large portion of algae produce glucose through the process of photosynthesis, wherein water and carbon dioxide are converted into glucose with the aid of solar energy. Each glucose molecule contains five hydroxyl groups (**Figure 1**), which can undergo transformations and conversions into various chemicals or substances. This property is significant in the context of the reaction scheme for the formation of methyl lactate, which will be elucidated in subsequent sections.

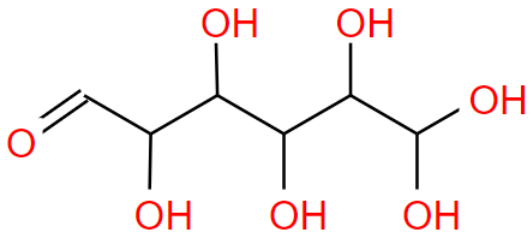

Figure 1: Glucose molecule

In contrast to methanol and ethanol, glucose exists as white or colorless solid substance that exhibit moderate solubility in acetic acid and water. These solids possess melting points of 146 °C and 150 °C, respectively, and undergo decomposition at 188 °C, releasing various volatile products while leaving behind a carbon residue. In aqueous solutions at 25 °C, glucose has a pK value of 12.16. Glucose is categorized as a hexose, belonging to the subclass of monosaccharides characterized by the presence of six carbon atoms. Among the sixteen possible stereoisomers of aldohexoses, glucose specifically refers to the D-isomer, also known as dextrose, which is occurring naturally. On the other hand, the L-isomer (L-glucose) does not naturally exist. Glucose can be obtained by hydrolyzing different carbohydrates such as lactose, sucrose, maltose, cellulose, glycogen, and others. Tapioca, potato, and wheat starch are commonly utilized raw materials for dextrose production in the United States and Japan. The process involves hydrolysis followed by enzymatic depolymerization through controlled pH pressurized steaming[32]. Glucose is an essential constituent of honey, present in an unbound form.

1.3.2. Methanol

Methanol, also known as methyl alcohol or wood spirit, is the simplest aliphatic alcohol with the chemical formula CH_3OH, where a methyl group is attached to a hydroxyl group. It is a colorless, volatile, flammable liquid that exhibits a distinct alcoholic odor reminiscent of ethanol. Historically, methanol acquired the nickname "wood alcohol" due to its primary production method involving the destructive distillation of wood. In modern times, the industrial production of methanol relies on the hydrogenation of carbon monoxide[33].

Pure methanol holds great importance in chemical synthesis as a vital component. Its derivatives are extensively employed in the synthesis of significant compounds such as synthetic dyestuffs, resins, pharmaceuticals, and perfumes. Methanol is utilized in large quantities for the production of various compounds[34]. Notably, it is transformed into formaldehyde for the production of synthetic resins and dimethylaniline for dyestuffs. Additionally, methanol serves as a general solvent and finds applications in rocket fuels, automotive antifreeze, and potentially as a high-octane, clean-burning fuel for replacing gasoline in automobiles[35].

Physically, methanol is a colorless liquid that solidifies at -93.9 °C and reaches its boiling point at 64.96 °C. It forms explosive mixtures when combined with air and burns with a nonluminous flame. Methanol exhibits complete solubility in water. It is important to note that methanol is a toxic substance, sharing a similar odor with ethyl alcohol, the intoxicating component of alcoholic beverages. Consumption of mixtures containing methanol has resulted in numerous cases of blindness or even death.

1.3.3. Lactic acid

Lactic acid is a type of organic acid with a molecular formula of $CH_3CH(OH)COOH$. It exhibits white color in its solid state and forms a clear solution when dissolved in water. The production of lactic acid involves both synthetic methods and utilization of natural resources. Lactic acid is classified as an alpha-hydroxy acid (AHA) due to the presence of a hydroxyl group adjacent to the carboxyl group. It serves as a synthetic intermediate in various organic synthesis and biochemical industries. The lactate anion, also known as lactate, is the conjugate base of lactic acid, while the derived acyl group is referred to as lactoyl[4].

Lactic acid, often abbreviated as LA, is the most abundant hydroxycarboxylic acid found in nature. It plays a crucial role in the production of biodegradable polymers, solvents, and oxygenated chemicals[36]. Currently, industrial-scale production of lactic acid is primarily achieved through the anaerobic fermentation of sucrose and glucose using microbial fermentation. This method overcomes the thermal instability issues associated with carbohydrates, which is inherent to the biochemical nature of the process. However, there are certain limitations and challenges associated with this fermentation method. If a chemical, which can act as a consistent base, is not added to neutralize the system, the acidity of the reaction mixture increases during lactic acid production due to the gradual deactivation of the bacteria[37]. Additionally, a significant amount of salt waste is generated during the separation of lactic acid from the fermentation broth, necessitating complex purification and separation steps for its removal. To align the process with the principles of green chemistry and ensure economic viability, it is crucial to develop cost-effective and efficient production methods for lactic acid[37].

1.3.4. Methyl lactate

Methyl lactate is an organic compound represented by the formula depicted in the **Figure 2**. It is commonly known as lactic acid methyl ester and serves as the methyl ester derivative of lactic acid. As the simplest chiral ester, it exists as a colorless liquid. Methyl lactate is readily available as a single enantiomer due to its natural origin. It exhibits the ability to dissolve nitrocellulose, cellulose acetate, cellulose acetobutyrate, and cellulose acetopropionate. This property contributes to its utility in the production of lacquers and dopes, as it imparts high diluent tolerance and offers favorable characteristics such as excellent flaw and blush resistance[38].

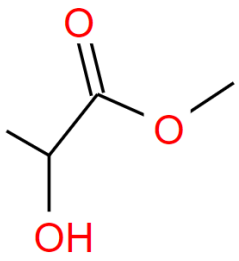

Figure 2: Methyl lactate formula

1.4. From sugars to methyl lactate

Figure 3 presents a visual representation of the primary steps involved in the conversion of sugars into methyl lactate (ML). The process begins with the isomerization of glucose to fructose. Subsequently, fructose undergoes retro-aldol condensation, resulting in the formation of two C_3 compounds: glyceraldehyde and dihydroxyacetone. The subsequent step involves the transformation of these C_3 compounds into pyruvaldehyde. This transformation can occur through either the addition of methanol, leading to the formation of pyruvaldehyde dimethyl acetal (PADA), or a redox reaction, resulting in the formation of highly thermodynamically stable ML[39]. It is important to note that PADA molecules can undergo a 1,2-hydride shift to further convert into ML, as depicted in Figure 3. However, it is worth mentioning that there is also a possibility of the formation of a side product called 1,1,2,2-tetramethoxypropane from PADA. During the retro-aldol condensation, a six-membered ring is formed as a transition state, facilitated by a Sn active site bonding to an oxygen atom on each of the C_2 and C_4 carbon atoms of the fructose molecule. This transition state is particularly favored under high temperature conditions[39].

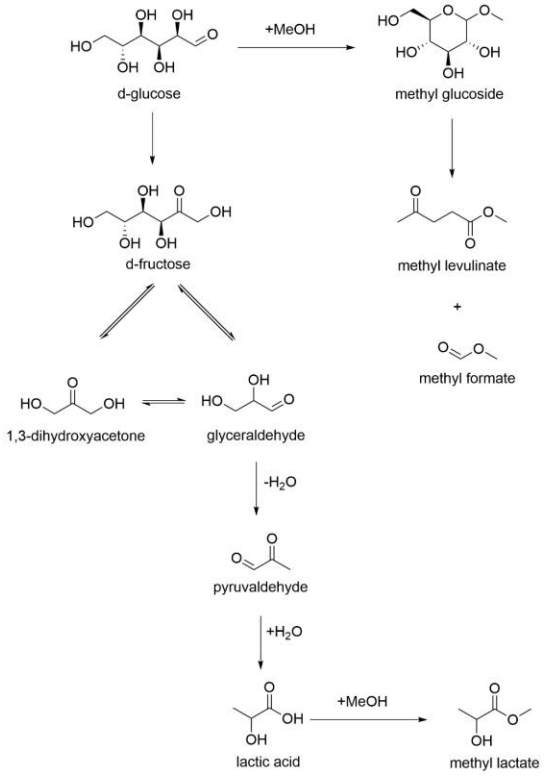

Figure 3: Reaction network of glucose to ML

2. Theory

Theoretical aspects of the completed research work are covered in this chapter. Methods for synthesis and physio-chemical characterization of catalysts, as well as information about their structure, are discussed.

2.1. Homogeneous and heterogeneous catalysts

Catalysis involves the acceleration of a chemical reaction through the addition of a catalyst to the reaction mixture. Catalysts play a crucial role in speeding up reactions without being consumed or undergoing any permanent changes themselves, as depicted in **Figure 4**. Even minute quantities of catalysts are often adequate when the reaction proceeds rapidly, and the catalyst can be efficiently regenerated[40]. The rate of the reaction is influenced by many factors such as synthesis methods and parameters of catalyst, and reaction conditions. Generally, catalysts interact with reactants to form intermediate species, which subsequently lead to the production of the desired final product, thereby enabling the catalyst to be regenerated for further use[40].

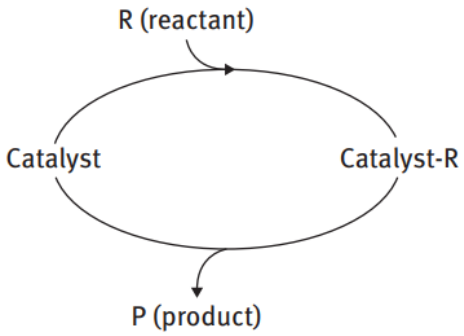

Figure 4: Catalytic cycle reproduced from *Murzin, D. Y. Engineering Catalysis (2020)*

Homogeneous catalysis refers to a system where all the components, including the catalyst, are in the same phase as the reactant, typically a gas or liquid. On the other hand, heterogeneous catalysts are present in a phase different from the reactant. Enzymes and other biocatalysts are often considered as a separate category being in fact either homogeneous or heterogenous. Catalysis finds extensive application across various sectors of the chemical industry, with approximately 90% of commercial chemical products utilizing catalysts at some stage of their production process[41]. As homogeneous catalysts operate in the same phase as the reactants, this limits their reactivity, making them less versatile compared to heterogeneous catalysts.

Some examples of homogeneous catalysts include the use of metal catalysts for alkene hydrogenation, catalysts for acid-base reactions, organometallic complexes, and certain gaseous catalysts involved in significant reactions like ozone depletion in the atmosphere[42].

Heterogeneous catalysis, on the other hand, plays a dominant role in the chemical industry and currently holds a significant share of the industrial catalyst market. These catalysts, usually in solid form, offer advantages in terms of separation and recyclability[43]. Their solid nature allows for effective separation of the reaction products from the catalysts, which is crucial in both batch and continuous processes. Historically, the key distinctions between homogeneous and heterogeneous catalysts have been their separability and recyclability. Heterogeneous catalysts benefit from easier and less expensive separation techniques. Furthermore, spent heterogeneous zeolite catalysts after separation can be regenerated and reused in the chemical production processes.

2.2. Zeolites

Zeolites are crystalline solids that possess distinctive structural features and microporous surfaces. These materials typically consist of silicon, aluminum, and oxygen atoms within their framework, along with cations, water molecules, and/or other molecules residing in their pores. While some zeolites are naturally occurring minerals that can be found abundantly through mining operations worldwide, others are synthetic and synthesized either for academic interests or produced commercially for specific applications[40].

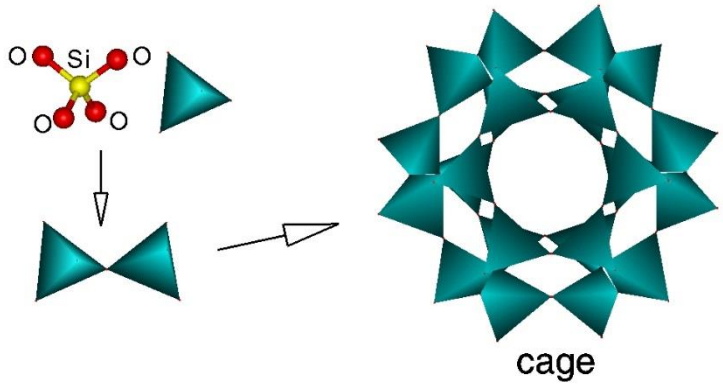

Figure 5: Framework structure of a zeolite adapted from *International Zeolite Association (IZA)*

The unique porous properties of zeolites make them highly versatile and widely utilized in various fields, resulting in a global market demand of several million tons annually[44]. Applications of zeolites are found in gas and solvent separation and removal, ion exchange processes for water

softening and purification, as well as in refining and chemical industry. Additionally, zeolites are employed in agriculture, animal husbandry, and construction. They are often referred to as molecular sieves due to their ability to selectively allow the passage of small molecules through their connected cages, cavities, or channels[44].

The distinguishing feature of zeolites lies in their framework, which consists of interconnected tetrahedra. These tetrahedra are composed of silicon atoms positioned at the corners and oxygen atoms at the centers. By linking these tetrahedra at their corners, a diverse range of intricate structures can be formed. These frameworks can contain interconnected cages, cavities, or channels that possess pore sizes optimized for the selective passage of small molecules. The diameter of these pores typically falls within the range of approximately 3 to 10 Å[45].

Zeolites are currently known to be more than 200 distinct framework structures[45]. Other compositions, such as the expanding class of microporous aluminophosphates, or ALPOs, have also been synthesized in addition to those with silicon or aluminum as the tetrahedral atom[4].

2.3. Properties of zeolites

Zeolites possess a porous structure that enables the passage of a diverse range of cations, including Na^+, K^+, Ca^{2+}, Mg^{2+}, and others. These positively charged ions are loosely held within a contacting solution and can be readily exchanged for different ions. Analcime, chabazite, clinoptilolite, heulandite, natrolite, phillipsite, and stilbite are among the prominent varieties of zeolite minerals. For instance, natrolite has a chemical formula of $Na_2Al_2Si_3O_{10}2H_2O$. Depending on their acidity, these zeolites with exchanged cations can catalyze various acid-catalyzed reactions[46].

Zeolites belong to the group of microporous aluminosilicate minerals known as "molecular sieves." These minerals primarily consist of silicon, aluminum, oxygen, and may incorporate metals such as titanium, tin, or zinc. The term "molecular sieve" describes the property of these materials to selectively separate molecules using a size exclusion mechanism, facilitated by their highly regular pore structure at the molecular level[47]. The pores of zeolites can only accommodate molecules or ions of specific sizes, determined by the dimensions of the channels. The designation of "eight-ring" refers to a closed loop formed by eight silicon (or aluminum) atoms and eight oxygen atoms

within the zeolite structure. The size of these rings is typically defined by the aperture's ring size. However, due to various factors such as strain resulting from bonding or coordination of oxygen atoms to cations within the structure, many zeolites exhibit non-cylindrical pores.

The pore of FAU consists of a circular 12-ring channel with a window diameter of 0.74 nm connecting almost spherical 1.18 nm cavities (**Figure 6**)[48]. Its application in fluid catalytic cracking (FCC) and hydrocracking processes has brought about a transformative advancement in the petroleum refining industry. Zeolite Y has also shown promising catalytic activity in biomass conversion. The primary active component in industrial cracking catalysts typically comprises ultra-stable Y (USY) zeolite, which is derived from post-synthesis dealumination of conventional zeolite Y. The dealumination process is intricate, time- and energy-intensive, but it can enhance the SiO_2/Al_2O_3 (SAR) ratio in structures of zeolites, (hydro)thermal stability, and introduce mesoporosity. However, an unfavorable gradient of dealumination inevitably emerges[49].

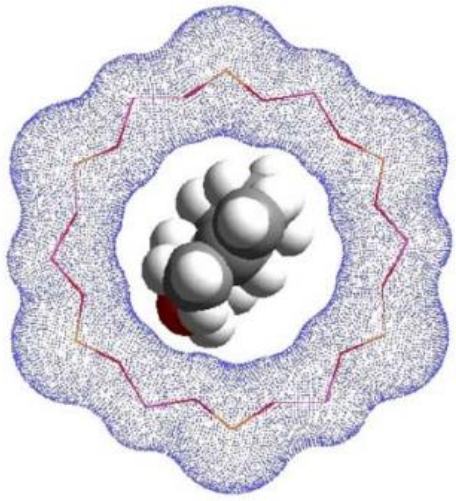

Figure 6: Y zeolite structure with the isopulegol molecule inside, adapted from [32]

.

2.3.1. Structural and topological properties

The effectiveness of a catalyst in catalyzing reactions is significantly influenced by its structural and topological characteristics[50]. The distinction in porosity between mesoporous materials and microporous zeolites has several consequences, with the most notable being the increased incorporation of metal ions into the framework. Similarly, the topology of zeolites has a substantial impact on the adsorption and diffusion of carbohydrates within their pore structure[51].

To avoid mass transfer limitations, pore blockage, and to ensure a uniform distribution of acid sites, a sufficiently large pore structure is required[52]. For example, it has been observed that Sn-Beta catalysts exhibited higher activity compared to catalysts with narrower pore structures such as MFI zeolites (10-membered ring, 0.55-0.6 nm pore sizes[53]) in the aldose-ketose isomerization of glucose to fructose[54]. In such cases, the introduction of secondary pore systems and nanostructuring has the potential to enhance this limited reactivity, leading to the emergence of hierarchical zeolites.

Zeolites possessing hierarchical porous architectures have demonstrated remarkable catalytic efficacy in diverse reaction scenarios, surpassing the performance of conventional catalysts. Furthermore, these zeolites exhibit additional advantageous catalytic properties[55]. This is partially attributed to their hierarchical structure, which allows for a higher loading of Sn in the framework due to larger diameter hierarchical pores[16]. Consequently, this facilitates the cleavage of carbon bonds in the fructose molecule, leading to improved conversion to ML[9].

2.3.2. Lewis and Brønsted acidity

Crystalline aluminosilicates, specifically zeolites, possess acidic sites resulting from the substitution of aluminum for silicon in the silica framework, enabling their application in catalysis. It is important to note that the presence of protons in zeolites balances the charge of Al^{3+}, contributing to their strong Brønsted acidity. The availability of protons and Lewis acid sites, which can function as solid acids by accepting electrons, is closely associated with the mechanism of acid-catalyzed reactions[40].

The selectivity toward ML (methyl lactate) in the methanol-mediated of triose sugars was found to be influenced by the Lewis acidity of the catalyst, similar to the impact of tin incorporation[56]. Achieving a remarkable level of selectivity towards ML can be accomplished through the utilization of a zeolite catalyst that possesses redox activity. This is due to the involvement of a redox step in the reaction pathway during the formation of ML[56]. The resemblance of this redox step was also highlighted to the Meerwein-Ponndorf-Verley reduction and Oppenauer oxidation (referred to collectively as MPVO-redox), where a Lewis-acidic catalyst facilitates the reduction of a ketone or aldehyde by an alcohol[57]. Zeolites with low or no Brønsted acidity are known to

exhibit active MPVO-redox properties. Furthermore, it is well-established in the literature that Brønsted acid catalysts tend to favor formation of the side products such as PADA, rather than ML[56].

In contrast, recent findings have demonstrated that a Brønsted acidic catalyst exhibits both exceptional catalytic activity and selectivity in the conversion of trioses into ML[58]. This contradicts earlier studies that proposed a correlation between low levels of Brønsted acidity and high levels of Lewis acidity with elevated ML yields. On the other hand, it was recently demonstrated that Brønsted acids catalyze dehydration of fructose into HMF (hydroxymethylfurfural), considered typically as a side product[59]. Consequently, the primary objective of this research is to enhance the Lewis acidity of the catalysts while minimizing Brønsted acidity, and to investigate the resulting effects.

2.3.3. Catalytic trinity

In industrial processes, the key criteria for a catalyst revolve around the three fundamental aspects of catalysis: activity, selectivity, and stability. Activity pertains to the catalyst's capacity to facilitate a process within a reasonable contact time, which directly impacts reactor dimensions and process capacity. In situations where the activity falls short, it is possible to compensate the low acidities by increasing the catalyst quantity or employing alternative measures, such as raising the temperature. However, selectivity of the catalyst holds a paramount importance, as it determines its ability to selectively promote the desired reactions. Additionally, the catalyst must exhibit adequate stability under the operating conditions to ensure sustained and reliable performance[40].

2.3.4. Fresh and the spent catalysts

In the context of this study, the term "fresh catalyst" denotes a recently prepared catalyst that has not undergone any reaction. Conversely, the term "spent catalyst" refers to a catalyst that has been employed in a reaction and subsequently separated from the reaction medium through filtration[40]. To ensure clarity and avoid any potential confusion, these terms will be utilized throughout this work to differentiate between the catalysts under examination and their respective characterization methods and results.

2.4. Catalyst synthesis methods

Heterogeneous catalysts are sophisticated products obtained through various chemical processes. The preparation of solid catalysts involves a series of steps, and the quality of raw materials utilized significantly influences their catalytic properties. In the laboratory, specific catalyst preparation techniques are selected based on the desired physical and chemical characteristics of the final composition, making the process comprehensible. Moreover, the choice of base materials also influences the preparation methods, and it has been observed that different approaches can be employed even for a specific base material. To outline the key stages involved in catalyst synthesis, the following sequential steps can be followed to prepare a catalyst[60]:

1) Precipitation: This step aims to precipitate a solid from a liquid solution. While each step in the preparation process can be thought of as a precursor to the one after it, the precipitation creates the imprint or latent image of the final solid that subsequent operations will gradually reveal. Supersaturation, nucleation, and growth are the three stages of precipitation[61] (**Figure 7**).

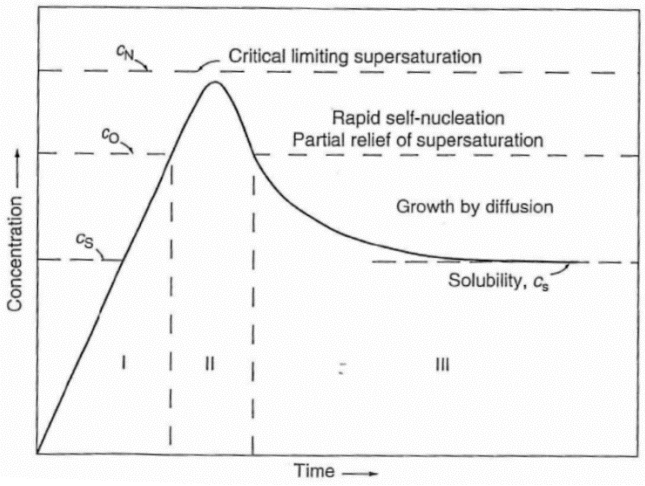

Figure 7: Supersaturation, nucleation, and growth of nanoparticles as a function of precipitation time. Notation: c_S-solubility, c_0-supersaturation, c_N-critical limiting supersaturation, reproduced from [46]

Supersaturation occurs when a solution holds more solute than it can normally dissolve. Nucleation is the formation of small clusters or nuclei from the supersaturated solution. Growth happens when solute molecules attach to nuclei, leading to the enlargement of crystals. These processes depend on factors such as temperature, concentration, and the presence of impurities.

2) Gelation: Gelation is facilitated by the use of gelling agents. It can be achieved through physical or chemical crosslinking. Chemical gelation involves the formation of covalent bonds, while physical gels are formed through physical interactions. In the 1940s, Flory and Stockmayer developed quantitative theories on chemical gelation[62].
3) Hydrothermal Transformation: Hydrothermal transformations involve changes in precipitates, gels, or flocculates resulting from temperature variations, aging, or ripening in the presence of a solvent such as water. These transformations typically occur at relatively low temperatures (100-300°C) and involve modifications to the texture or structure of the solid material. These changes follow the principles of thermodynamics and proceed in a direction that minimizes the system's free energy.
4) Filtration: Filtration is the physical separation of solid matter and liquid from mixtures using a filter medium with a complex structure that allows only the fluid to pass through. The fluid that passes through the filter medium is called the filtrate, while the solid particles that cannot pass through are referred to as oversize particles. Large particles can accumulate and form a filter cake, potentially obstructing the filter and causing blinding, which hampers the passage of the fluid phase. The "effective pore size" refers to the maximum particle size that can successfully pass through a filter.
5) Washing: Decantation, filtration, and centrifugation are common unit operations employed to separate the solid phase from the solvent or mother liquor. After separation, the solid material needs to be thoroughly washed to eliminate the remaining solvent and any impurities. This process, although time-consuming, is highly effective. Decantation can be performed simultaneously with washing, where the slurry is mixed with a significant amount of distilled water, allowed to settle, and then decanted. This process is repeated until the desired level of purity is achieved.
6) Drying: Drying involves the removal of the solvent, typically water, from the pores of a solid material. While routine for crystalline solids, drying is particularly crucial for flocculates and hydrogels that can contain a high percentage of water, sometimes up to 90%. Care must be taken during drying operations to maintain the desired porosity and prevent structural collapse. Drying is usually carried out at temperatures around 100-105°C, corresponding to the boiling point of water at standard temperature and pressure (STP).

7) Calcination: The term "calcination" encompasses a range of thermal processes used to create or prepare ceramic powders prior to dissolution in a liquid, shaping, and densification through sintering. Generally, calcination involves the thermal reaction of simple metal oxide powders to form a thermodynamically stable mixed metal oxide or the thermal decomposition of sparingly soluble metal oxide precursors, such as metal carbonates, hydroxides, and oxalates. Both processes are essential for the synthesis of many ceramic powders[63].

The calcination temperature is a significant factor impacting the degradation rate of the catalytic layer[64]. Initially, increasing the calcination temperature (within the range of 300-500 °C) enhances the catalytic performance of the sample. However, beyond this range, further elevations in temperature lead to a sudden decline in the performance of catalyst[64]. The reason behind this phenomenon lies in the crystallinity enhancement and removal of loosely bound impurities achieved through calcination. In the absence of calcination, excess moisture present in the sample hampers the utilization of active surface sites, resulting in decreased catalytic activity. Moreover, at very high temperatures (above 600°C), the mesoporous structure of the sample collapses, leading to a reduction in specific surface area, ultimately slowing down the rate of degradation[64,65].
Regarding the type of methods that are used and implemented for metal/metal oxide incorporation, four different synthesis methods will be discussed in this work; Evaporation Impregnation (EIM), Hydrothermal Synthesis (HS), Deposition Precipitation (DP), Alkaline Ion Exchange (AIE)."

2.4.1. Impregnation methods

The impregnation technique is a commonly employed approach in the production of supported catalysts for diverse reactions. This methodology encompasses three essential stages: initial impregnation of a high surface area support material with a solution containing metal precursors, subsequent evaporation of the solvent under elevated temperatures, and finally, reduction of the metal precursors in a controlled environment to generate the catalytically active phase. One notable benefit of the impregnation method is its inherent scalability, rendering it a favored alternative to colloidal synthesis[66].

An alternative technique frequently employed for the synthesis of heterogeneous catalysts is referred to as incipient wetness impregnation (IW or IWI), also recognized as capillary

impregnation or dry impregnation. This approach involves dissolving the active metal precursor in either an organic or aqueous solution, which is subsequently introduced to the catalyst support. The volume of the added solution corresponds to the pore volume within the support material. Through capillary action, the solution permeates the pores, and when additional solution surpasses the pore volume capacity of the support, the mode of solution transport transitions from capillary action to a slower diffusion process. Subsequently, the catalyst can be dried and calcined to eliminate volatile components from the solution and deposit the metal onto the catalyst surface. The maximum loading achievable is restricted by the solubility of the precursor in the solution. The distribution of the impregnated material within the pores is determined by the conditions of mass transfer during the impregnation and drying stages.

2.4.2. Ion exchange

Ion exchange refers to the reversible substitution of ions within an insoluble solid with ions of similar charge that are present in the surrounding solution. This versatile process holds considerable utility in various applications such as water demineralization, water softening, chemical cleansing, and the separation of substances. When it comes to purifying aqueous solutions, the practice of ion exchange often revolves around employing solid polymeric ion-exchange resins. This encompasses a diverse array of techniques that facilitate the exchange of ions between two electrolytes[40]. This technique finds widespread use in industrial and medical sectors for the purification and separation of crucial chemicals, along with its application in water treatment. Ion exchangers can be classified into two main categories: cation exchangers, which facilitate the exchange of positively charged ions (cations), and anion exchangers, which facilitate the exchange of negatively charged ions (anions). Additionally, there exist amphoteric exchangers that possess the ability to simultaneously facilitate cation and anion exchange. However, in cases where simultaneous exchange is necessary, it is common to utilize mixed beds comprising a combination of anion-exchange resins, cation-exchange resins, or multiple ion-exchange materials.

Alkaline ion exchange

In contrast to the previously mentioned metal grafting techniques, the alkaline ion exchange (AIE) method posed significantly greater challenges, requiring longer time periods and larger amounts of chemicals. The alternative methods commonly utilized involved metal grafting, filtration, washing

with distilled water, drying, and calcination. In contrast, the AIE approach involved a sequence of three distinct reactions, each accompanied by sequential steps of filtration, washing, drying, and calcination.

2.4.3. Deposition precipitation

Precipitation is the occurrence where a dissolved substance in an aqueous solution undergoes a transition from a supersaturated state, resulting in the formation of an insoluble solid. The resultant solid substance is commonly known as a precipitate, and its formation is facilitated by a chemical agent referred to as the precipitant in the realm of inorganic chemical reactions.

The phenomenon of precipitation arises when the concentration of a compound exceeds its solubility threshold. Variations in temperature, solvent evaporation, or solvent blending can serve as triggers for precipitation. Importantly, it should be acknowledged that precipitation tends to transpire at an accelerated pace in solutions that are highly supersaturated.

2.5.Catalyst characterization methods

The comprehensive analysis of catalysts' physicochemical properties entails evaluating their physical attributes and establishing connections between their structure and performance throughout the catalytic process. This endeavor involves the harmonization of various techniques for characterizing catalysts, along with the analysis of reaction mixtures, to effectively evaluate the catalyst's activity, selectivity, and stability.

2.5.1. X-ray diffraction

X-ray diffraction (XRD) is a scientific technique employed to investigate the atomic and molecular structure of various materials. It entails directing a beam of X-rays towards a specimen, resulting in the scattering of X-rays by the atoms present within the crystal lattice of the sample. Through careful analysis of this pattern, XRD provides valuable insights into the arrangement of atoms within the material, including parameters such as the spacing between atomic planes, crystal symmetry, and the presence of different crystalline phases. Exploiting this information allows for the determination of the crystal structure, identification of material composition, and characterization of various properties, such as crystallite size, strain, and texture[67].

2.5.2. Transmission Electron Microscopy (TEM)

Transmission electron microscopy (TEM) is a microscopy technique that generates images by directing an electron beam through a specimen. Typically, the specimen employed is either a grid-supported suspension or an ultrathin section measuring less than 100 nm in thickness. As the electron beam traverses the specimen, interactions between the electrons and the sample give rise to the formation of an image. Subsequently, this image is magnified and focused onto an imaging device, which can range from a fluorescent screen or a film sheet to a sensor, such as a scintillator connected to a charge-coupled device[68].

The utilization of transmission electron microscopy offers a distinct advantage over scanning electron microscopy, primarily in terms of significantly enhanced resolution when compared to light microscopes. This is attributed to the shorter de Broglie wavelength of electrons in comparison to light[69]. As a result, the transmission electron microscopy (TEM) instrument can capture intricate details, even at the atomic level, surpassing the resolution capabilities of a light microscope by thousands of times. This exceptional resolution makes TEM an invaluable analytical tool in the physical, chemical, and biological sciences. Various fields, including materials science, virology, cancer research, nanotechnology, semiconductor research, as well as disciplines like paleontology and palynology, derive significant benefits from employing TEMs[68].

2.5.3. Scanning Electron Microscopy, Energy-Dispersive X-Ray spectroscopy (SEM-EDX)

The Scanning Electron Microscope (SEM) is an advanced electron microscope that employs a highly focused electron beam to produce a topographical image and assess the relative composition of the specimen. When the concentrated electron beam interacts with the sample, it triggers the emission of secondary electrons (SEs). Furthermore, the SEM enables the detection of backscattered electrons and a specific form of X-ray emission from the sample[70].

Within the realm of electron microscopy, there exist two primary types of interactions that commonly occur: elastic interactions and inelastic interactions. In the case of inelastic interactions, when the sample is subjected to bombardment by primary beam electrons, energy is transferred to the atoms within the sample, causing the emission of low-energy secondary electrons (SEs).

Backscattered electrons (BSE) deflected at angles greater than 90 degrees, can be harnessed for the purpose of sample imaging[70]. The scanning electron microscope (SEM) combined with energy-dispersive X-ray spectroscopy (EDX) enables the determination of the elemental composition of a substance. By employing EDX spectroscopy, elements with atomic numbers greater than boron can be detected when their concentrations exceed 0.1%. The EDX spectroscopy instrument serves various purposes, including material assessment, identification, spot detection analysis of areas up to 10 cm in diameter, quality control screening, and other related tasks[71].

2.5.4. Fourier-Transform Infrared (FTIR) spectroscopy

The Fourier-transform infrared spectroscopy (FTIR) technique enables the acquisition of an infrared spectrum that depicts the absorption or emission of a solid, liquid, or gas. By employing an FTIR spectrometer, high-resolution spectral data covering a wide range of wavelengths are simultaneously collected. This surpasses the capabilities of a dispersive spectrometer, which measures intensity over a limited range of wavelengths at a time. Absorption spectroscopy techniques are employed to determine the extent of light absorption by a sample at each wavelength. Among these techniques, "dispersive spectroscopy" stands as the simplest approach, involving the illumination of a sample with a monochromatic light beam, measuring the absorbed light, and repeating the process for each distinct wavelength (for example, some UV-vis spectrometers function in this way). In Fourier-transform spectroscopy a beam containing multiple frequencies of light is shined at the sample instead of a monochromatic beam (a beam made up of only one wavelength) and then measures how much of that beam is absorbed by the sample. The beam is then changed to contain a different combination of frequencies, providing a second data point. This process is quick and repeatedly carried out over a brief period to calculate the absorption at each wavelength by working backward[72].

2.5.5. Liquid nitrogen physisorption

Liquid nitrogen physisorption method is used to determine textural properties of a catalyst. Van der Waals forces will cause a certain number of nitrogen gas molecules in contact with a solid at 77 K to be drawn to the solid's surface[73]. Physical or physisorption is the term used to describe this process. Physisorption differs from chemisorption in that its interaction energy is low[74]. The relative pressure of the N_2 gas in equilibrium with it determines the number of physisorbed

molecules. The ratio of absolute gas pressure to saturation pressure (p/p_0) is known as the relative pressure, or the atmospheric pressure at which unconstrained gas condenses. Since 77 K is the boiling point of N_2, the saturation pressure of N_2 at that temperature is 101.3 kPa. The amount of gas present at a particular area of a solid's surface at a given relative pressure depends on the surface's geometry and local surface-energetic characteristics. To interpret isotherms in terms of porosity and pore structure, physical models of adsorption and desorption mechanisms serve as the foundation[75].

2.5.6. Solid-State Nuclear Magnetic Resonance (NMR)

Nuclear magnetic resonance (NMR) spectroscopy is used in solid-state NMR (ssNMR) spectroscopy to characterize atomic-level structure in solid materials like powders, single crystals, amorphous samples, and tissues. In contrast to solution-state NMR, where rapid tumbling motion tends to average out many spin interactions, solid-state NMR preserves the anisotropic component of many spin interactions. Because of this, solid-state NMR spectra exhibit larger line widths than solution-state NMR spectra, which can be used to provide quantitative data on the molecular structure, conformation, and dynamics of the material. To eliminate anisotropic interactions and enhance the resolution and sensitivity of the technique, solid-state NMR is frequently combined with magic angle spinning[76].

2.5.7. Ultraviolet-Visible Diffuse Reflectance spectroscopy

UV spectroscopy, also known as UV-visible spectrophotometry (UV-Vis or UV/Vis), is the study of absorption or reflectance spectra in portions of the ultraviolet and the full, adjacent visible regions of the electromagnetic spectrum. This methodology is widely used in a variety of applied and theoretical applications because it is reasonably affordable and simple to implement. Together with fluorescence spectroscopy, absorption spectroscopy is useful. In addition to the measurement wavelength, parameters like absorbance (A), transmittance (%T), and reflectance (%R), as well as how they change over time, are important[77].

2.5.8. Temperature-Programmed Desorption (TPD)

Observing desorbed molecules from a surface when the surface temperature is raised is a technique known as temperature-programmed desorption (TPD). As soon as molecules and atoms come into a contact with a surface, they adsorb onto it, and their energy is reduced when a

bond with the surface is created. The interaction between the adsorbate and the surface affects the binding energy. The adsorbed species will eventually desorb if the surface becomes heated because of the energy transfer. The desorption temperature is the level at which this occurs. TPD thus provides information on the binding energy and availability of active sites[78].

2.5.9. Inductively Coupled Plasma (ICP) leaching

ICP leaching, or Inductively Coupled Plasma leaching, is a technique used for the extraction and analysis of various elements from solid samples. It involves the dissolution of a solid material in an acidic or alkaline solution, followed by the determination of the dissolved elements such as Inductively Coupled Plasma-Atomic Emission Spectroscopy (ICP-AES) or Inductively Coupled Plasma-Mass Spectroscopy (ICP-MS)[79].

2.5.10. CHNS analysis

CHNS analysis, also known as elemental analysis or elemental combustion analysis, is a technique used to determine the elemental composition of a sample, specifically the percentage of carbon (C), hydrogen (H), nitrogen (N), and sulfur (S) present in the compound or substance. The CHNS analysis involves the combustion of the sample at high temperatures in the presence of an oxidizing agent. During the combustion process, carbon and hydrogen are converted to carbon dioxide (CO_2) and water (H_2O), respectively. Nitrogen is converted to nitrogen gas (N_2), and sulfur is oxidized to sulfur dioxide (SO_2). After combustion, the resulting gases are separated, purified, and quantitatively analyzed using various detection methods. For instance, carbon and sulfur dioxide can be measured using gas chromatography (GC), while nitrogen and hydrogen are typically detected using thermal conductivity detection (TCD) or infrared detection methods[80].

3. Experimental

In this part of the thesis work, the experimental part and procedures of the research work will be described.

3.1.Chemicals

Chemicals used were obtained from different commercial sources and used without any purifications.

Table 2: Chemicals used

Chemical	Purity (%)	Supplier
H-Y-5.1	-	Zeolyst International
H-Y-30	-	Zeolyst International
H-Y-80	-	Zeolyst International
Tin(II) chloride	>99.9	Sigma-Aldrich
Tin(IV) chloride	>95	Sigma-Aldrich
Potassium chloride	>99	Sigma-Aldrich
Strontium nitrate	>98	CJSC Souzchimprom
Cesium nitrate	-	CJSC Souzchimprom
Triethylamine	-	Sigma-Aldrich
Hydrochloric acid	>37	Fluka
Nitric acid	70	Saltpeterzuur
Sulfuric acid	95-98	Fluka
D-(+)-glucose	-	Fluka
D(-)fructose	>99	Sigma-Aldrich
D-(+)-mannose	>99	Sigma-Aldrich
Alfa methyl glucoside	>95	Sigma-Aldrich
1-0-methyl-beta-d-glucoside	>99	Sigma-Aldrich
Methyl lactate	>98	Sigma-Aldrich
Methyl levulinate	>98	Sigma-Aldrich
Dl-lactic acid	90	Sigma-Aldrich
Dihydroxyacetone	>95	Merck KGaA
5-hydroxymethyl-2-furfural	99	Sigma-Aldrich
Dl-glyceraldehyde	>95	Sigma-Aldrich
Methyl vinyl glycolate	-	Enamine
Methyl formate	97	Sigma-Aldrich
Acetic acid	99	Sigma-Aldrich

3.2. Catalyst synthesis

3.2.1. Evaporation Impregnation (EIM) method

Evaporation impregnation (EIM) method was applied for synthesizing several Sn modified zeolite catalysts. Tin (II) chloride and tin (IV) chloride were used as aqueous solutions to study the effects of precursors. Catalyst synthesis procedure was as follows: 3.5 g of precursor was dissolved in 250 ml of water to create an acidic solution with a pH range of ca. 1.5-1.8, followed by the addition of 10 g of the zeolite catalyst, and pH was then determined being in the range of ca. 1.7–2.0. Finally, a rotavapor was used to synthesize a catalyst for 24 hours at 50 °C and 60 rpm in a flask containing H-Y zeolite and an aqueous solution of tin (IV) chloride. To recover the catalyst from the flask after the synthesis was finished, water was evaporated. A step-calcination process as shown in **Figure 8** was used to calcine the catalyst after it has been dried at 100 °C in an oven for

an entire night. Six distinct catalysts have been prepared and labeled separately by altering the silica-to-alumina ratio in the parent H-Y zeolite and the precursor.

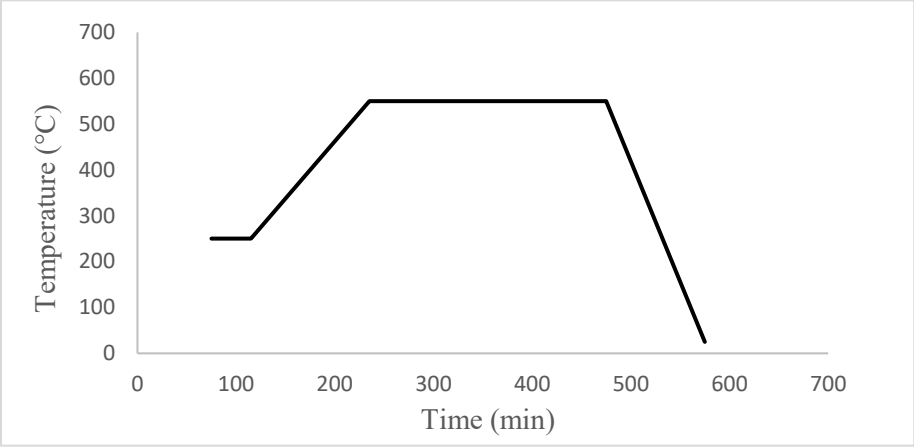

Figure 8: Step calcination process that was followed for catalysts synthesis.

The spent catalysts from the reaction were regenerated with the step-calcination procedure as given in **Figure 9**. The regeneration method involved the removal of any impurities or carbonaceous deposits that accumulated on the catalyst surface during the reaction[81]. The regenerated catalyst was then evaluated for its catalytic performance in the subsequent reaction cycle.

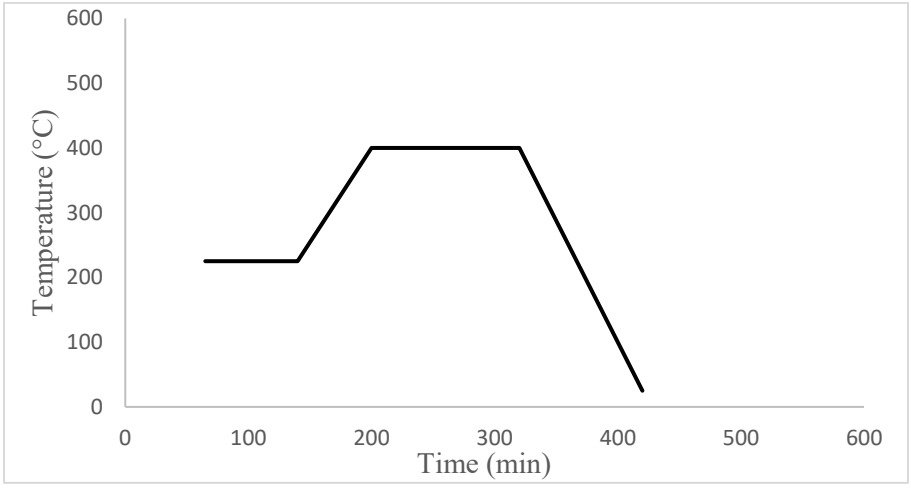

Figure 9: Step calcination procedure for the regeneration of the catalyst (K-Sn-H-Y-30-DA-4)

3.2.2. Alkaline Ion Exchange

Synthesis of catalysts by the alkaline ion exchange method was also performed using Y zeolites with varying SiO_2/Al_2O_3 ratios. The procedure for the synthesis is given in the reference[82]. For dealumination, H-Y catalyst was treated with 10 M 70% aqueous nitric acid solution for 1 h and then filtered and neutralized with distilled water until pH close to 7 was reached. The filtered catalyst was dried overnight at 100 °C. This was repeated two times and then Sn modification was performed followed by drying and calcination with the same procedure. Thereafter, K modification was performed with the given molarity of the aqueous KCl solution. For that, 250 ml aqueous solution of KCl with 0.5 M molarity was prepared and the Sn-modified catalyst was stirred for 2 h at room temperature. The final catalyst was again filtered, dried at 110 °C for overnight, and calcined at 550 °C for 6 h with the step calcination procedure as given in **Figure 8**. This experiment was performed a few more times for H-Y zeolites with different SiO_2/Al_2O_3 ratios.

3.2.3. Incipient Wetness Impregnation

A frequently used method for creating heterogeneous catalysts is incipient wetness impregnation (IW or IWI), also known as capillary impregnation or dry impregnation. The active metal precursor is typically dissolved in an organic or aqueous solution. The metal-containing solution is then added to the catalyst support that has the same amount of pore space as the volume of the added solution. The solution is attracted to the pores by capillary action in which more solution is added than the support pore volume can hold, the process of solution transport switches from capillary action to diffusion, which is much slower. The metal can then be deposited on the catalyst surface after being dried and calcined to remove the volatile components from the solution. The solubility of the precursor in the solution regulates the maximum loading. The mass transfer conditions within the pores during impregnation and drying determine the concentration profile of the impregnated compound.

To perform Sr and Cs modification, the IW method was used as follows; first, 0.5 M solution of $Sr(NO_3)_2$ and CsCl precursors was prepared by slowly adding the Sn modified H-Y zeolites with the SiO_2/Al_2O_3 ratio of 30 under 100 rpm stirring. The mixture was stirred for 2 hours filtered and washed twice with deionized water. Then, it was dried at 100 °C followed calcination at 550 °C for 6 h.

A list of the synthesized catalysts is shown in **Table 3**.

Table 3. The synthesized zeolite catalysts
(All catalysts were calcined using step-calcination procedure given in Table 2).

No	Precursor	Type of Catalyst	Weight (g)
1	$SnCl_2$	Sn-H-Y-5.1-EIM	6
2	$SnCl_2$	Sn-H-Y-80-EIM	4.95
3	$SnCl_2$	Sn-H-Y-30-EIM	4.19
4	$SnCl_4$	Sn-H-Y-30-EIM	11.2
5	$SnCl_4$	Sn-H-Y-80-EIM	11.02
6	$SnCl_4$	Sn-H-Y-5.1-DA	11
7	$SnCl_4$, KCl	K-Sn-H-Y-5.1-DA	7.7
8	$SnCl_4$, KCl	K-Sn-H-Y-30-DA	3.6
9	$SnCl_4$, KCl	K-Sn-H-Y-80-DA	9.3
10	$SnCl_4$, $SrNO_3$	Sr-Sn-H-Y-30-DA	6.5
11	$SnCl_4$, CsCl	Cs-Sn-H-Y-30-DA	6

3.3. Catalyst characterization

X-Ray Diffraction (XRD): Using powder X-ray diffraction (XRD), the crystal phases and phase purity were identified for a group of Sn and alkaline earth metal catalysts supported on H-Y-5.1, and H-Y-30. The XRD analysis was done for samples that were dried and calcined. It was focused on using the Bragg-Brentano configuration. The XRD patterns of catalysts were captured using the CuKα radiation (=1.5418 Å) and a one-dimensional LynxEye detector and with an angular range of 2.9° on the 2θ scale by scanning in the 2θ-angle range from 15° to 70° with a step of 0.05° and the acquisition time of 3 s at each point. From the broadening of the diffraction peaks, the sizes of the coherently scattering domains (CSD – D_{XRD}) were calculated. According to the diffraction pattern of the international standard α-Al_2O_3 (SRM 1976)[83], the instrumental broadening of the diffraction lines was recorded and taken into consideration.

Using a PANalytical Empyrean diffractometer with a five-axis goniometer, the XRD measurements of other dealuminated and metal (Sn, K) modified catalysts were carried out. The incident beam optics included a Bragg-Brentano HD X-ray mirror, a fixed 1/4º divergence slit, a 10 mm mask, a 0.04 rad Soller slit, and a 1° anti-scatter slit. The optics for the diffracted beam included a PIXcel detector array, a 0.04 rad Soller slit, and a 7.5 mm divergence slit. The used X-ray equipment was an Empyrean Cu LFF tube. Only the Cu Kα1 and Cu Kα2 components of the X-ray radiation were kept out by a filter.

Transmission Electron Microscopy (TEM): The Jeol JEM-1400Plus, which has a 120 kV acceleration voltage and a resolution of 0.38 nm, was used to study the metal particle size, textural characteristics, porosity, and periodicity of pores of catalysts[84]. Before the TEM measurements, the majority of the Sn-based catalysts were calcined. Before conducting catalytic tests, the set of monometallic and bimetallic catalysts originating from H-Y zeolites with various SiO_2/Al_2O_3 ratios (5.1, 30, 80) was characterized. To compare the changes in textural properties after the reactions, some of the used catalysts were also similarly characterized. Using ImageJ software, the catalysts' particle size distributions were determined.

Scanning Electron Microscopy and Energy Dispersive X-rays Spectroscopy (SEM-EDS): The crystal morphology of the prepared catalysts was investigated using SEM, and EDX was used to ascertain their elemental compositions. SEM measurements were carried out using a Zeiss Leo Gemini 1530 Scanning Electron Microscope and a Thermo Scientific UltraDry Silicon Drift Detector (SDD)[84]. The X-ray analyzer was operated at an acceleration voltage of 15 kV.

Nitrogen physisorption: The Micromeritics 3Flex-3500 was used for the surface area measurements. Before measuring the weight of the empty, a burette was first degassed for two minutes under vacuum. For ex-situ treatment of samples, ca. 50–100 mg of the catalyst was heated overnight at 180 °C under vacuum of 0.2-0.3 bar. The following morning, the weight of the sample was determined. The catalyst's moisture was eliminated in this step. After that, the adsorption isotherms at -196 °C were measured, and the moles of nitrogen adsorbed on the sample at various relative pressures were plotted. The Dubinin-Radushkevich method was used to determine the specific surface areas of the synthesized microporous materials. The DFT method was used to determine the pore size distribution of the catalysts.

Fourier-transform infrared (FTIR) spectroscopy: ATI Mattson FTIR was used to perform the qualitative and quantitative analysis of the catalyst's Brønsted and Lewis acid sites while using pyridine as a probe molecule. The catalyst was prepared as a thin, self-supporting pellet with a radius of 0.65 cm, which was then placed inside the FTIR cell. For pretreatment, the cell temperature was raised to 450 °C under a vacuum and maintained there for an hour. Thereafter, a background spectrum of the sample was captured while the temperature was lowered to

100 °C. The probe molecule (pyridine) was adsorbed at 100 °C for 30 min and then desorbed by evacuation at various temperatures. During the desorption process, three distinct temperatures are employed: 250 °C for weak, medium, and strong acid sites, 350 °C for medium and strong acid sites, and 450 °C specifically for strong acid sites. At each temperature increment, the spectrum of the adsorbed pyridine is recorded. The scanning is conducted under a vacuum pressure ranging from 10^{-2}-10^{-1} bar, with the temperature set at 100 °C. Spectral bands at 1545 cm^{-1} and 1450 cm^{-1} are utilized to differentiate between Brønsted and Lewis acid sites during the scanning procedure. Using the molar extinction parameters published by Emeis[85], the acid sites were quantified. Calculations were made with consideration for the catalyst's weight.

Ultraviolet-Visible Diffuse Reflectance Spectroscopy (UV-vis DRS): Different catalysts were subjected to UV-vis DRS analysis to distinguish the positions of the metals (Al, Sn, and K) and to compare the data with the catalyst performance. For this purpose, the reflectance was measured using an Avantes Avaspec HS-TEC CCD spectrometer connected to a fiber optic cable by an Avantes FC-UV600-1-SR. The light source was an Avantes AvaLight-DHc, which uses halogen and deuterium lamps. The white reference was a $BaSO_4$ disc made by Edinburgh Instruments.

Solid-State Nuclear Magnetic Resonance (SS-NMR): ^{27}Al MAS NMR spectra were recorded on a Bruker AVANCE-III spectrometer operating at 79.50 MHz (^{29}Si) and 104.26 MHz (^{27}Al) equipped with a CP-MAS 4 mm solid state probe. The ^{27}Al spectra were recorded using a 5.00 µs pulse and a recycle delay of 0.05 s at 14 kHz spinning speed.

Inductively Coupled Plasma (ICP) leaching: The possible metal leaching into liquid phase was investigated by filtering out the catalyst from the reaction mixture after 24 h reaction time. To prepare the product sample for subsequent analysis using Inductively Coupled Plasma (ICP) measurement, methanol was removed from the product by purging with nitrogen gas. Subsequently, 3.6 ml of hydrochloric acid (65%, Sigma Aldrich) and 1.2 ml of nitric acid (70%, Sigma Aldrich) were added to the product to achieve an optimal concentration for the equipment. The resulting solution was transferred into a 100 ml volumetric flask, ensuring that the walls of the beaker were thoroughly rinsed with an in-situ prepared aqua regia. The solution was then diluted

with distilled water to a final volume of 100 ml. Once the sample was prepared and measured, the discrepancies in metal concentrations between the two different media could be detected.

Hot filtration test: The hot filtration test was performed for verification of catalyst stability to leaching into the reaction solution. The reaction which was carried out with 2 wt.% Sr – 2 wt.% Sn/H-Y-30-Da catalyst for 24 h, was stopped for cooling and separation of the reaction mixture from the solid catalyst. The separation was performed by the filter paper (Whatman, 2 μm pore size) with the further filtration (PVDF syringe filter, 0.45 μ). The filtrate was loaded into the autoclave, heated to 150 °C and run for another 24 h. The hot filtration test allows for the separation of reaction products from the solid catalyst, enabling evaluation of the catalyst's performance and analysis of the reaction products.

3.4. Catalyst Testing

Experiments were carried out in a batch mode using an autoclave (**Figure 10**) that was designed for a maximum pressure of 200 bar. Transformations of glucose to methyl lactate were carried out as follows; the reactor was loaded with 0.75 g of the catalyst, 0.9 g of glucose, and 75 ml of methanol. Once the reactor was loaded, it was flushed by an inert gas (argon) to remove air. Flushing was done 3-5 times making sure that there is no air left inside the reactor. Thereafter, the heating of the reactor was started with a 3 °C/min heating rate. When the desired reactor temperature was reached, the total pressure was adjusted to 30 bar and the sampling time (t=0 min) and stirring (720 rpm) were started. Samples were taken at different reaction times (0, 15, 45, 90, 180, 360 min) during and after the reaction (24 h). The samples were withdrawn from the reactor through a 7 μm sinter to avoid removal of the catalyst particles, moreover, the liquid samples were further filtered through a 0.43 μm syringe filter. HPLC (Hewlett Packard 1100 series) was used for the initial analysis of the samples, then after achieving practically full sugar conversions, a gas chromatograph - GC (HP 6890 Series) was used for analysing the products after the reactions.

Figure 10 - Batch reactor used for methyl lactate synthesis

3.5. Analysis of products

High-Performance Liquid Chromatography (HPLC) for sugars: The analysis of the composition of the reaction mixture was conducted using high-performance liquid chromatography (HPLC). Specifically, an HPLC instrument from the Hewlett Packard 1100 series was utilized, which featured a refractive index detector (RI). Separation of the compounds was achieved using an Animex HPX-87H column, with 5 mM sulphuric acid serving as the eluent. The column temperature was maintained at 45 °C, and the flow rate of H_2SO_4 was set at 0.6 ml/min. Prior to the catalytic experiments, response factors and retention times for various compounds were determined and subsequently employed in concentration calculations.

Table 4: HPLC retention time of the sugars

Sugar	Retention Time (min)
Glucose	8.88
Fructose	9.82
D-mannose	9.62
α-Methyl glucoside	10.14
β-Methyl glucoside	10.56

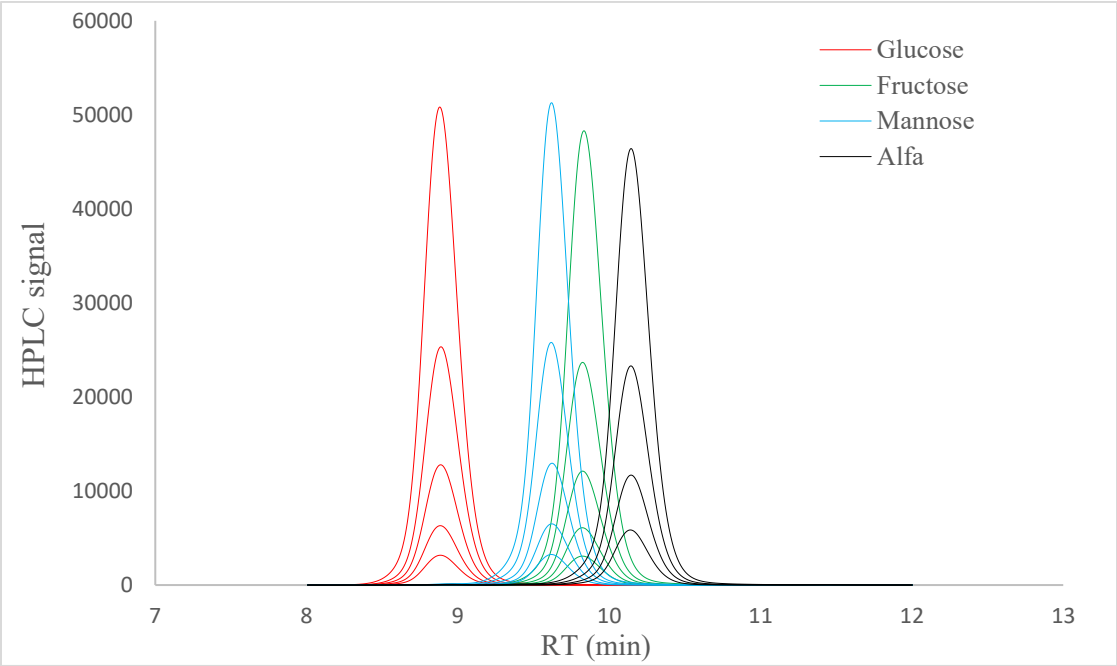

Figure 11: Calibrated sugars in HPLC

Gas Chromatography (GC) for analysis of liquid phases: The sample was further analyzed by gas chromatography to quantify methyl lactate, methyl levulinate, as well as furfural and methyl formate after achieving in practice full conversion of glucose. The GC was an HP 6890 Series GC System with an HP-5, 5 % phenyl methyl siloxane column of length 30.0 m 320 µm x 0.50 µm thickness and a flame ionization detector (FID). The analysis used the following temperature program: 2 minutes at 40 °C, 10 °C per minute heating to 250 °C, holding for 3 minutes, and 3.8 ml/min of gas flow rate through the column. The compounds were calibrated in GC before the measurements began, and the outcomes are listed in **Table 5**.

Gas Chromatography-Mass spectrometry (GC-MS) for product detection: The unknown compounds in the product samples were identified using gas chromatography and mass spectrometry. The equipment employed in this study incorporated an Agilent HP-1 column, where the stationary phase consisted of dimethylpolysiloxane. The separation of different compounds during elution along the column in gas chromatography-mass spectrometry (GC-MS) relies on the varying affinities of these compounds for the stationary phase.

The analysis method is typically applicable to carbohydrates because sugars decompose during the process through caramelization, but techniques such as extraction and silylation were used to

get around this. The procedures for the sample preparation for the extraction of the sample with dichloromethane and analysis with GC-MS and silylation followed by short column GC analysis for sugars are given in Appendix D and E, respectively.

Table 5: GC retention time of the chemicals

Product	Retention Time (min)
Methyl formate	3.8
Methyl lactate	12.2
Methyl-vinyl-glycolate	15.89
Furfural	16.09
Methyl levulinate	18.5
1,3-Dihydroxyacetone	29.6
Lactic acid	31
Methoxymethyl-furfural	36.89
Hydroxymethyl-furfural	37.02

3.6. Formulae and definitions

Conversion of glucose (X) was calculated by:

$$X(\%) = 100\% * \frac{n\_g_0 - n\_g_f}{n\_g_o} \quad (1)$$

Where, n_g_o and n_g_f are the initial and final moles of glucose, respectively.

The liquid phase mass balance of compounds (MB) was calculated by:

$$MB\ (\%) = 100\% * \frac{MB_f}{MB_0} \quad (2)$$

Where MB_f is the sum of liquid-phase reactants and products at the end of the reaction (time 24 h), and MB_0 is the sum of liquid-phase reactants at the beginning of the reaction (time 0).

The **yield** of methyl lactate was calculated by:

$$Y(\%) = 100\% * \frac{(n\_ml_{1400})/2}{n\_g_0} \quad (3)$$

Where n_ml_{1400} is the final molar amount of methyl lactate.

Selectivity was calculated by this equation:

$$S(\%) = Y(\%)/X_{gl} \quad (4)$$

4. Results and Discussion

4.1. Catalyst characterization results

X-ray diffraction

The XRD patterns for S1, S4-S8 (**Table 6**), with matched standard structures, are shown in **Figure 12**.

Table 6: The catalysts characterized using X-ray powder diffraction

Sample Label	Info
S1	H-Y-5.1
S2	Sn-H-Y-5.1-DA
S3	K-Sn-H-Y-5.1-DA
S4	H-Y-30
S5	Sn- H-Y-30-DA
S6	K-Sn- H-Y-30-DA
S7	Sn-H-Y-30-EIM
S8	$SnCl_4$-H-Y-30-EIM

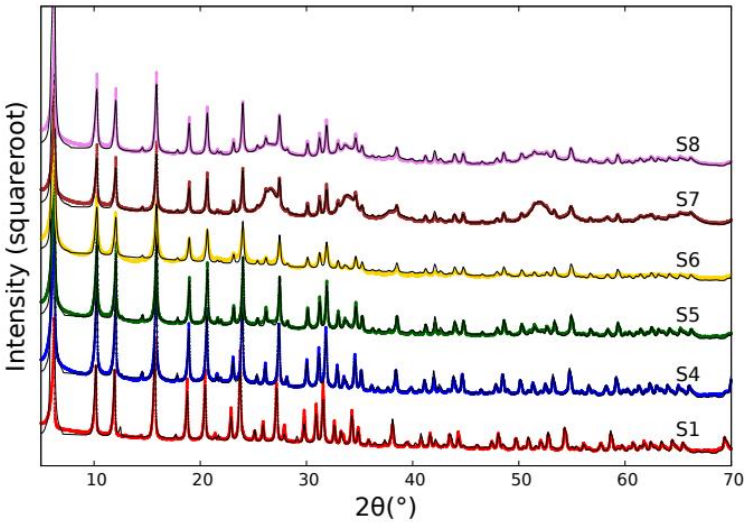

Figure 12: The XRD patterns of S1, S4-S5 with fitted standard structures including faujasite zeolite and SnO_2

The faujasite zeolite[86] and SnO_2[87] were identified as the phases present. All the diffraction data obtained for S1, S4-S8 were found to be well-matched with the faujasite zeolite phase. In addition, the diffraction patterns of S7 and S8 revealed clear details that can be attributed to the presence of SnO_2 phase[87]. The volume percentage of SnO_2 phase in S7 and S8 was approximately 5% and 3%,

respectively. Although traces of SnO_2 phase were possibly to be observed in S5 and S6, the identification is not considered reliable.

The X-ray diffraction patterns for S2 and S3 (**Figure 13**) are comparable. The identification of minor traces, which appear to correspond to faujasite zeolite and SnO_2 phases, was possible. However, these samples exhibit low crystallinity, and the identification of the phases is based on minor diffraction features, and as such, it may not be conclusive. Furthermore, a distinct diffraction peak located near $2\theta = 7.7^\circ$ cannot be attributed to faujasite zeolite[86] and SnO_2[87]. This may indicate an incorrect identification of phases or/and the presence of an additional phase. Potential matches comprise multiple SiO_2 structures (such as ICSD 142091, ICSD 62582, ICSD 153336), but without additional information, precise phase identification based on a single diffraction peak is not feasible**.**

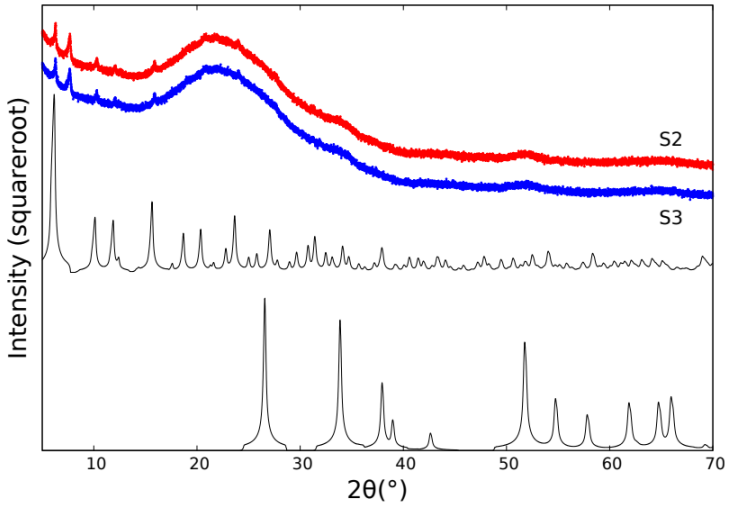

Figure 13: The XRD patterns of S2 and S3 with unfitted standard models including faujasite zeolite and SnO_2

Scanning Electron Microscopy and Energy Dispersive X-rays Spectroscopy (SEM-EDX)

The scanning electron microscopy (SEM) technique was employed to examine the morphological properties, including shape, size, and crystal distribution of the catalysts. The chemical compositions of the synthesized zeolites, which incorporated various metals (Sn, K, Sr, Cs), as well as their amounts in the catalysts prepared by different synthesis methods, were determined using energy dispersive spectroscopy (EDS). The SEM micrographs of all catalysts revealed distinct crystallites of Y zeolites that maintained their structures even after the addition of Sn and K.

The investigation involved a comparison between two synthesis methods: evaporation impregnation and a method similar to the one utilized by[11]. **In Figure 14**, the two zeolites synthesized from H-Y-30 using the evaporation impregnation method are illustrated. The catalysts under investigation were distinguished by the type of the precursor utilized. The catalyst on the left was synthesized employing $SnCl_2$ as the precursor, whereas the other zeolite was synthesized using

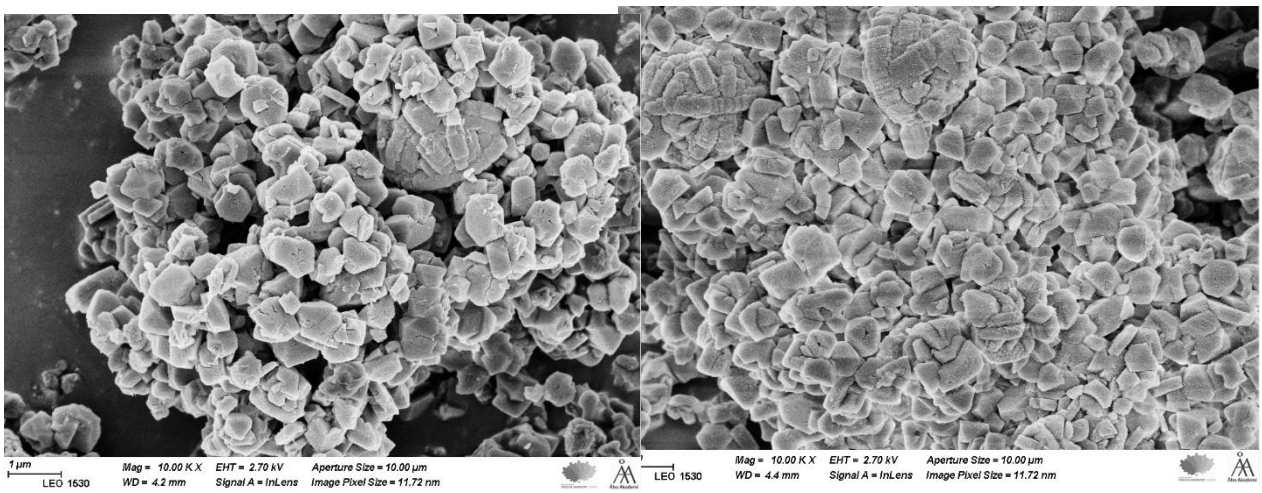

Figure 14: SEM micrographs of Sn-H-Y-30-EIM catalysts with different precursors ($SnCl_2$ left, $SnCl_4$ right)

$SnCl_4$ in a synthesis process lasting 24 hours. Examining the synthesized catalysts employing different Sn precursors demonstrates that variations in their properties, including morphology, crystallinity, surface area, pore volume, and catalytic activity[53], can arise. The scanning electron microscopy (SEM) analysis revealed noticeable agglomeration of the catalyst particles synthesized using $SnCl_4$ precursor. This agglomeration phenomenon was attributed to the low pH of the precursor solution, a finding consistent with the previous studies[88]. In contrast, Sn-H-Y-30 zeolites impregnated with $SnCl_2$ precursor exhibited a more uniform distribution of tin, resulting in catalyst particles with rectangular, triangular, pyramidical, or hexagonal shapes characterized by sharp edges. The crystal sizes ranged from 210-520 nm, with an average size of 345 nm. Conversely, the catalysts prepared with $SnCl_4$ precursor exhibited predominantly spherical and rectangular particle shapes, indicating a less homogeneous particle distribution. The particle sizes varied from 360-620 nm, with an average diameter of 501 nm. These results clearly demonstrate the significant influence of the precursor on the crystal size and shape during the synthesis process. The use of $SnCl_2$ as a precursor for Sn modification of H-Y catalysts has been reported to yield small crystal sizes[89]. This

observation can be attributed to the higher reactivity of $SnCl_2$, facilitating a more homogeneous distribution of tin within the zeolite structure and leading to the formation of small crystals[89].

The two precursors employed in the catalyst synthesis, $SnCl_2$ and $SnCl_4$, possess distinct chemical structures and properties that can exert an influence on the ultimate characteristics of the catalysts. The precursor choice can impact the quantity and distribution of Sn species within the catalyst, thereby affecting the material's catalytic performance. Furthermore, the chosen preparation method, such as impregnation or sol-gel, can also influence the catalyst's properties. Consequently, catalysts synthesized using diverse Sn precursors can exhibit distinctive characteristics, thereby influencing their applicability for various catalytic applications.

Furthermore, **Figure 15** displays the scanning electron microscopy (SEM) micrographs of both the dealuminated fresh and spent K-Sn-H-Y-30-DA catalysts. This particular catalyst has demonstrated exceptional performance in the reaction under investigation (Section 4.2). The SEM analysis of the metal-modified H-Y zeolites unveiled the presence of uniform and well-structured crystallites within the catalysts. Notably, **Figure 15** reveals that the bimetallic catalyst support remained intact throughout the 24-hour reaction, displaying consistent crystal size and shape. Visible indications of cracks and the creation of mesopores were evident in the fresh catalyst, along with a crystal size range spanning from 220 to 600 nm. Conversely, the spent catalyst exhibited a diminished presence of cracked and blocked mesopores, primarily attributed to the deposition of coke formed during the reaction. Furthermore, the crystal sizes observed in the spent catalyst ranged from 246 to 660 nm. Notably, both the fresh and spent catalysts showcased comparable particle size distributions for the metal component, measuring 5.4 nm and 5.6 nm, respectively.

Similarly, the monometallic catalysts (Sn/H-Y-30 and K/H-Y-30), as illustrated in Appendix B, also exhibited preserved structures following the metal modifications (K, Sn, Sr, Cs). These findings indicate that the employed metal incorporation techniques in this study, encompassing ion-exchange, evaporation-impregnation, and deposition-precipitation methods, had no discernible impact on the morphological characteristics of the parent supports.

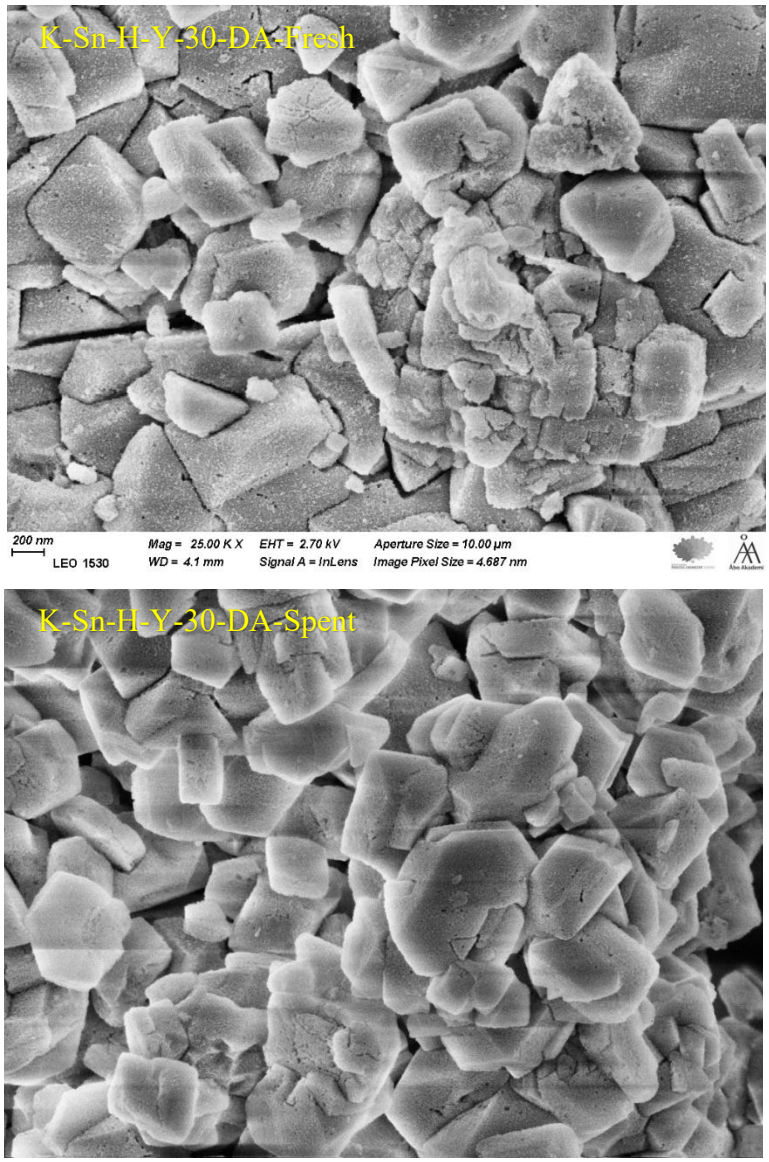

Figure 15: SEM micrographs of the fresh and the spent K-Sn-H-Y-30-DA catalysts

EDX analysis was applied both for fresh and spent catalysts showing that Sn-content determined by EDXA varied from 1.4 to 2.4 wt.%. The EDXA elemental analysis of the fresh and spent K-Sn-H-Y-30-DA catalysts demonstrated that the mass ratio of Sn to Si was about 0.126 and it was decreased to 0.114 after the reaction. This result indicates that leaching of tin occurred during the reaction as also confirmed by ICP analysis (Section 4.2) and by hot filtration test (Section 4.4). Furthermore, no sulfur, chloride or phosphorus were detected in the spent catalyst.

Transmission Electron Microscopy (TEM)

In the current investigation, transmission electron microscopy (TEM) was utilized to evaluate the dimensions and dispersion of metal nanoparticles present in different catalysts employed for the transformation of glucose to methyl lactate. The TEM images and the corresponding histograms of selected catalysts employed in the reaction are presented in **Figure 16** and **Figure 17**. Specifically, **Figure 16** illustrates a catalyst prepared using the evaporation impregnation technique, with $SnCl_2$ serving as the metal precursor. This preparation method led to a remarkable dispersion of Sn species owing to the utilization of a high precursor loading (35 wt.%).

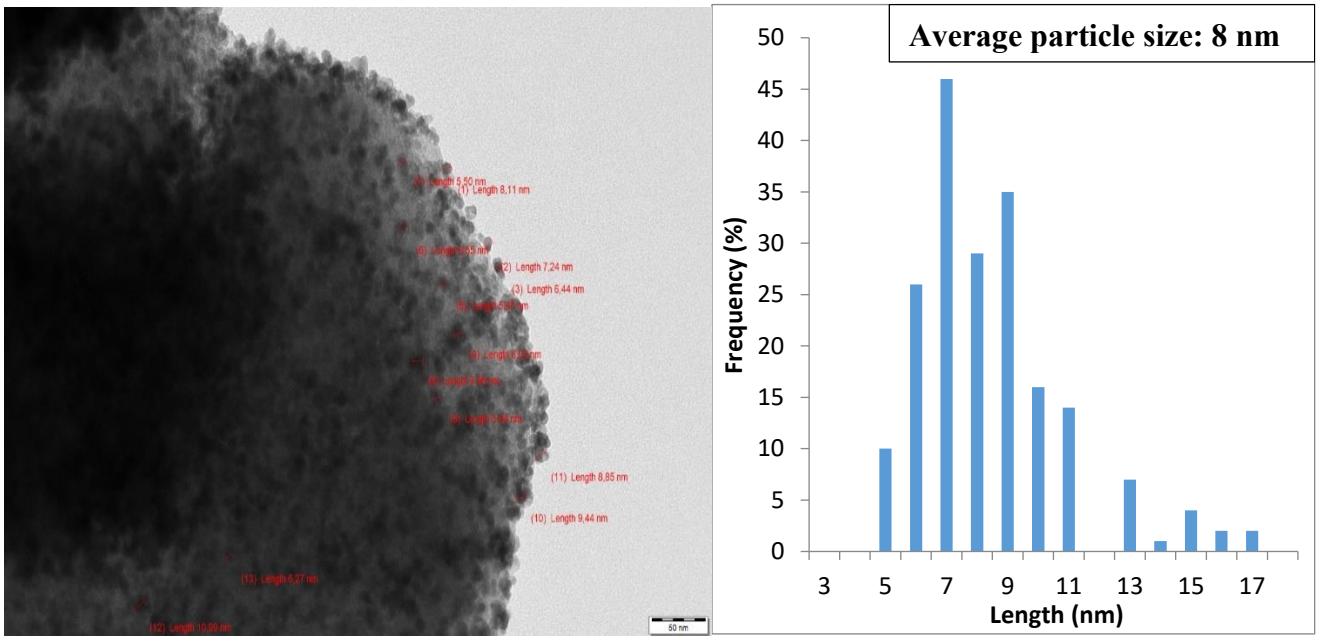

Figure 16: TEM micrograph (left) and the particle size distribution (right) of Sn-H-Y-30-EIM prepared with the tin (II) chloride precursor

In contrast, larger Sn particles (9.1 nm) were observed for Sn-H-Y-30-EIM catalyst prepared from $SnCl_4$ as compared to those prepared from $SnCl_2$ (8 nm). Furthermore, the average size of the metal nanoparticles, including Sn, K, Sr, and Cs described in Appendix III containing additional TEM images of alternative catalysts for reference.

The catalysts containing tin (Sn) synthesized using either tin (II) or tin (IV) chloride as precursors exhibited the presence of widely dispersed Sn nanoparticles in the transmission electron microscope (TEM) images. These nanoparticles displayed sizes ranging from 6 to 10 nm. However, in the catalysts prepared with the tin (IV) chloride precursor, slightly larger Sn particles were observed.

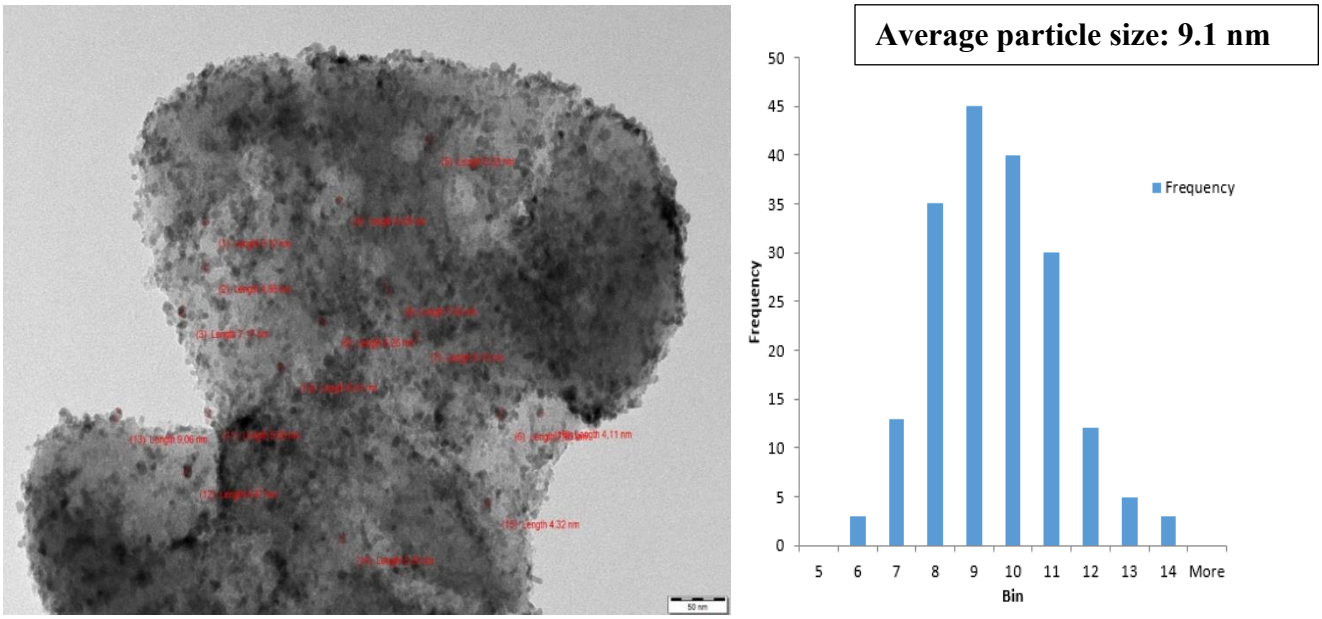

Figure 17: TEM micrograph (left) and the particle size distribution (right) of Sn-H-Y-30-EIM prepared with the tin (IV) chloride precursor

In **Figure 18**, TEM micrographs from four different catalysts are shown. In the first TEM micrograph a typical protonic form of Y zeolite with the SiO_2/Al_2O_3 ratio of 30 is visible. Typically, in the case of **a)**, TEM images of H-Y-30 zeolite show the presence of small crystallites with a size range of a few nanometers to several micrometers, depending on the synthesis conditions. The images also show the characteristic channels and cavities of the Y zeolite structure. In addition to the morphology, TEM characterization also provides information on the crystallinity and defects in the H-Y-30 zeolite[90]. For example, the images may reveal the presence of stacking faults, twinning, or other types of defects that can affect the performance of the catalyst. Overall, TEM characterization of typical H-Y-30 zeolite provides important information about its morphology, crystallinity, and defects, which can be useful for understanding its properties and optimizing its performance as a catalyst. Similar to other publications[91] on H-Y zeolites, it can be clearly seen that there is neither agglomeration nor considerable particle clustering.

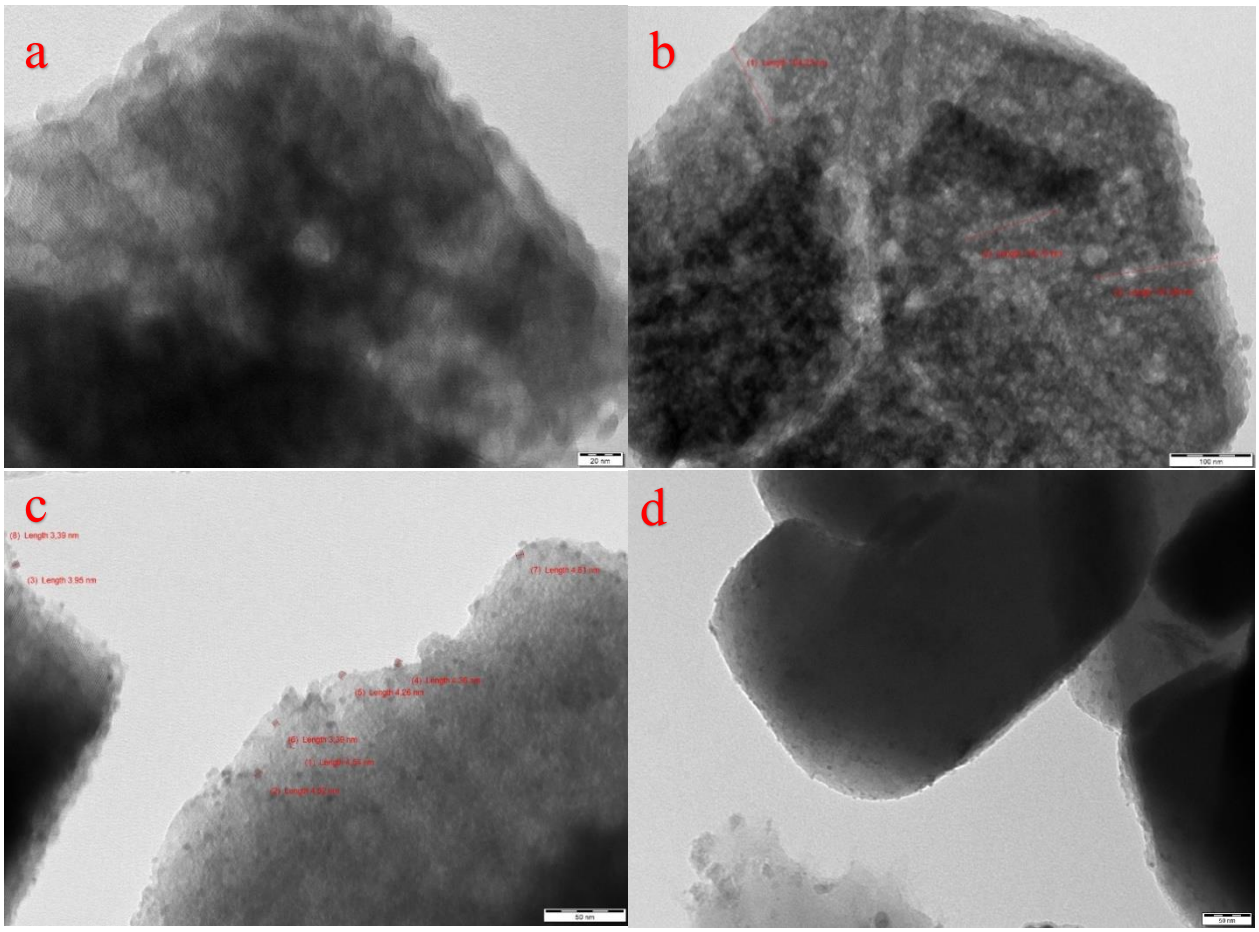

Figure 18: TEM micrographs of: a) H-Y-30 zeolite, b) H-Y-30-DA, meaning dealuminated H-Y-30 zeolite, c) K-Sn-H-Y-DA-fresh, d) K-Sn-H-Y-30-DA-spent catalyst after 24 h reaction

In **Figure 18, b)**, TEM characterization of typical H-Y-30 zeolite after dealumination with 10 M nitric acid reveals several changes in the morphology and structure of the zeolite. For example, the images of dealuminated Y zeolites demonstrate a decrease in the catalyst particle size and an increase in the surface area compared to the pristine H-Y (**Table 10**) zeolite with the SiO_2/Al_2O_3 ratio of 30 which is similarly reported.[92] This is because dealumination can break down the larger particles and open up new channels and cavities in the zeolite structure, resulting in a higher surface area[93]. Additionally, TEM characterization reveals changes in the crystallinity and framework of the zeolite after dealumination. The images display changes in the lattice spacing, indicating a change in the framework of the zeolite due to the removal of aluminium atoms. The images also show the presence of new defects or voids in the zeolite structure, which can affect the catalytic performance of the material such as discussed in another research of the similar type.[94] Overall,

TEM characterization of typical H-Y-30 zeolite after dealumination with nitric acid provide valuable information on the changes in morphology, structure, and particle size distribution of the zeolite. This information can be used to understand the effect of dealumination on the catalytic performance of the zeolite and to optimize the synthesis and processing conditions for specific applications.

In Figure 18-c, the TEM images of K and Sn modified dealuminated H-Y zeolite with the SiO_2/Al_2O_3 ratio 30 provide information about the morphology, size, and distribution of metal nanoparticles on the catalyst surface. As it can be seen from the image which reveals the distribution and aggregation of the metal nanoparticles and the extent to which they are located on the external surface of the catalyst particle. The challenge was to differentiate the Sn and K particles due to their closer particle sizes which was also previously reported in literature[95]. On the other hand, pores and channels of Y zeolite were intact even after synthesis and modifications[96]. Even though metal particles on the catalyst surface is clearly visible, it is difficult to assess if placement of metal particles in the catalyst channels has been succeeded. Additionally, the images from various parts of the catalysts by doing spot analysis provided insights into the crystalline structure and porosity of the zeolite support and any changes that may have occurred due to the modification.

In Figure 18-d, TEM micrograph of K and Sn modified dealuminated spent H-Y zeolite with the SiO_2/Al_2O_3 ratio of 30 is shown. In general, TEM images of the fresh and spent catalysts can reveal important differences in the morphology, size, and distribution of the metal nanoparticles on the catalyst surface before and after the reaction. Moreover, the fresh H-Y catalysts typically exhibit well-defined crystalline structures with regular pore arrangements. In the spent catalysts, structural changes like framework collapse, dealumination, or the formation of secondary phases may be observed, leading to alterations in particle morphology and size[97]. The fresh catalysts exhibited a more uniform distribution of metal nanoparticles with a smaller particle size and a more homogeneous morphology. In contrast, the spent catalysts showed signs of sintering, aggregation, or migration of the metal nanoparticles, resulting in a larger particle size, uneven distribution, and a less uniform morphology. Furthermore, the spent catalysts may also exhibit changes in the zeolite support, such as dealumination, pore blockage, or collapse[96]. Such negative issues as the pore blockage, collapse and changes in the zeolite support were also observed, which further affect the catalyst activity and selectivity. Overall, a comparison of the TEM images of the fresh and the

spent H-Y-30 zeolite can provide insights into the factors that contribute to the catalyst deactivation and its impact on the catalyst performance and stability. TEM images of the spent H-Y catalysts also revealed the presence of carbonaceous deposits (coke) on the catalyst surface or within the pores. Deposited coke was observed in the amorphous form on the surface of the catalyst as reported in the literature[98].

The average particle sizes of the spent Sn, K, and K-Sn catalysts synthesized on the dealuminated H-Y-5.1, H-Y-30 and H-Y-80 support were slightly larger than those for the fresh catalysts by 2-5%. This confirms that there was sintering of Sn and K nanoparticles during the reaction as analogously observed in lactic acid formation from glycerol[99].

Fourier-transform infrared (FTIR) spectroscopy

The acidic properties, such as the amount of Brønsted and Lewis acid sites in the metal modified heterogenous H-Y catalysts, were determined using the FTIR pyridine adsorption-desorption method. The results are shown in two different tables in which the **Table 7** displays the FTIR pyridine acidity data for H-Y zeolites with varying SiO_2/Al_2O_3 ratios as well as with different Sn precursors that were used in the synthesis i.e. $SnCl_2$ and $SnCl_4$. Except for catalyst 4 ($SnCl_4$-H-Y-30-EIM), in all other catalysts introduction of Sn increased the number of Lewis acid sites, which as discussed in Section 4.2, decreased the yield of methyl lactate.

Table 7: Acidity measurements for H-Y zeolites synthesized by impregnation method

Catalysts	Brønsted acidity (μmol/g)			Lewis acidity (μmol/g)		
T (°C)	250 (W+M+S)	350 (M+S)	450 (S)	250 (W+M+S)	350 (M+S)	450 (S)
1. H-Y-5.1	336	194	65	16	0	0
2. Sn-H-Y-5.1-EIM	140	93	63	31	22	13
3. H-Y-30	146	121	13	13	9	1
4. Sn-H-Y-30-EIM	88	84	76	20	19	15
5. H-Y-80	24	21	6	15	9	0
6. Sn-H-Y-80-EIM	18	18	4	26	26	3
7. $SnCl_4$-H-Y-5.1-EIM	128	117	62	4	1	0
8. $SnCl_4$-H-Y-30-EIM	98	86	49	38	24	2
9. $SnCl_4$-H-Y-80-EIM	83	77	49	31	22	0

Notation: W+M+S: weak acid site, M+S: medium acid site, S: strong acid site

Very similar behaviour of the H-Y zeolites that were synthesized by evaporation impregnation method was also assessed and reported previously[100] in line with the results of this work. The reason that $SnCl_4$-H-Y-5.1-EIM (**Table 6, entry 7**) catalyst showing different behaviour by having very small total Lewis acid sites concentrations of 4 μmol/g can be explained by the low pH of the metal precursor solution which could have resulted in destruction of Lewis acid sites in the process of synthesis[101]. Another interesting finding from this study is the relationship between SiO_2/Al_2O_3 ratio and the Brønsted acidity of H-Y zeolites. There is a substantial decrease in the number of Brønsted acid with increasing SiO_2/Al_2O_3 ratio. While Sn modified H-Y-5.1 zeolite with $SnCl_2$ precursor has total acidity of 140 μmol/g, another synthesized catalyst with SiO_2/Al_2O_3 ratio of 80 using the same method has the total acidity of 18 μmol/g as analogously reported[102]. Comparing the different precursors that were used during the synthesis of the catalysts it can be assessed that obviously there is a big difference in the strong Lewis acid sites between the catalysts that were prepared by $SnCl_2$ and $SnCl_4$ precursors. While Y zeolites with the SiO_2/Al_2O_3 ratio of 5.1 and 30 exhibited 13 μmol/g and 15 μmol/g strong Lewis acid sites, respectively at the temperature of 450 °C, the zeolites that were modified using the $SnCl_4$ precursor almost did not contain any strong Lewis acid sites as analogously reported[103].

On the other hand, **Table 8** shows the FTIR pyridine acidity measurements of the catalysts that were prepared by alkaline ion exchange method by following the recipe that was reported[82]. As it was also the purpose of dealumination, in the K and Sn modified dealuminated catalysts no strong acid sites were detected. This result indicates that dealumination was successfully achieved. However, variations in all acid sites for different types of catalyst are clearly visible (Table 11). For example, entry 2 and entry 5 catalysts, which were modified with K and Sr as bimetallic compounds, exhibited higher total Lewis acid sites than others being 27 μmol/g and 25 μmol/g, respectively for those catalysts the expected yield of methyl lactate decreased after 24 h reaction time. Interestingly, the catalyst Sr-Sn-H-Y-30-DA (Table 11, entry 6) exhibited high Brønsted acidity even at high temperatures analogously to previously reported[104]. For materials containing the cationic metals and specifically strontium which were used in the methanol to olefins reaction.

Overall, for all catalysts that are displayed in **Table 8**, it was found that introduction of Sn decreased the concentration of Brønsted acid sites, while the K modification resulted in a higher

concentration of acid sites with 25 μmol/g of total Brønsted concentration in average in comparison to those for Sr and Cs modified catalysts being 15 μmol/g and 11 μmol/g, respectively.

Table 8: Acidity measurement of H-Y zeolites by alkaline ion exchange method

Catalysts	Brønsted acidity (μmol/g)			Lewis acidity (μmol/g)		
T (°C)	250 (W+M+S)	350 (M+S)	450 (S)	250 (W+M+S)	350 (M+S)	450 (S)
1. H-Y-30	146	121	13	13	9	1
2. K-Sn-H-Y-30-DA	41	13	0	5	5	0
10. K-Sn-H-Y-30-DA-2	20	16	0	27	6	0
11. K-Sn-H-Y-30-DA-3	21	17	0	6	5	0
12. K-Sn-H-Y-30-DA-4	17	0	0	4	0	0
13. Sr-Sn-H-Y-30-DA	15	13	12	25	5	4
14. Cs-Sn-H-Y-30-DA	11	0	0	7	0	0

Notation: W+M+S: weak acid site, M+S: medium acid site, S: strong acid site

The decrease of Brønsted acid sites after Sn modification suggests that Sn modification influenced the type and strength of acid sites present in the zeolite, possibly due to the interaction between Sn species and the framework. On the other hand, the acidity change after K modification suggests that K cation exchange enhanced the acid properties of the zeolite, potentially due to the interaction between K ions and the framework again, leading to the generation of additional acid sites[105]. By examining the effect of Sn and K on the acidity of H-Y zeolite, the study provides insights into the structural modifications and their consequences for the catalytic performance of these zeolite materials. The findings contribute to a better understanding of the relationship between acidity and catalytic activity in Sn and K modified H-Y zeolites, which can be beneficial for the design and optimization of zeolite catalysts for various applications.

To understand the change in the catalyst acidity based on the steps of synthesis, **Figure 19** displays the combined FTIR pyridine spectra of 4 different catalysts. The band around the wavenumber of 1550 cm^{-1} corresponds to Brønsted acidity and the one around 1450 cm^{-1} reflects the Lewis acidity of the catalyst[106]. The spectra correspond the total acid sites of the catalysts that were detected at 250 ºC.

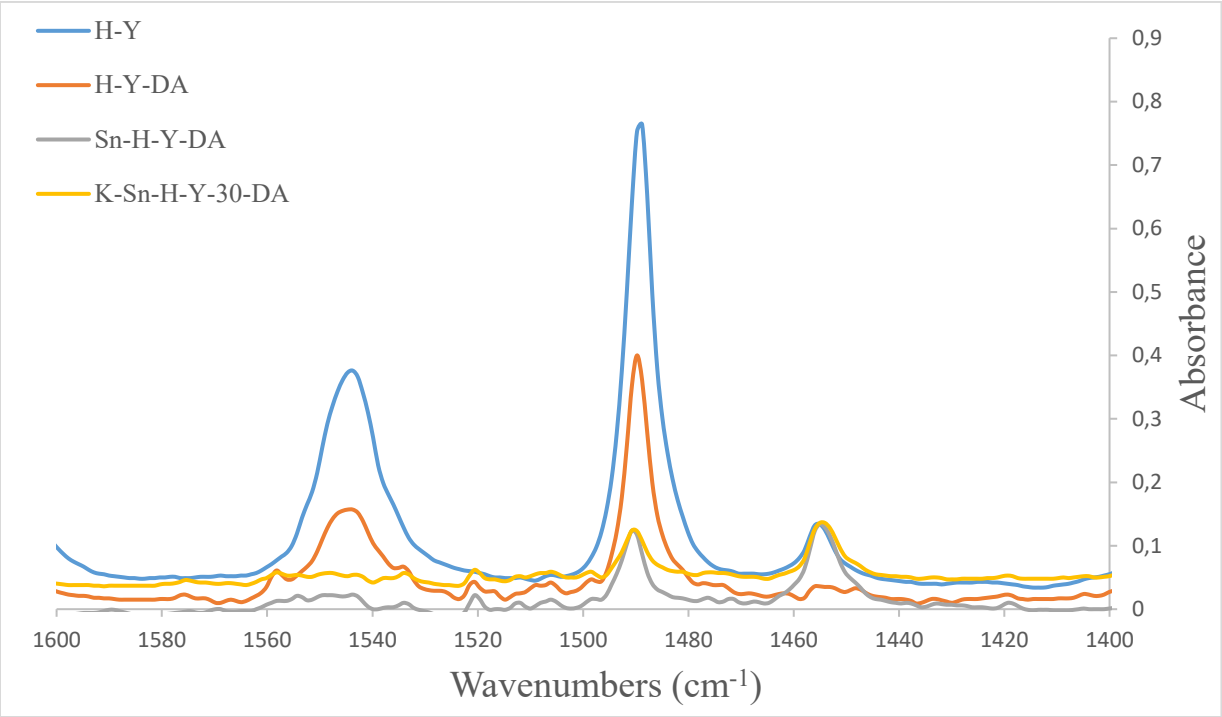

Figure 19: Combined FTIR pyridine acidity measurement spectra of H-Y zeolites

Commencing with the protonic form of H-Y zeolites, the corresponding spectrum, depicted by the blue plot, exhibits a notably high absorbance signal of Brønsted acid sites. Significantly, upon the subsequent dealumination process employing a 10 M nitric acid solution, it becomes evident that the total count of Lewis acid sites diminishes substantially, as expected. Concurrently, a reduction in the number of Brønsted acid sites is observed, in agreement with the existing literature data[107]. Analogously, as documented in Table 11, the introduction of Sn follows a comparable pattern, wherein the total population of Brønsted acid sites declined, as illustrated in **Figure 19**. Notably, the inclusion of Sn, being a Lewis acid itself, contributes to appearance of additional Lewis acid sites. The yellow spectrum for dealuminated H-Y zeolite with SAR of 30 confirms the characteristic behavior of the bimetallic catalyst. Consistent with a prior report[107], the introduction of K results in an increase of the overall Brønsted acidity. Conversely, the impact of K on the total number of Lewis acid sites in the zeolites appears to be relatively minimal, as indicated by the marginal disparity observed before and after the addition of K.

Temperature programmed desorption (TPD) of CO_2

Basicity analysis for one of the best performing catalysts (K-Sn-H-Y-30-DA) was performed and the results indicated that no detectable basicity was observed.

Nitrogen physisorption

The Dubinin-Radushkevich surface areas and the DFT pore volumes of H-Y zeolites which were synthesized by evaporation impregnation method studied using nitrogen physisorption are given in **Table 9**. The results indicated that the incorporation of Sn into the H-Y zeolite framework led to a decrease in the surface area compared to the pristine zeolite. Overall, the average surface area of 500 m^2/g and typical pore volume for microporous material of about 0.25 cm^3/g revealed alterations in the pore size distribution such as 18 % increase in the ratio of mesoporous to microporous total pore volumes compared to the unmodified H-Y-30 zeolite. The highest change in the mesoporous to microporous pore volume ratio was detected in H-Y-80 zeolite in which it was doubled after introduction of tin. The surface area of Sn-H-Y-80-EIM catalyst decreased to 512 m^2/g being 665 m^2/g for the pristine zeolite as can be seen in **Table 9**.

Table 9: N_2 Physisorption results of the impregnated catalysts

N	Catalyst	Surface Area (m^2/g)	Total Pore Volume (cm^3/g)	Micro-P (%)	Meso-P (%)	V_{meso}/V_{micro}
1.	H-Y-5	590	0.26	93	7	0.07
2.	Sn-H-Y-5-EIM	504	0.22	97	3	0.03
3.	H-Y-30	1200	0.57	78	22	0.28
4.	Sn-H-Y-30-EIM	527	0.25	75	25	0.33
5.	H-Y-80	665	0.33	82	18	0.22
6.	Sn-H-Y-80-EIM	512	0.27	68	32	0.47

Notably, impregnated zeolites exhibit a correlation between the SiO_2/Al_2O_3 ratio (SAR) and the ratios of total mesopore volume to micropore volume. Specifically, commencing from the pristine H-Y-5 zeolite, an elevated SiO_2/Al_2O_3 ratio leads to a substantial increase in the mesopore/micropore ratios as shown in **Figure 20**. This phenomenon is evident in the observed ratios of 0.47 for Sn-H-Y-80-EIM and a considerably lower value of 0.03 for Sn-H-Y-5-EIM.

Overall, the N_2 physisorption results demonstrated that the impregnated H-Y zeolites with Sn led to a decrease in the specific surface area, and an increased ratio for mesoporous to microporous

ratio (V_{meso}/V_{micro}). These modifications can be attributed to the incorporation of Sn species, which influenced the physicochemical properties and porosity of the zeolite framework[108].

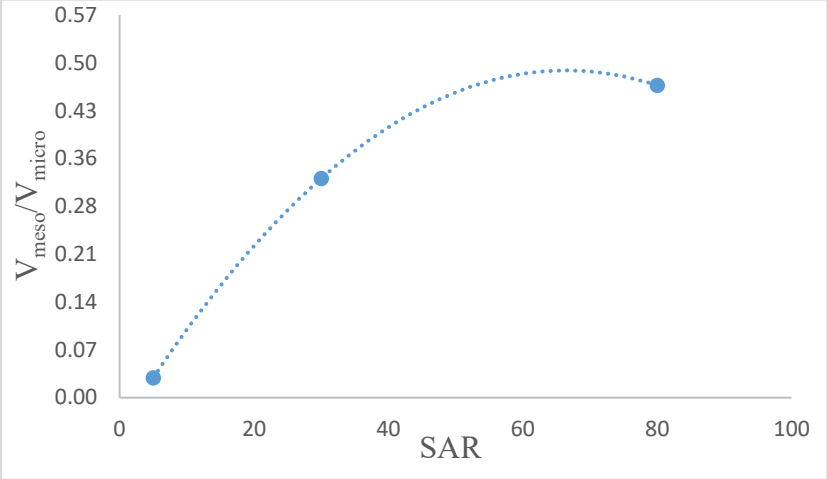

Figure 20: Relationship between SiO_2/Al_2O_3 (mol/mol) ratios and V_{meso}/V_{micro} of impregnated catalysts

Moreover, a typical microporous adsorption-desorption isotherm of the dealuminated H-Y zeolites and further modified with Sn and K is shown in **Figure 21**.

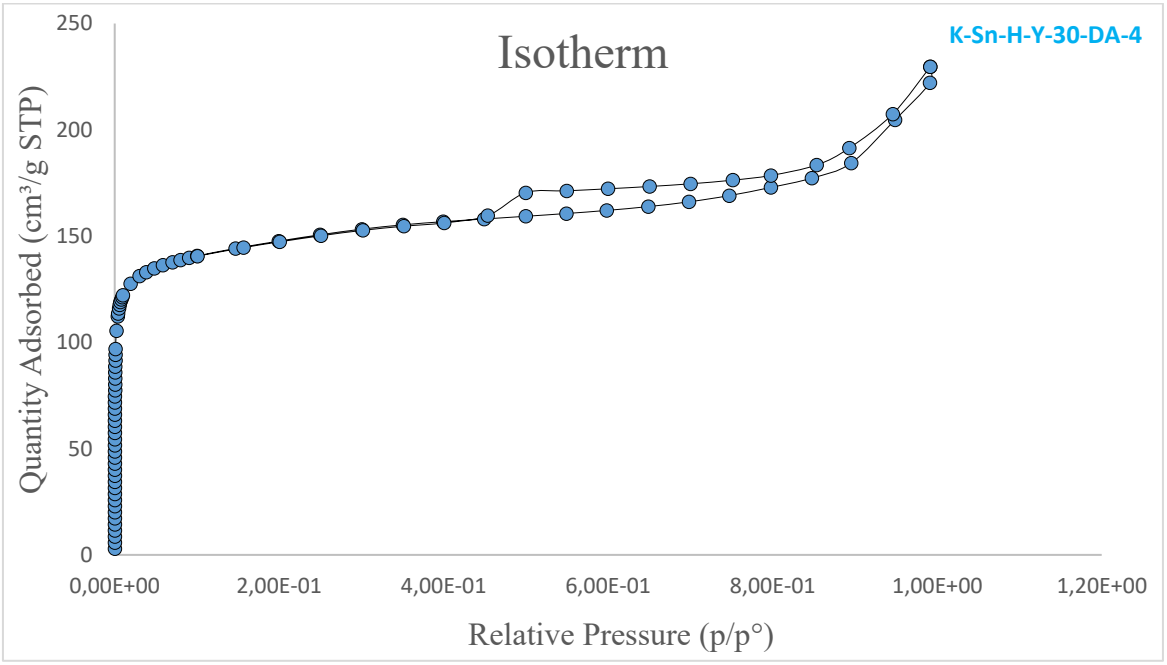

Figure 21: N_2 adsorption-desorption isotherm of Sn and K modified dealuminated H-Y-30 zeolite

Table 10 shows the results from N_2 physisorption of dealuminated and ion exchanged modified metals with Sn and K. The N_2 physisorption results for ion-exchanged dealuminated H-Y zeolites with Sn and K yielded several significant findings. The results indicated that the ion exchange of dealuminated H-Y zeolites with Sn and K led to decrease in the surface area compared to the pristine zeolite. For example, the TEM images of dealuminated Y zeolites show a decrease in the catalyst particle size (**Figure 18**) and an increase in the surface area compared to the untreated H-Y (**Table 10**) zeolite with the SiO_2/Al_2O_3 ratio of 30 which is very similar to previously reported.[92] Thereafter, the H-Y-30 zeolite surface area was measured to be ca. 1200 m^2/g containing almost only the micropores. After dealumination and modification with metals (Sn, K) the final catalyst exhibited the surface area of 550 m^2/g with 40% of mesopores favouring the reaction (Section 4.2). Specifically, for this reason the catalyst demonstrated very high selectivity and yield compared to other catalysts. Generally speaking, changes in the surface area could be attributed to the presence of Sn and K ions, which affected the pore structure resulting in a substantial increase in the total mesopore to micropore volumes (V_{meso}/V_{micro}), being 2.28 and 2.04 times higher for H-Y-30 and H-Y-80, respectively.[109]

Table 10: N_2 Physisorption results of dealuminated and bimetallic H-Y zeolites

N	Catalyst	Surface Area (m^2/g)	Total Pore Volume (cm^3/g)	Micro-P (%)	Meso-P (%)	V_{meso}/V_{micro}
1.	H-Y-30	1200	0.57	78	22	0.28
2.	H-Y-30-DA	790	0.37	76	24	0.32
3.	Sn-H-Y-30-DA	712	0.33	76	24	0.32
4.	K-Sn-H-Y-30-DA	547	0.30	61	39	0.64
5.	H-Y-80	665	0.33	82	18	0.22
6.	H-Y-80-DA	589	0.29	75	25	0.33
7.	Sn-H-Y-80-DA	604	0.30	73	27	0.37
8.	K-H-Y-80-DA	633	0.32	71	29	0.41
9.	K-Sn-H-Y-80-DA	579	0.30	69	31	0.45

As mentioned before, another interesting finding was to see how the meso-porosity is changing throughout the synthesis steps of the zeolites. While H-Y zeolite with the SiO_2/Al_2O_3 ratio of 80 has only 18% mesopores of all pores, the final synthesized catalyst, K-Sn-H-Y-80-DA exhibited 31% of mesopores. Again, this confirmed that the dealumination of the zeolites was successfully achieved in almost all cases.

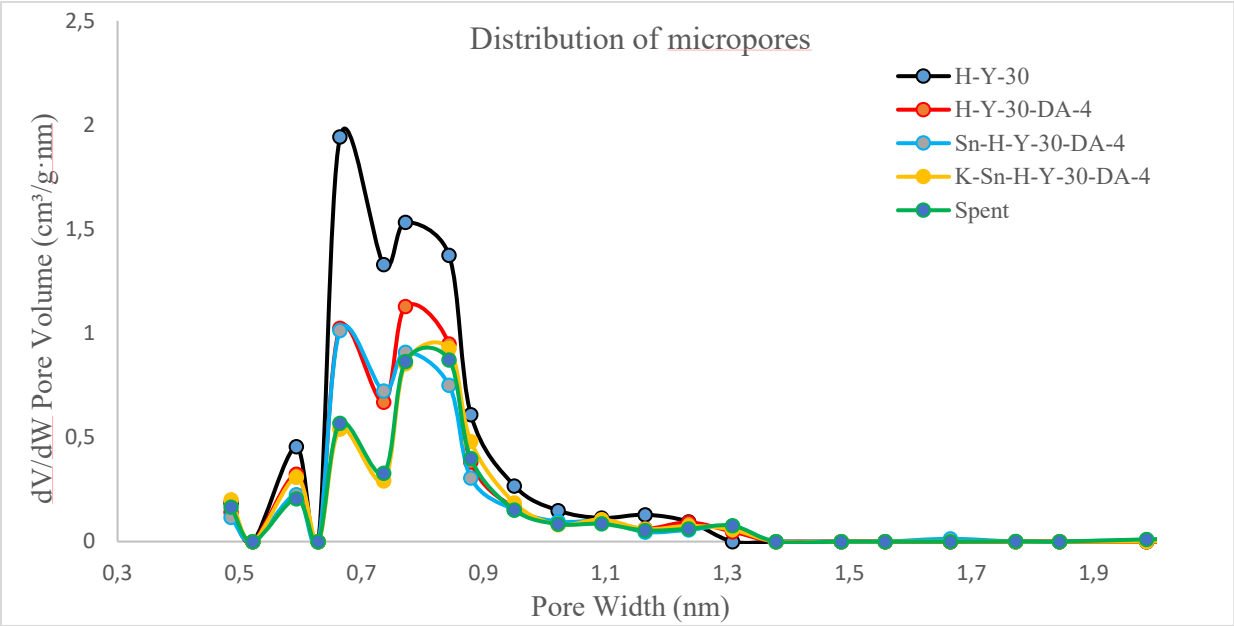

Figure 22: Distribution of the micropores of K-Sn-H-Y-30-DA-4 zeolite

To have better understanding in the textural properties of the zeolites, materials after different preparation steps were characterized. **Figure 22** delivers very informative data and helps in understanding the changes in a much better way. Starting from the proton form of the H-Y zeolite with the SiO_2/Al_2O_3 ratio of 30, it can be seen that the zeolite has a very high pore volume in the micropores of ca. 0.7-0.8 nm. A very big change after dealumination of the zeolite can be observed very easily. This is due to creation of more mesopores after dealumination with nitric acid leading to less micropores. Even though it is difficult to see the difference of the spent catalysts compared to the fresh one in **Figure 22**, **Table 11** can be however used to understand the change in the textural properties of the zeolites after the reaction. The N_2 physisorption results of the fresh and spent H-Y zeolites exhibit notable differences, indicating changes in the pore structure and surface properties of the zeolites after their usage or exposure to specific conditions as clearly can be seen from **Table 11**. One prominent distinction is the decrease in the specific surface area of the spent zeolites compared to their fresh counterparts[110]. For instance, according to Table 10, for the best catalyst (entry 1) a decrease in the surface area from approximately 550 m^2/g to around 510 m^2/g was detected. Notably, the dealuminated H-Y-80 catalyst (entry 4) exhibited no significant changes in the surface area, maintaining a constant value of 590 m^2/g even after the reaction. On the other hand, other dealuminated and metal-modified H-Y zeolites displayed minor fluctuations in surface areas within the range of 88-95%. Furthermore, the impregnated catalysts showed a wide range of

variation in surface areas. The decline in the surface area of the spent catalysts can be attributed to factors such as accumulation of the reaction by-products, coking, or fouling on the zeolite surface during the catalytic process[111].

In an unexpected manner, the spent Sn-H-Y-5-EIM catalyst exhibited a noteworthy 22% increase in the surface area, reaching a value of 610 m^2/g. This increase can be attributed to several factors, including the removal of carbonaceous deposits or coke that formed during the reaction, the restructuring or redistribution of active species on the catalyst surface, and potential alterations in the catalyst pore structure[112]. A related observation can be found in **Table 11**, which provides insights into changes in the micro and mesopores. While all catalysts demonstrated a decrease in the total micropore volumes and an increase in the total mesopore volume, entry 3 displayed an unaltered pore distribution, maintaining the same proportions of 71% micro- and 29% mesopores. In opposite, the Sn-H-Y-5-EIM catalyst exhibited a dramatic alteration in micro/mesoporosity. These significant changes in the catalyst pore characteristics, such as the increase in the mesopore volume and decrease in the micropore volume, can be explained by structural transformations and modifications that result in the formation of new mesopores or the enlargement of existing ones[111]. These transformations may arise from diverse phenomena, including the redistribution or removal of specific species on the catalyst surface, the restructuring or agglomeration of catalyst particles, or the formation and subsequent removal of coke or carbonaceous deposits[111].

Table 11: N_2 Physisorption results of the spent and the fresh catalysts after 24 h reaction

N	Catalyst	Surface Area (m^2/g) [Fresh]	SA_{spent}/SA_{fresh} (%)	Total Pore Volume (cm^3/g) [Fresh]	Micro-P (%) [Fresh]	Meso-P (%) [Fresh]
1.	Spent-K-Sn-H-Y-30-DA	514 [547]	94	0.30 [0.30]	55 [61]	44 [39]
2.	Spent-K-Sn-H-Y-80-DA	513 [580]	88	0.27 [0.30]	66 [69]	34 [31]
3.	Spent-K-H-Y-80-DA	600 [630]	95	0.31 [0.32]	71 [71]	29 [29]
4.	Spent-H-Y-80-DA	590 [590]	100	0.30 [0.29]	68 [75]	32 [25]
5.	Spent-H-Y-80	490 [580]	84	0.26 [0.25]	66 [72]	34 [28]
6.	Spent-Sn-H-Y-5-EIM	610 [500]	122	0.22 [0.22]	69 [97]	31 [3]
7.	Spent-Sn-H-Y-30-EIM	440 [530]	83	0.24 [0.25]	65 [75]	35 [25]
8.	Spent-Sn-H-Y-80-EIM	470 [510]	92	0.25 [0.27]	64 [68]	36 [32]

The presence of coke or other deposits can lead to changes in the accessibility and availability of different pore sizes, resulting in a modified pore size distribution[113]. The shape of the N_2 adsorption isotherms can vary between fresh and spent H-Y zeolites. The hysteresis loops observed in the N_2 adsorption-desorption isotherms was observed to be slightly different between fresh and spent H-Y zeolites due to presence of coke or other species in spent catalysts leading to lateral interactions[114]. Changes in the size, shape, or connectivity of the zeolite pores due to coke deposition or other factors can influence the occurrence and shape of hysteresis loops. These differences in the N_2 physisorption results between fresh and spent H-Y zeolites provide valuable information about the changes occurring in the zeolite structure and properties during catalytic reactions or prolonged usage. Understanding these differences can aid in assessing the stability, regeneration potential, and overall performance of H-Y zeolites in various applications[114].

4.2. Catalytic results

To investigate the hydrogenation activity, a control experiment was conducted in the absence of a catalyst. Glucose was utilized as the reactant, while methanol served as the solvent. The experiment was carried out under specific conditions of 180 °C temperature and a total pressure of 30 bar for a duration of 24 hours. By running a blank reaction with glucose in methanol, it can be assessed if methyl lactate may be generated in the reaction system without a catalyst. The same operating parameters were used previously[82] for methyl lactate reaction from glucose in a blank reaction where no catalysts was used. As mentioned earlier, the sugar (solid) components were measured using the HPLC, while the products after 24 hours were quantified using GC for the liquid phase.

As can be observed from **Figure 23**, a complete conversion of glucose was obtained under the used operating conditions without any catalyst after 24 hours. Even though only 46% conversion of glucose was achieved after 6 h at 150 °C [4], in the current work more than 70% conversion was already detected after 3 h at 180 °C using the same pressures. This is clearly related to a higher temperature leading to an increase in reaction[115]. Rapid isomerization of glucose to fructose already took place in the first minutes of the experiment as reported in the literature[4]. While the glucose conversion was almost 100% after the reaction, other sugars such as D-mannose and alfa methyl-glucosides were also detected in very small amounts by HPLC which are the result from the condensation of methanol with monosaccharides, as previously detected[4].

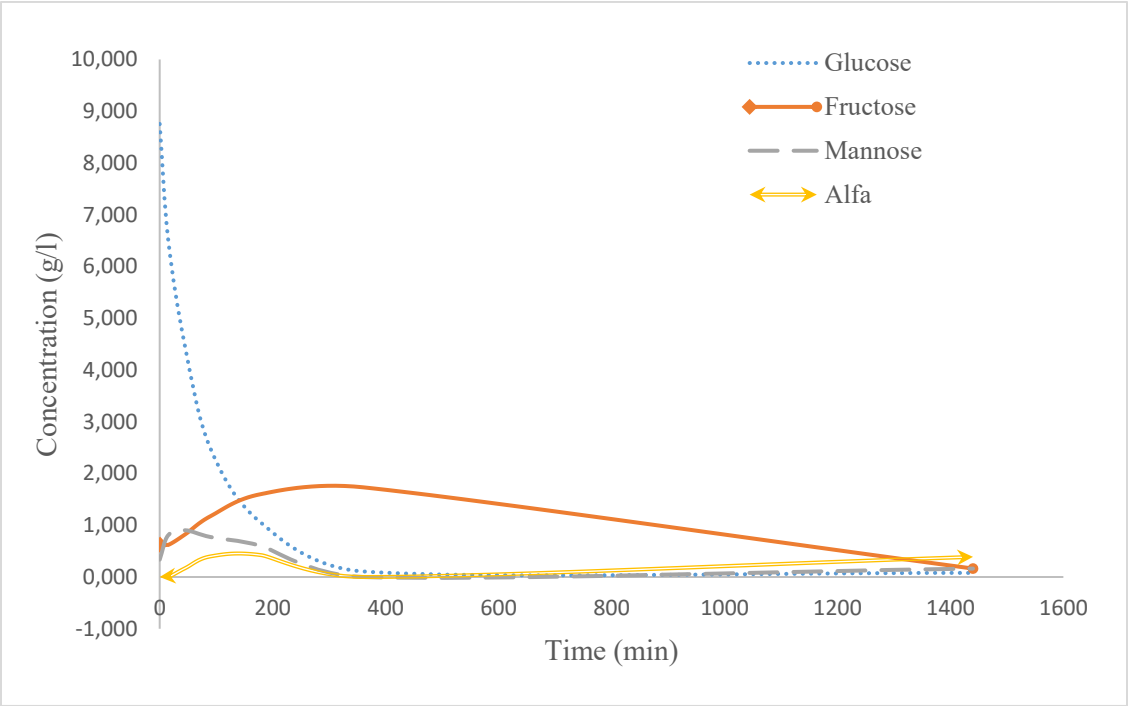

Figure 23: Conversions of sugars in the absence of any catalyst after 24 h (Reaction conditions: liquid volume, 100 ml; glucose concentration, 9 g/l; 180 °C, 30 bar)

Figure 23 also gives information about the products analysed by HPLC that were detected after the reaction. The blank experiment in the absence of a catalyst resulted in the formation of very low yields of methyl lactate (<10%) and ca. 1% of methyl levulinate was also formed at the end of the reaction. Majority of the reaction products were identified using GC-MS. Small amounts of various by-products such as furfural, methyl-formate, 1,3-dihydroxyacetone, methyl vinyl glycolate, etc. were formed each exhibiting less than 2% yields after 24 h of the reaction.

Methyl lactate formation reaction on evaporation impregnated catalysts with Sn

The further reactions were conducted with a set of catalysts synthesized using the same preparation method reported in the experimental part of the thesis. This set corresponds to H-Y zeolites with varying SiO_2/Al_2O_3 ratios of 5.1, 30 and 80 and two different metal precursors ($SnCl_2$ and $SnCl_4$). Overall, as it can be seen from **Figure 24** that all the catalysts resulted in full conversions (100%) of glucose within 24 hours. All impregnated catalysts exhibited similar sugar concentration curves where after 3 h of reaction, glucose and fructose were fully converted into such products as D-mannose and alfa methyl glucosides in addition to methyl lactate and methyl levulinate[116].

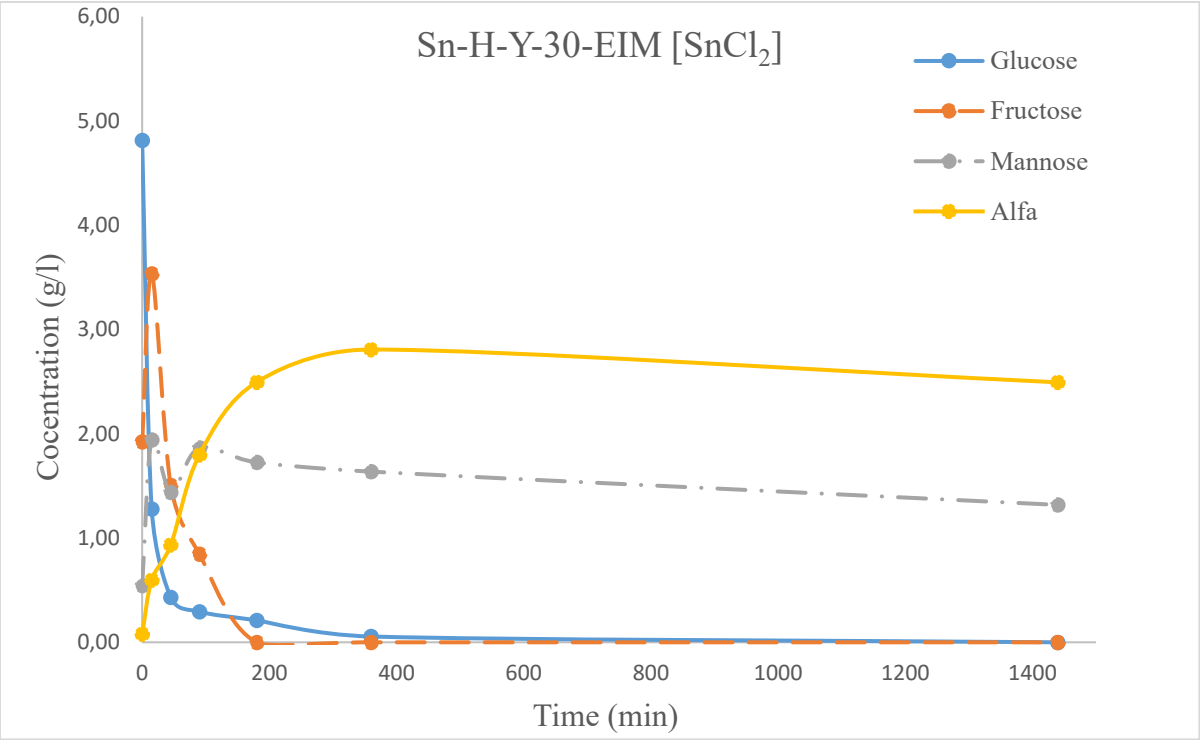

Figure 24: Conversions of sugars in Sn-H-Y-30-EIM [$SnCl_2$ precursor] (Reaction conditions: liquid volume, 100 ml; glucose concentration, 9 g/l; 180 °C, 30 bar)

The yields of the products, which were quantified by GC, are given in **Table 12** together with concentrations of those analyzed by HPLC in **Figure 24**. Very high yields of D-mannose and alfa-methylglucosides after 24 h. Remarkably, impregnated zeolites with $SnCl_2$ precursor gave higher glucoside yields being 38, 28 and 40 %, for synthesized zeolites with SiO_2/Al_2O_3 ratios of 5.1, 30 and 80, respectively.

Table 12: Yields of products for Sn-H-Y zeolites made by evaporation impregnation (Reaction conditions: liquid volume, 100 ml; glucose concentration, 9 g/l; 180 °C, 30 bar, complete conversion of sugars)

Type of precursor	Catalyst	MB (%)	Me-lactate (%)	Me-levulinate (%)	D-Mannose (%)	Alfa-methyl glucoside (%)
$SnCl_2$	Sn-H-Y-5.1-EIM	94	1	25	24	38
	Sn-H-Y-30-EIM	92	2	35	15	28
	Sn-H-Y-80-EIM	95	8	14	23	40
$SnCl_4$	Sn-H-Y-5.1-EIM	96	7	18	7	8
	Sn-H-Y-30-EIM	n/a	4	42	11	20
	Sn-H-Y-80-EIM	95	11	11	15	30

Furthermore, very high methyl levulinate yields were also obtained specifically, the highest methyl levulinate yield of 42% was recorded in the presence of Sn-H-Y-30-EIM catalyst which was synthesized using $SnCl_4$ precursor. In general, the impregnated catalysts exhibit large amounts of strong acid sites (Table 6) and according to the literature[116], more methyl levulinate is formed over Brønsted acidic catalysts.

Even though promising results from the impregnated catalysts were expected, only low yields of methyl lactates varying from 1 to 11%, as being 11% for Sn-H-Y-80-EIM ($SnCl_4$ precursor) were achieved. As a comparison with the literature it can be stated regarding:

Catalyst selectivity: H-Y zeolites impregnated with Sn metal may exhibit higher selectivity towards mannose in the range of 7-24% and alpha-methylglucosides with the selectivity between 8-40 % under specific reaction conditions. The active sites on the catalyst surface, along with the presence of Sn species, may favor formation of these products at the expense of methyl lactate[117].

Reaction pathways: Glucose to methyl lactate transformations and the formation of mannose and alpha-methylglucosides involve different reaction pathways. The presence of Sn on the catalyst surface can influence the reaction kinetics and favor specific pathways leading to formation of mannose and alpha-methylglucosides[117].

Reaction conditions: The reaction conditions, such as temperature, pressure, and reactant concentrations, can influence the product distribution. It is possible that under the specific reaction conditions employed in the studies with H-Y zeolites impregnated with Sn metal, formation of mannose and alpha-methylglucosides is favored over methyl lactate. However, because similar reaction temperatures were tested and higher methyl lactate yields were previously reported[38], this may not be the reason behind the results of the current work different from previously reported.

Catalyst stability: Stability of the catalyst, particularly interactions between the Sn species and the zeolite support, can affect selectivity. The presence of Sn metal on H-Y zeolites may create specific active sites or alter acidity of the catalyst, leading to the preferential formation of mannose and alpha-methylglucosides[118].

In general, as can be seen from **Table 12**, increasing SiO_2/Al_2O_3 ratios actually slightly increased the yields of methyl lactate while methyl levulinate in all cases was also the dominant product. This means that the reactions have mostly proceeded into the direction of undesirable products

yielding more levulinates and glucosides as previously reported[82]. This can be explained by changes in acidity of the H-Y zeolites which depends on SiO_2/Al_2O_3 ratio. Higher SiO_2/Al_2O_3 ratios result in lower acidity due to decreased concentrations of acidic sites[119]. Catalyst acidity can influence the reaction kinetics and selectivity, potentially decreasing the yield of methyl lactate such as in the reaction where Sn-H-Y-5.1-EIM ($SnCl_2$ precursor) exhibited only 1 % methyl lactate yield (**Table 12**).

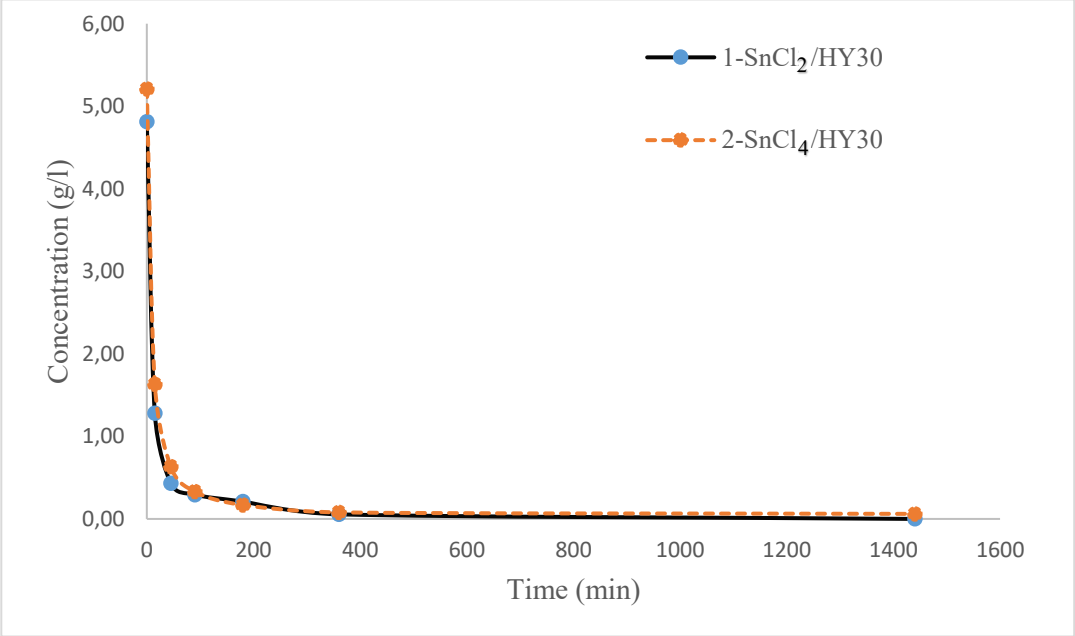

Figure 25: Conversions of sugars on impregnated catalysts with different precursors of Sn (Reaction conditions: liquid volume, 100 ml; glucose concentration, 9 g/l; 180 °C, 30 bar)

Figure 25 reports conversion of glucose on H-Y-30 zeolites impregnated using two different precursors, the first one being the tin (II) chloride and the second tin (IV) chloride, respectively. Regardless of the precursor almost the same concentration curves were obtained.

Methyl lactate formation reaction on dealuminated alkaline ion exchanged bimetallic catalysts with Sn and K

Catalytic testing was continued, as previously, in a batch mode with 0.75 g of the catalyst, 0.9 g of glucose, and 75 ml of methanol at 150 °C and 30 bar upon intensive stirring (720 rpm). Sn and K-modified bimetallic H-Y zeolites have shown promising catalytic performance in the transformation of glucose to methyl lactate. The bimetallic catalysts that were modified by Sn and

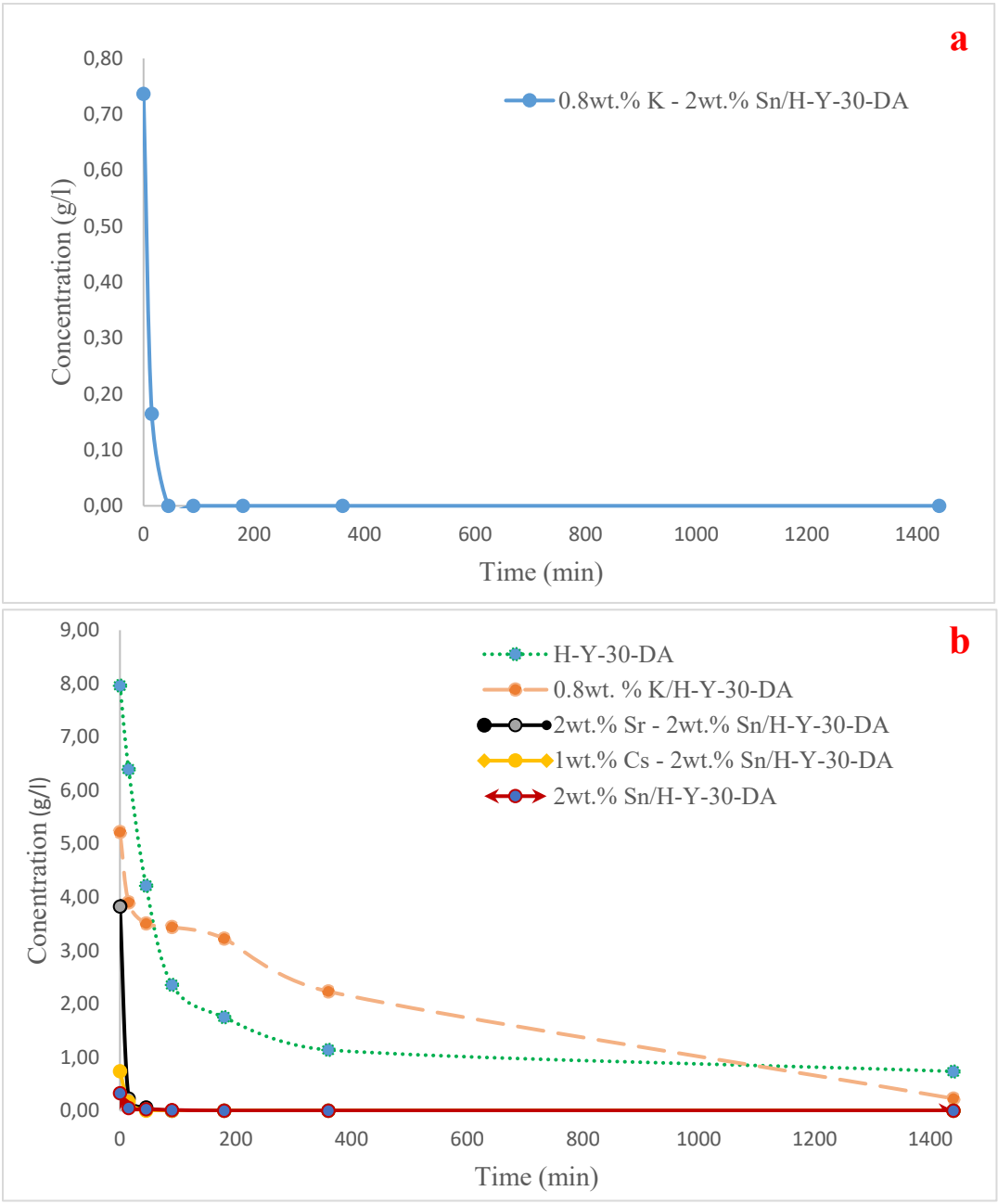

Figure 26: Glucose concentration curves over K/Sn modified (a) and other dealuminated catalysts (b) (Reaction conditions: liquid volume, 75 ml; glucose concentration, 12 g/l; 150 °C, 30 bar)

K exhibited high activity being able to reach full conversion within an hour of the reaction time. Throughout this work, these catalysts exhibited high activity, selectivity, and as well stability without visible changes in TEM, making them suitable for this transformation. As K-Sn-H-Y-30-DA has been the best catalyst for the transformations of glucose to methyl lactate among the tested materials, **Figure 26** depicts the glucose conversions of some other catalysts that were synthesized

and tested. From the concentration curves the clear differences in activity can be observed; namely that bimetallic catalysts that are modified sith Sn and another alkaline earth metals such as K, Cs as well as Sr exhibited very high rates of glucose transformation. The monometallic 2 wt.% Sn/H-Y-30-DA catalyst also exhibited very high rates even though not reaching high methyl lactate yields as those bimetallic catalysts ultimately yielding only 30% yield. Previously, very fast reaction rates of glucose to methyl lactate were reported[9,38,82]. Sn and K modification of H-Y zeolites enhanced the catalytic activity for glucose transformation to methyl lactate resulting 4-5 times faster reaction rates. It was also stated in[120] that the presence of Sn species promoted the cleavage of the C-C bond in glucose, facilitating formation of the intermediates and the desired product. K modification improves the accessibility of the reactants to active sites as a result of decrease in Brønsted acidity and creation of mesopores as discussed in the Sections 4.1.4 and 4.1.6, therefore, enhances the overall ML yield up to 70%[120].

Sn and K-modified H-Y zeolites have demonstrated high selectivity towards methyl lactate. The highest yield of methyl lactate was 72 % obtained over K-Sn-H-Y-30-DA-4 catalyst (**Figure 27**). The presence of Sn and K species help to promote the desired reaction pathways leading to the formation of methyl lactate. In general, H-Y zeolites are known for their acidic nature, which can influence the reaction kinetics and selectivity[121]. The introduction of Sn and K species modifies acidity of the zeolite, creating a balance between the acid and base sites. This adjusted low Lewis acidity helps in controlling the reaction pathways and enhances the selectivity towards methyl lactate formation[11]. K modification of H-Y zeolites improves the accessibility of reactant molecules to the active sites on the catalyst surface due to increased total mesopore volumes as discussed in the Section 4.1.6. This increased accessibility focused to modify the pore size distribution (specially, creating more mesopores and channels) facilitates the interaction between glucose and the catalyst, promoting the desired glucose transformation to methyl lactate[11]. During this study, many different catalysts using varying synthesis methods and procedures were used and tested. Among them, as it was previously also reported[11] Sn and K modified, dealuminated H-Y zeolites gave very high yields as can also be seen from **Figure 27**. Even though the dealumination step is very important for this reaction mechanism as also previously mentioned, it was observed that without metal modifications it is impossible to reach high yields of methyl lactate within reaction conditions. Only after introduction of Sn, a significant elevation in the yield of the desirable product

could be seen. Interestingly, without Sn, using only K in the monometallic catalyst the methyl lactate yield again dropped down to 6 %.

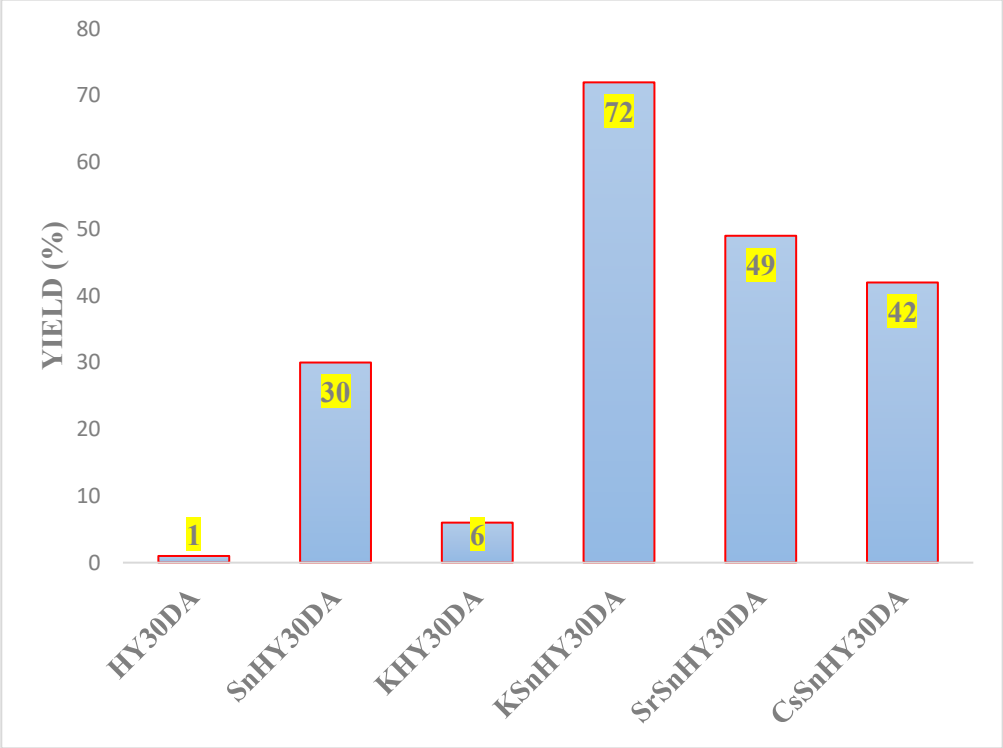

Figure 27: Glucose to ML over dealuminated catalysts (Reaction conditions: liquid volume, 75 ml; glucose concentration, 12 g/l; 150 °C, 30 bar)

This can again be explained by generation of active sites upon intorduction of Sn species which facilitate the desired reaction pathway, as previously stated. In contrast, K alone may not possess the same capability to generate active sites for efficient C-C bond cleavage[122]. By combining Sn and K species, the catalyst benefits from the unique properties and interactions of both components, leading to improved catalytic performance and selectivity in the glucose to methyl lactate conversion. The specific reasons for the superior performance of Sn and K together compared to K alone may vary depending on what specific reaction conditions and catalyst formulations used[122,123]. During this study, a number of physicochemical observations were discovered to account for the high activity of this catalyst. These findings revealed that the catalyst exhibited a notable combination of low Lewis and Brønsted acidity, while concurrently possessing a substantial number of mesopores and a relatively low loading of Sn (2 wt.%). Other metals not previously investigated in this reaction such as Sr and Cs were also tested. Interestingly, Sr-

modified catalyst exhibited more strong acid sites than Cs-modified one (**Table 8**), however the former one gave a higher methyl lactate yield of 49% while the other resulted in only 42% yield.

Influence of Sn loading

It was found throughout the studies that deposition of Sn and K species on the H-Y zeolite catalysts can significantly impact the catalytic performance. The influence of Sn loading on modified H-Y zeolites in the reaction of glucose to methyl lactate can vary and has been studied in several articles[124–126]. Increasing the Sn loading on H-Y zeolites can enhance the catalytic activity and selectivity towards methyl lactate formation. Typically, an optimal Sn loading range was reported to the highest yield of methyl lactate. Beyond this range, excessive Sn loading may result in catalyst deactivation or formation of the undesired by-products[127]. Sn loading affects the reaction kinetics, including the rate of glucose conversion and selectivity towards methyl lactate. Furthermore, a higher Sn loading can enhance the reaction rate by providing more active sites for the desired reactions. Stability of Sn-modified H-Y zeolites can also be influenced by the Sn loading meaning that the catalyst may undergo some modifications already in the reaction phase when Sn loading is not within an optimum range[13]. Four different Sn and K modified catalysts were synthesized by the same procedure with different Sn loading. The yields of different products from glucose transformation are shown in **Table 13**. Even if dealumination is challenging very similar amounts of aluminium in the range of 0.43-0.46 wt.% were detected resulting in high methyl lactate yields apart from one catalyst.

Table 13: Influence of Sn loading on methyl lactate yield (Reaction conditions: liquid volume, 75 ml; glucose concentration, 12 g/l; 150 °C, 30 bar)

Sample	Al (wt.%)	Sn (wt.%)	MB (%)	ML (%)	M-Le (%)	MVG (%)	M-For (%)
K-Sn-H-Y-30-DA	0.45	0.87	98	**70**	1.8	6	2
K-Sn-H-Y-30-DA-2	0.46	3.61	97	**40**	4	4	1.8
K-Sn-H-Y-30-DA-3	0.43	1.43	98	**66**	<1	7	1
K-Sn-H-Y-30-DA-4	0.46	1.32	98	**72**	2	7	<1

Notation: MB: mass balance, ML: methyl lactate, M-Le: methyl levulinate, MVG: methyl-vinyl-glycolate, M-For: methyl formate (Catalysts preparation method was given in section 3.2.2).

The results from **Table 13** revealed that an optimized amount of Sn should be used. As a comparison, the catalyst with the highest amount of Sn (ca. 3.6 wt.%) gave much lower methyl lactate yield (40%).

Influence of reaction conditions

Reaction parameters such as temperature, pressure, solvent, catalyst-to-glucose ratio, and reaction time can influence the overall performance of the catalysts. Fine-tuning these conditions is essential to maximize the yield of methyl lactate. Even though such study requires a lot of experimental work[38] to reach to the best conditions, various catalyst-to-glucose ratios were studied in this work as a preliminary approach to optimization. **Table 14** combines the results on exploitation of the parameter space for the best performing catalyst. In all reactions, full conversion of glucose was detected already after 30 min of the reactions, giving ML yields ranging from 58 to 72%. The highest yield of 72 % ML was achieved using 0.75 g of the catalyst with the catalyst-to-glucose mass ratio of 0.83. Even though the yield was expected to be higher for higher catalyst amounts (1.16 mass ratio), it dropped to 62% as analogously to previously reported lactic acid formation from biomass[128].

Table 14: Effect of cat/glu mass ratio after 24 h reaction (Reaction conditions: liquid volume, 75 ml; 150 °C, 30 bar, complete conversion of sugars)

No	Catalyst	m_cat (g)	m_cat/m_gl	MB (%)	ML Yield %	M-Le (%)	MVG (%)	M-For (%)
1	0.8wt.% K – 2wt.% Sn/H-Y-30-DA	0.45	0.5	98	**58**	2	7	1
2		0.6	0.67	98	**65**	3	4	0.7
3		0.75	0.83	96	**72**	2	7	-
4		0.9	1	97	**67**	2.4	6	1
5		1.05	1.16	95	**62**	4	6	0.9

Notation: MB: mass balance, ML: methyl lactate, M-Le: methyl levulinate, MVG: methyl-vinyl-glycolate, M-For: methyl formate.

Increasing the catalyst amount can lead to a decrease in the yield of the product in certain reactions due to several factors[129–131]:

1) Mass transfer limitations: When the catalyst amount is increased excessively, it can lead to higher viscosity or hinder diffusion of the reactants and products within the reaction

mixture. This can result in a poor contact between the reactants and the active sites on the catalyst surface, leading to lower reaction rates and decreased yield.

2) Side reactions: In some cases, an increase in the catalyst amount can promote side reactions or undesired pathways, leading to formation of the by-products instead of the desired one. This can occur when the catalyst per se or the support promotes undesired reactions or when it interacts with other components in the reaction mixture to generating unwanted products.
3) Catalyst deactivation: Certain catalysts can undergo deactivation or degradation due to aggregation, sintering, or poisoning of active sites, leading to a decrease in catalytic activity and subsequently lower product yield.

Furthermore, the best catalyst which is 0.8 wt.% K – 2 wt.% Sn/H-Y-30-Da was also further analyzed to investigate metal leaching. The total amount of leached metals determined by ICP-MS method was found to be 15.5 wt.% and 6.4 wt.% for Sn and K, respectively.

In total, 41 reactions were performed in this work with the outcome summarized in **Figure 28**, illustrating yields of methyl lactate and methyl levulinate as the reaction products.

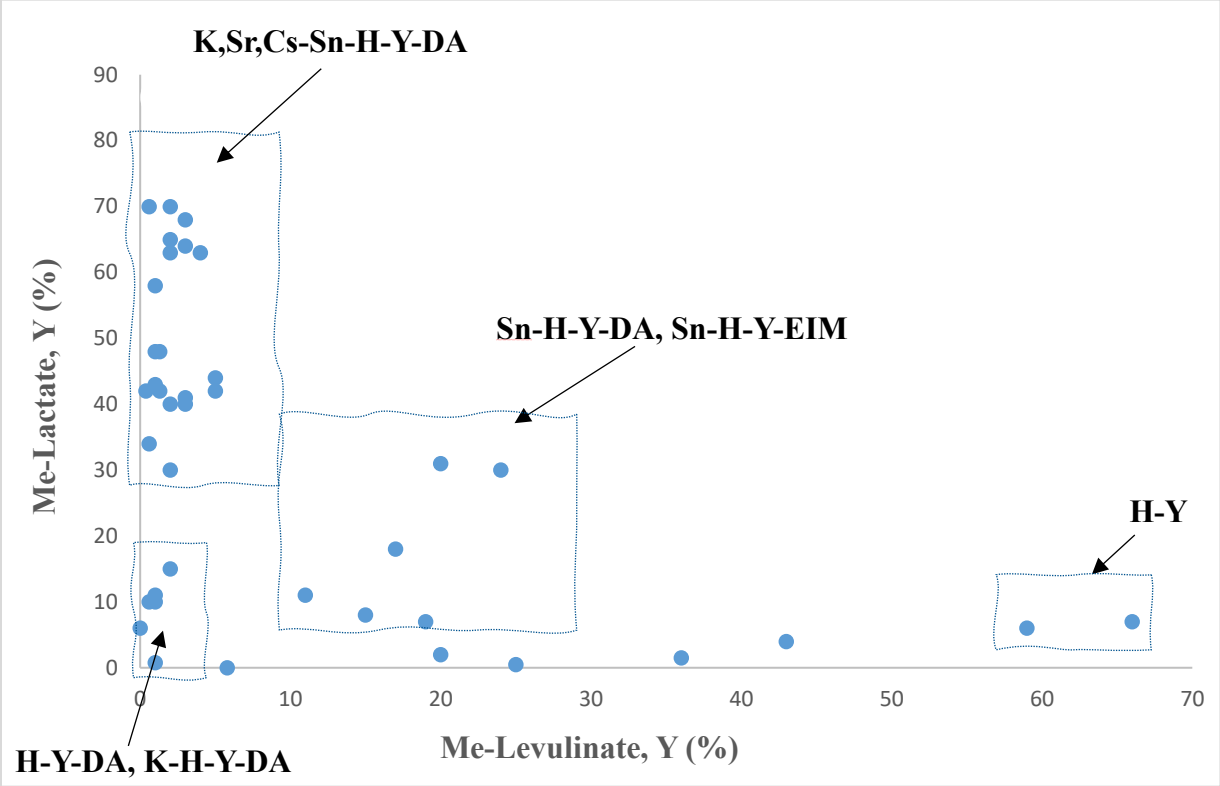

Figure 28: Combined reaction results as desirable (methyl lactate) versus undesirable (methyl levulinate) product yields

It can be concluded that Sn and alkali metal-modified catalysts, alongside Sr-modified dealuminated H-Y zeolites, demonstrated notably high methyl lactate yields ranging from 30% to 72%. Simultaneously, corresponding yields of methyl levulinate were relatively low. Conversely, monometallic Sn-modified dealuminated catalyst exhibited a reasonably favorable methyl lactate yield of up to 30%, while the impregnated zeolites demonstrated poor catalytic performance in this particular study. The significance of Sn as a catalytic phase in this reaction is evident when examining the results of the dealuminated and solely K-modified catalysts, which yielded very low average methyl lactate and methyl levulinate yields, both below 10%. Interestingly, the pristine H-Y zeolites demonstrated remarkably high methyl levulinate yields of approximately 60%, attributed to their high number of strong acid sites[116].

4.3. Challenges with product analysis

The reaction from glucose to methyl lactate using Sn and K modified H-Y zeolites presents several challenges in terms of the product analysis. These challenges arise from the complexity of the reaction system[13] and a need to quantify the desired product, methyl lactate, as well as many by-products and intermediates.

For one of the best performing catalysts of 0.8 wt.% K – 2 wt.%Sn/H-Y-30-DA mass spectrometry (MS) coupled with GC was used in addition to GC and HPLC. As can be seen from **Figure 29**, it was possible to identify most of the peaks for unknown by-products from GC-MS.

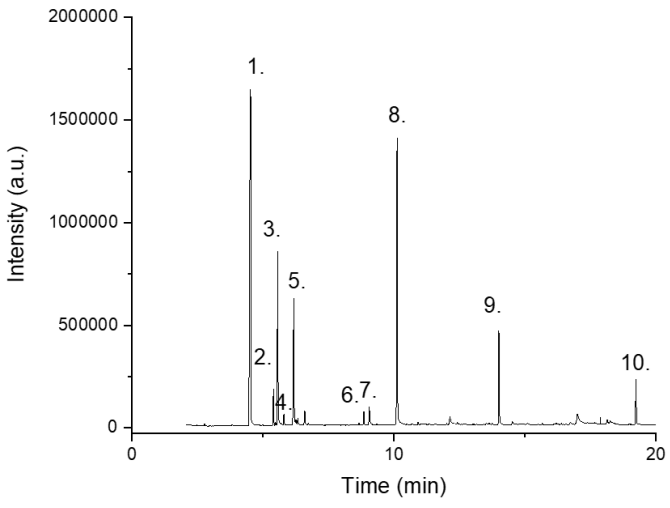

1.	Methyl Lactate
2.	3-methoxyphenylethanol
3.	1,1-dimethoxypropane
4.	1,1-dimethoxypropanol
5.	Ether (specifically unknown)
6.	4-oxo-5-methoxy-2-penten-5-olide
7.	Methyl-3-acethylpropanoate
8.	2-(2-methoxyethoxy)-ethanol
9.	Unknown
10.	Hexadecane (solvent for MS)
Some dimeric compounds at high retention times (>30 min)	

Figure 29: Identification of the products with GC-MS analysis; MS intensity signal and number of peaks (left), with identified chemicals table (right)

4.4. Hot filtration test

Hot filtration test was performed for the reaction with 2 wt.% Sr – 2 wt.% Sn/H-Y-30-DA as a catalyst. The results confirmed that the reaction proceeded after filtering away the solid catalyst after 1440 min and continuing the experiment with the filtrate (**Figure 30**) indicating homogeneous catalysts, i.e. by leached metals.

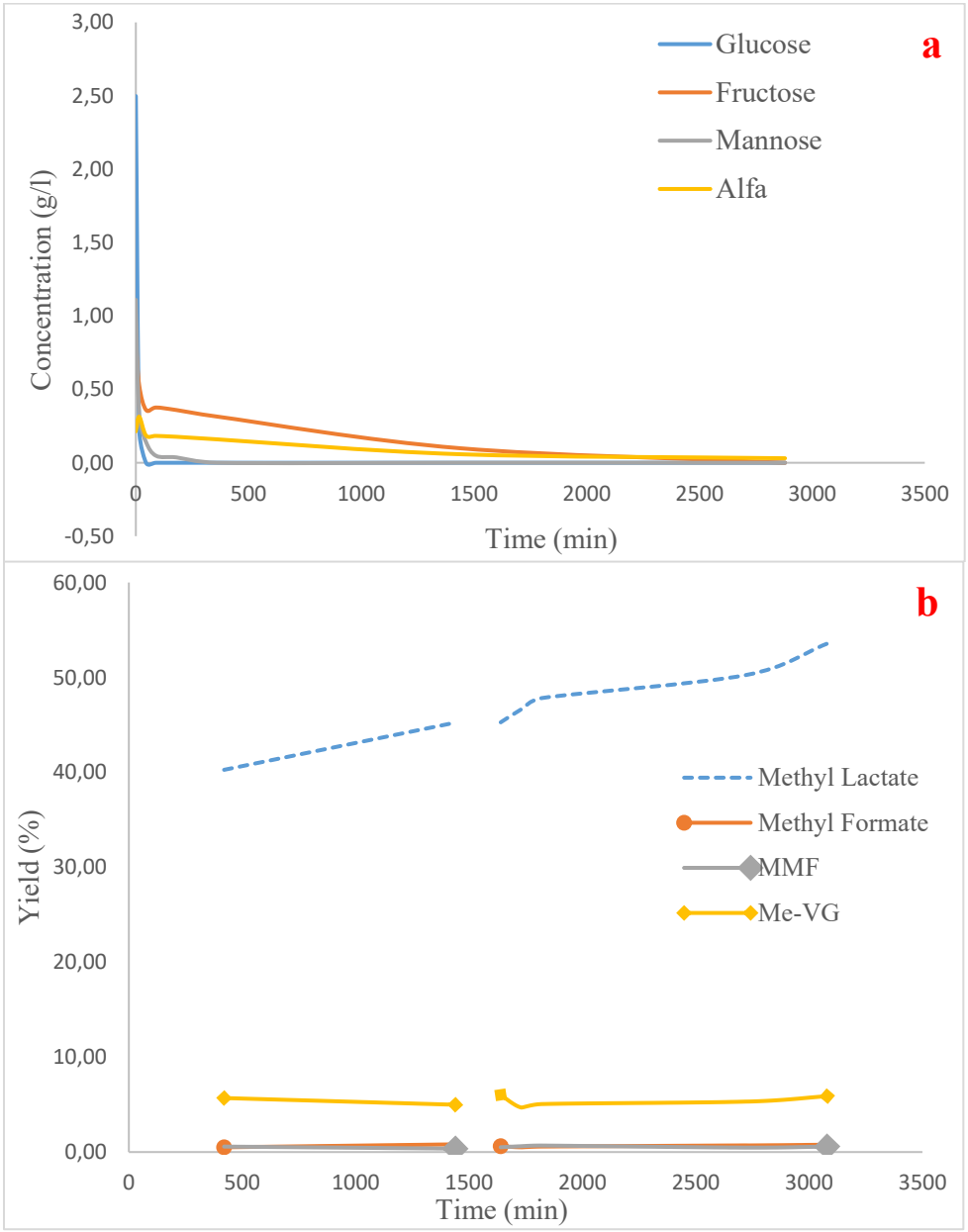

Figure 30: Sugar concentration curves (a) and reaction results (b) from the hot filtration test (Reaction conditions: liquid volume, 75 ml; glucose concentration, 12 g/l; 150 °C, 30 bar)

4.5. Reproducibility and repeatability

Reproducibility of catalysts performance plays a critical role in ensuring their reliability and applicability[132]. In this study, a particular attention was given to investigation of the reproducibility of the best-performing catalyst, which involved synthesis of the dealuminated H-Y zeolite with the SAR of 30. The aim was to determine if the catalyst's superior performance could be consistently replicated and if the obtained results were repeatable.

Regarding the best-performing catalyst, namely Sn and K-modified by ion-exchange H-Y-30 zeolite, it was synthesized multiple times to assess its reproducibility. The elemental composition of the catalysts was determined through ICP measurements, and the corresponding results are presented in **Table 13**. During the initial synthesis, the K-Sn-H-Y-30-DA catalyst exhibited exceptionally high reaction rates and yielded up to 70% methyl lactate, even once reaching the record-breaking 85% yield of methyl lactate under the same reaction conditions. However, when the catalyst was synthesized for the second time (K-Sn-H-Y-30-DA-2), with a modification in the amount of Sn loading as indicated in **Table 13**, its performance significantly deteriorated under the same reaction conditions (0.75 g catalyst loading, 9 g/l substrate concentration, 75 ml solvent, 150 °C, 30 bar, 24 h). Consequently, after the second synthesis, the yields of methyl lactate dropped to only 40%. This unexpected behaviour of the catalysts raised several questions since the previous literature reported reproducible results for synthesized H-Y zeolites, exhibiting high activity and stability[133].

Reproducibility of Sn and K-modified H-Y zeolites in the transformations of glucose to methyl lactate has been reported in several studies[133,134]. For example, robust synthesis of Sn and K-modified H-Y zeolites using a different method giving reproducible results by conducting multiple experiments was demonstrated. Findings of this study also demonstrated consistent catalytic performance in terms of conversion and selectivity, further highlighting reproducibility of the catalysts[134].

To comprehend the disparity in the synthesis process of two catalysts and specifically elucidate the impact of varying Sn loading amounts on catalyst performance, a series of experiments and characterizations were conducted. The ICP elemental weight compositions of these catalysts, as depicted in **Table 13**, provided crucial insights into the significance of appropriate Sn loading.

Additionally, ultraviolet-visible spectroscopy and solid-state NMR were employed to investigate the distinctions between the catalysts, with the corresponding results presented in **Figure 31**.

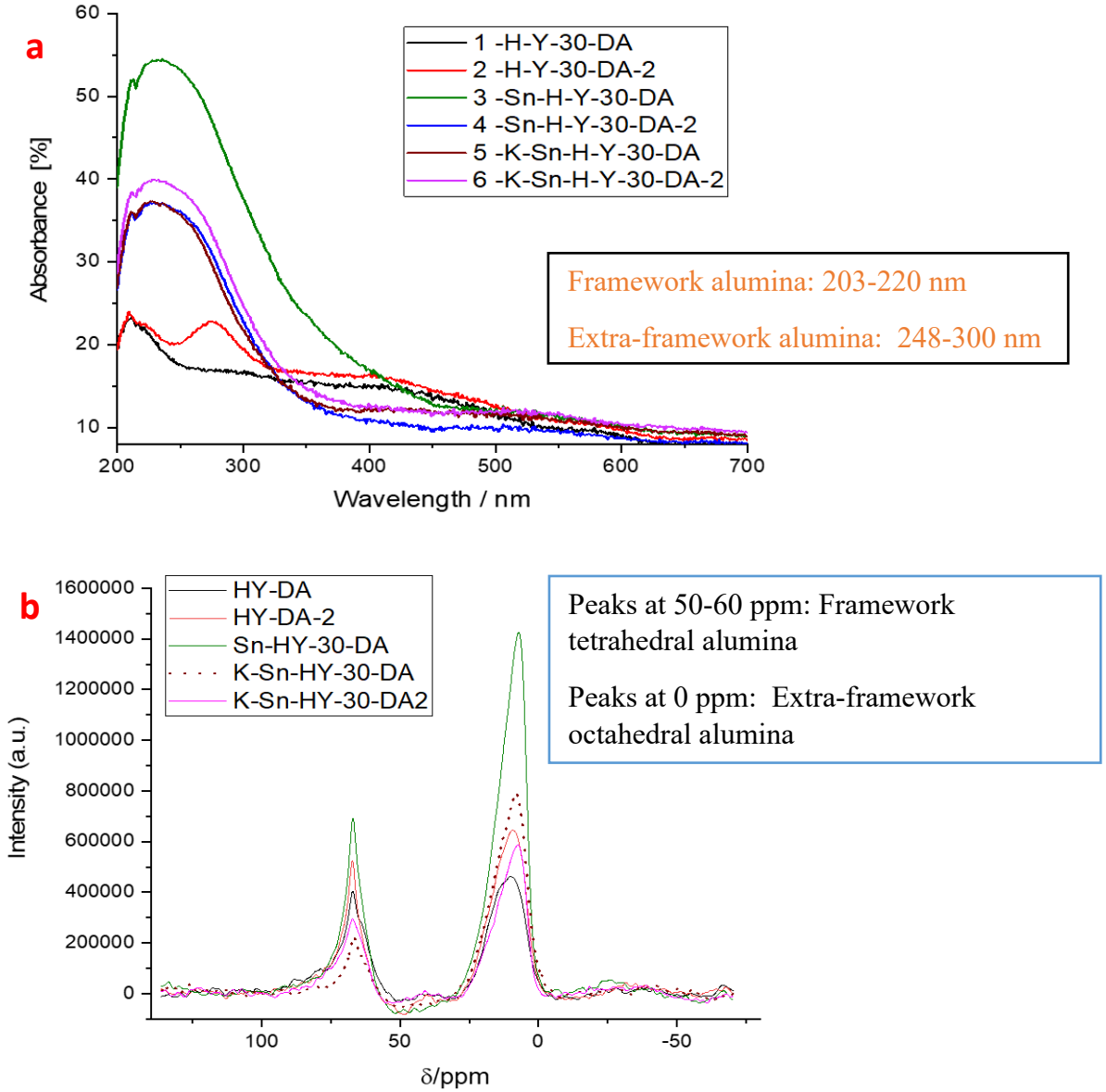

Figure 31: UV-vis (a) and solid-state NMR results (b) comparisons for understanding the reproducibility of the preparation of different catalyst

The UV-vis results unveiled substantial variations in the dealumination step during the synthesis of these catalysts. **Figure 31** demonstrates notable dissimilarities, particularly in the wavelength range of 248-300 nm[50], which indicates a significant presence of extra-framework alumina structures in the second synthesized catalyst (H-Y-30-DA-2) compared to the dealuminated H-Y-30-DA. Although both catalysts exhibited similar peaks for alumina in the framework structures

(203-220 nm)[135], the distinct UV-vis profiles underscored the contrasting nature of the dealumination process. Furthermore, disparities in the positioning of Sn atoms within the catalysts were observed, along with variations in the intensities of absorbances. Notably, both Sn-H-Y-30-DA and Sn-H-Y-30-DA-2 exhibited a prominent absorption band in the 210–220 nm region, indicative of isolated Sn^{IV} species with a tetrahedral coordination within their zeolite frameworks[50].

The results from solid-state NMR supported conclusions from the UV-vis study highlighting importance of the dealumination step. ^{27}Al MAS NMR has been established as an efficient method to determine the coordination and the local structure of specific aluminium species in zeolites since each ^{27}Al site can be readily resolved based on their distinctly different chemical shifts[136]. **Figure 31 b** reports ^{27}Al MAS NMR spectra of the dealuminated HY zeolites (H-Y-30-DA, and H-Y-30-DA-2). Obviously, the hydration process has a significant effect on the ^{27}Al MAS spectra. In general, three broad peaks at around 60, 30 and 0 ppm can be observed in the ^{27}Al MAS spectra of the hydrated samples. The 60 ppm signal originates from four-coordinated framework Al i.e. Brønsted acid sites, while the peak centered at around 30 ppm arises from the five-coordinated extra-framework Al, and the resonance at 0 ppm corresponding to Lewis acid sites is associated with six-coordinated extra-framework aluminium[136,137]. Both solid state NMR and UV-vis spectroscopy confirmed that dealumination of the H-Y zeolite is an essential step because removal of aluminium from the extra-framework structure should be achieved successfully. Otherwise the yield of methyl lactates will decrease at the expense of other undesirable products[138].

In summary, a comprehensive analysis of the synthesis process and characterization of the catalysts provided valuable insights into the influence of Sn loading and the resulting disparities in catalyst performance. The UV-vis spectroscopy and solid-state NMR techniques effectively highlighted the differences in dealumination, extra-framework structures, Sn positioning, and absorbance intensities, emphasizing the distinct nature of the catalysts. These findings contribute to a better understanding of the underlying mechanisms and facilitate further optimization of the catalyst synthesis for improved and reliable performance of the catalysts.

Despite the encountered challenges during the catalyst synthesis, the majority of the obtained results could be reproduced. Underlying chemistry behind catalyst synthesis led to subsequent synthesis of the optimal catalysts, labelled as K-Sn-H-Y-30-DA-3 and K-Sn-H-Y-30-DA-4 (**Table 13**). The loading of K, Sn, and Al in these catalysts was found to be quite similar. Concentration

curves of fructose derived from two separate reactions using the K-Sn-H-Y-30-DA-4 catalyst are provided. **Figure 32** illustrates that the fructose concentration changes in a comparable manner with a minimal discrepancy. The initial concentration increase can be attributed to the isomerization of glucose to fructose, involving carbonyl group rearrangement, as outlined in the reaction mechanism (**Figure 3**)[13]. Subsequently, fructose itself undergoes decomposition and further transformation reactions, yielding various intermediate products that eventually lead to formation of methyl lactate.

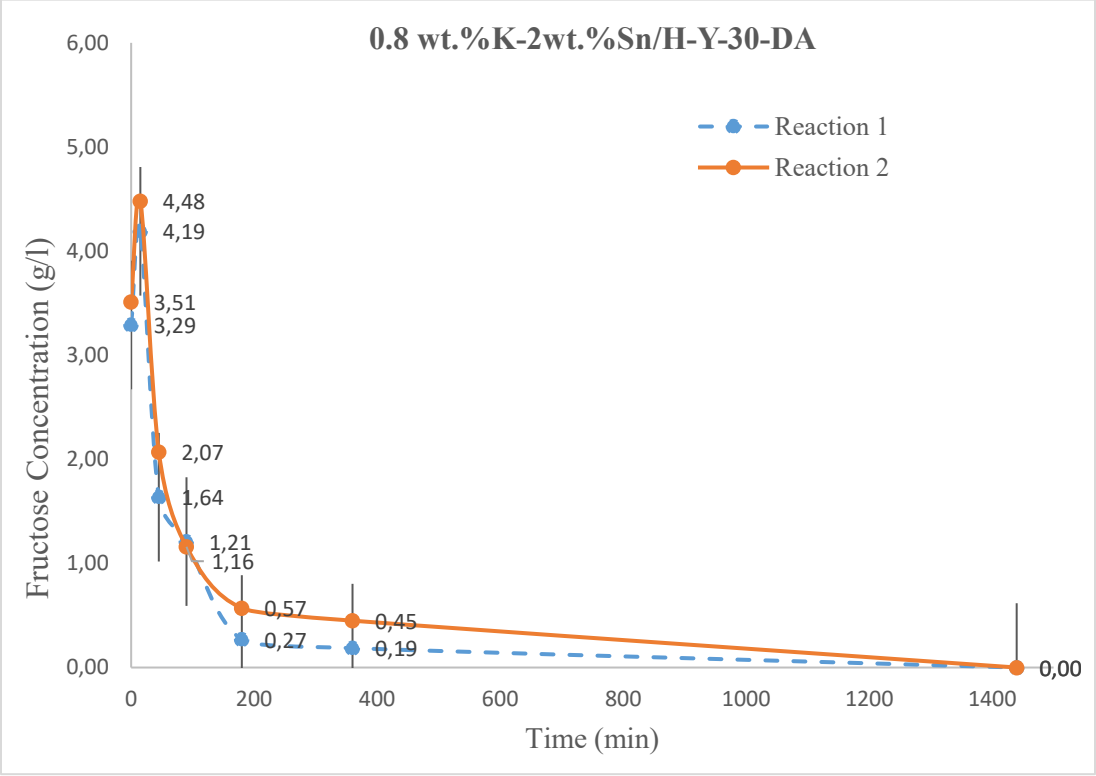

Figure 32: Repeatability of the glucose transformation over K-Sn-H-Y-30-DA catalyst based on fructose concentration curves (Reaction conditions: liquid volume, 75 ml; glucose concentration, 12 g/l; 150 °C, 30 bar)

4.6. Catalyst regeneration and reuse

Catalyst regeneration was performed for K-Sn-H-Y-30-DA-4 the best catalyst studied in this work in terms of methyl lactate yield. The findings revealed that although complete glucose conversion was achieved within just 30 minutes, the overall yield of methyl lactate decreased to 33%, whereas the fresh catalyst exhibited a methyl lactate yield of 72% under identical reaction conditions, as

indicated in **Table 15**. Intriguingly, a substantial rise in the yields of methyl levulinate was observed, suggesting a decline in catalyst selectivity favouring the production of methyl levulinate.

Table 15: Reaction results for the fresh (1) and regenerated (2) K-Sn-H-Y-30-DA-4 catalyst (Reaction conditions: 0.75 g catalyst loading, 9 g/l substrate concentration, 75 ml solvent, 150 °C, 30 bar)

Reactions	Me-lactate (%)	Me-levulinate (%)	MVG (%)	Me-formate (%)
1	72	2	7	<1
2	33	21	4	3

Notation: MVG stands for methyl-vinyl-glycolate.

Differences in the product distribution are visualized in **Figure 33**, where the chromatograms are presented for the fresh and the regenerated catalysts.

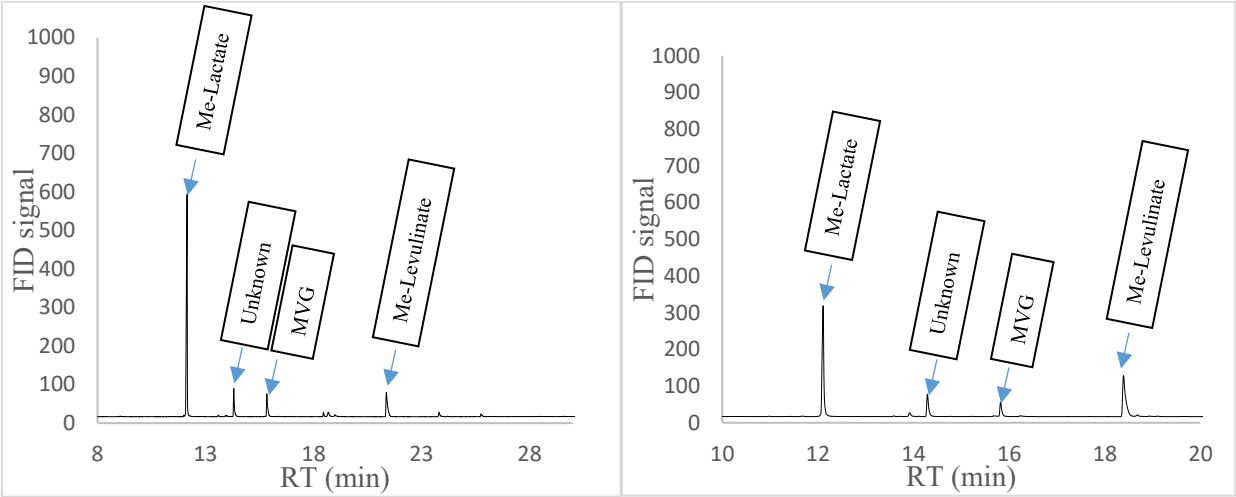

Figure 33: GC product identification for the fresh (left) and the regenerated (right) K-Sn-H-Y-30-DA catalyst

Overall, the regeneration and reuse of K and Sn modified H-Y zeolite catalysts have shown that there is a need for further research and analysis as there can be many reasons for different behaviour of regenerated catalysts[139]. In any case, coking can be concluded as a reason for catalyst deactivation according to HRTEM in addition to sintering[140].

4.7. Coke analysis

TGA provided valuable information about the amount of coke formed and its thermal stability for the best catalyst (K-Sn-H-Y-30-DA). Presence of carbonaceous species on the catalyst surface suggested occurrence of coking. The amount of coke was quantified by measuring the weight loss in the TGA experiments to be 4.6 wt.% as shown in **Figure 34**.

The CHNS analysis revealed that the coke generated on K-Sn-H-Y-30-DA catalyst exhibited a hydrogen-to-carbon (H/C) molar ratio of 2.6. Comparison of this finding with existing literature established that the coke's composition predominantly comprised alkanes, consistent with an H/C ratio exceeding 2[141].

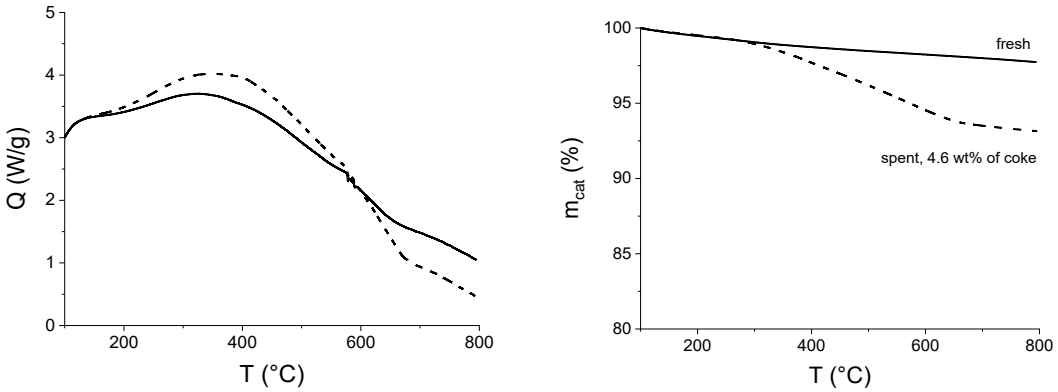

Figure 34: Thermal stability of coke formed (left) and its amount (right) for K-Sn-H-Y-30-DA

5. Conclusions

In this work, the synthesis, characterization, and testing of H-Y zeolites for the production of methyl lactate from glucose have been investigated. The main objective was to explore the influence of Sn, K and other metal modifications on the catalytic performance and selectivity towards methyl lactate formation.

Different methods were employed to introduce Sn and K species into the H-Y zeolite framework. The characterization techniques, such as X-ray diffraction (XRD), scanning electron microscopy (SEM), Fourier-transform infrared spectroscopy (FTIR) and nitrogen physisorption provided valuable insights into the structural and morphological properties of the catalysts.

The catalyst testing phase involved transformations of glucose to methyl lactate under various reaction conditions. The highest methyl lactate yield was 85 % obtained in glucose transformation at 150 °C in methanol as a solvent over K-Sn-H-Y-30-DA catalyst with the initial glucose concentration of 9 g/l. This catalyst exhibited no strong Lewis acid sites with highly mesoporous (40%) structure enhancing formation of methyl lactate. TGA coke analysis revealed formation of 4.6 wt.% coke after the 24 h reaction. CHNS analysis conducted on the spent K-Sn-H-Y-30-DA catalyst revealed the predominance of paraffins as the primary constituent of the formed coke.

The results revealed that the presence of Sn species played a crucial role in promoting the cleavage of the C-C bond in glucose[142], facilitating formation of intermediates and the desired product. Additionally, K modification enhanced accessibility of the reactants to the active sites due to creation of more mesopores with decrease in Lewis/Brønsted total acid sides, leading to an overall improvement in the reaction rate. However, it was observed that excessive Sn loading could result in catalyst deactivation or formation of the undesired by-products. Similarly, increasing the catalyst-to-glucose ratio beyond a certain point led to a decrease in the yield of methyl lactate. These findings highlight the importance of carefully optimizing the catalyst loading and reaction conditions to achieve the desired selectivity and the yield.

Overall, the production of methyl lactate from glucose over H-Y zeolites represents a promising avenue for the utilization of renewable resources and the development of sustainable chemical processes. Continued research and development in this field will contribute to the advancement of green chemistry and the transition toward a more environmentally friendly and resource-efficient chemical industry.

1. References:

(1) Murzin, D. Yu. Mesolevel Bifunctional Catalysis. Kinet. Catal. 2020, 61 (1), 80–92. https://doi.org/10.1134/S0023158420010073.

(2) Mäki-Arvela, P.; Simakova, I.; Salmi, T.; Murzin, D. Production of Lactic Acid/Lactates from Biomass and Their Catalytic Transformations to Commodities. Chem. Rev. 2013, 114. https://doi.org/10.1021/cr400203v.

(3) Corma, A.; Nemeth, L. T.; Renz, M.; Valencia, S. Sn-Zeolite Beta as a Heterogeneous Chemoselective Catalyst for Baeyer-Villiger Oxidations. Nature 2001, 412 (6845), 423–425. https://doi.org/10.1038/35086546.

(4) Mäki-Arvela, P.; Simakova, I. L.; Salmi, T.; Murzin, D. Y. Production of lactic acid/lactates from biomass and their catalytic transformations to commodities. Chem. Rev. 2014, 114(3), 1909-1971.

(5) Milovanovic, S.; Pajnik, J., Lukic, I. Tailoring of advanced poly (lactic acid)-based materials: A review. J. Appl. Polym. Sci. 2022, 139, 12, 51839.

(6) Bressanin, J. M., de Mesquita Sampaio, I. L., Geraldo, V. C., Klein, B. C., Chagas, M. F., Bonomi, A., Filho, R. M., Cavalett, O. Techno-economic and environmental assessment of polylactic acid production integrated with the sugarcane value chain. Sustainable Production and Consumption 2022, 34, 244-256.

(7) Tosi, I.; Sacchetti, A.; Martinez-Espin, J. S.; Meier, S.; Riisager, A. Exploring the Synthesis of Mesoporous Stannosilicates as Catalysts for the Conversion of Mono- and Oligosaccharidesinto Methyl Lactate. Top. Catal. 2019, 62 (7–11), 628–638. https://doi.org/10.1007/s11244-019-01135-8.

(8) Theng, D.; Du, Y.; Xi, S.; Huang, L.; Gao, F.; Wang, C.; Chen, L.; Borgna, A. Selective Conversion of Lactic Acid to Acrylic Acid over Alkali and Alkaline-Earth Metal Co-Modified NaY Zeolites. Catal. Sci. Technol. 2017, 7. https://doi.org/10.1039/C7CY02142A.

(9) Tang, B.; Li, S.; Song, W.-C.; Yang, E.-C.; Zhao, X.-J.; Guan, N.; Li, L. Fabrication of Hierarchical Sn-Beta Zeolite as Efficient Catalyst for Conversion of Cellulosic Sugar to Methyl Lactate. ACS Sustain. Chem. Eng. 2020, 8 (9), 3796–3808. https://doi.org/10.1021/acssuschemeng.9b07061.

(10) Liu, X.; Yang, W.; Zhang, Q.; Li, C.; Wu, H. Current Approaches to Alkyl Levulinates via Efficient Valorization of Biomass Derivatives. Front. Chem. 2020, 8.

(11) Jimenez-Martin, J. M., Orozco-Saumell, A., Hernando, H., Linares, M., Mariscal, R., López Granados, M., Garcia, A., Iglesias, J. Efficient Conversion of Glucose to Methyl Lactate with Sn-USY: Retro-aldol Activity Promotion by Controlled Ion Exchange. ACS Sust. Chem. & Eng. 2022, 10(27), 8885-8896.

(12) Zhou, S.; Yang, X.; Zhang, Y., Jiang, L., Zhou, L., Lu, T., Su., Y. Efficient conversion of cellulose to methyl levulinate over heteropoly acid promoted by Sn-Beta zeolite. Cellulose 2019, 26, 9135–9147. https://doi.org/10.1007/s10570-019-02743-z

(13) Aho, A.; Kumar, N.; Eränen, K.; Lassfolk, R.; Mäki-Arvela, P.; Salmi, T.; Peurla, M., Angervo, I., Hietala, J., Murzin, D. Y. Improving the methyl lactate yield from glucose over Sn–Al-Beta zeolite by catalyst promoters. Micropor. Mesop. Mat. 2023, 351, 112483.

(14) Jimenez-Martin, J. M.; Orozco-Saumell, A.; Hernando, H.; Linares, M.; Mariscal, R.; López Granados, M.; Garcia, A.; Iglesias, J. Efficient Conversion of Glucose to Methyl Lactate with Sn-USY: Retro-aldol Activity Promotion by Controlled Ion Exchange. ACS Sust. Chem. Eng. 2022, 10(27), 8885-8896.

(16) van der Graaff, W. N. P.; Tempelman, C. H.; A. Pidko, E.; M. Hensen, E. J. Influence of Pore Topology on Synthesis and Reactivity of Sn-Modified Zeolite Catalysts for Carbohydrate Conversions. Catal. Sci. Technol. 2017, 7 (14), 3151–3162. https://doi.org/10.1039/C7CY01052D.

(17) Sun, Y.; Shi, L.; Wang, H.; Miao, G.; Kong, L.; Li, S.; Sun, Y. Efficient Production of Lactic Acid from Sugars over Sn-Beta Zeolite in Water: Catalytic Performance and Mechanistic Insights. Sustain. Energy Fuels 2019, 3 (5), 1163–1171. https://doi.org/10.1039/C9SE00020H.

(18) Yang, X.; Lv, B.; Lu, T.; Su, Y.; Zhou, L. Promotion Effect of Mg on a Post-Synthesized Sn-Beta Zeolite for the Conversion of Glucose to Methyl Lactate. Catal. Sci. Technol. 2020, 10 (3), 700–709. https://doi.org/10.1039/C9CY02376C.

(19) Dong, W., Shen, Z., Peng, B. et al. Selective Chemical Conversion of Sugars in Aqueous Solutions without Alkali to Lactic Acid Over a Zn-Sn-Beta Lewis Acid-Base Catalyst. Sci. Rep. 6, 26713 (2016). https://doi.org/10.1038/srep26713.

(20) Yang, L.; Yang, X.; Tian, E.; Vattipalli, V.; Fan, W.; Lin, H. Mechanistic Insights into the Production of Methyl Lactate by Catalytic Conversion of Carbohydrates on Mesoporous Zr-SBA-15. J. Catal. 2016, 333, 207–216. https://doi.org/10.1016/j.jcat.2015.10.013.

(21) Sho Yamaguchi, Mizuho Yabushita, Minjune Kim, Jun Hirayama, Ken Motokura, Atsushi Fukuoka, and Kiyotaka Nakajima ACS Sust. Chem. Eng. 2018 6 (7), 8113-8117 DOI: 10.1021/acssuschemeng.8b00809.

(22) Wang, F.; Wen, Y.; Fang, Y.; Ji, H. Synergistic Production of Methyl Lactate from Carbohydrates Using an Ionic Liquid Functionalized Sn-Containing Catalyst. ChemCatChem 2018, 10(18), 4154-4161.

(23) Zhao, X.; Wen, T.; Zhang, J.; Ye, J.; Ma, Z.; Yuan, H.; Ye, X.; Wang, Y. Fe-Doped SnO 2 Catalysts with Both BA and LA Sites: Facile Preparation and Biomass Carbohydrates Conversion to Methyl Lactate MLA. RSC Adv. 2017, 7 (35), 21678–21685. https://doi.org/10.1039/C7RA01655G.

(24) Lu, X.; Wang, L.; Lu, X. Catalytic Conversion of Sugars to Methyl Lactate over Mg-MOF-74 in near-Critical Methanol Solutions. Catal. Commun. 2018, 110, 23–27. https://doi.org/10.1016/j.catcom.2018.02.027.

(25) Xiao, Y.; Xu, S.; Zhang, W.; Li, J.; Hu, C. One-Pot Chemo-Catalytic Conversion of Glucose to Methyl Lactate over In/γ-Al2O3 Catalyst. Catal. Today 2021, 365, 249–256. https://doi.org/10.1016/j.cattod.2020.02.038.

(26) Lyu, X.; Wang, L.; Chen, X.; Xu, L.; Wang, J;, Deng, S.;, Lu, X. Enhancement of catalytic activity by γ-NiOOH for the production of methyl lactate from sugars in near-critical methanol solutions. Ind. Eng. Chem. Res. 2019, 58(9), 3659-3665.

(27) Murillo, B.; de la Iglesia, Ó.; Rubio, C.; Coronas, J.; Téllez, C. Conversion of Sugars to Methyl Lactate with Exfoliated Layered Stannosilicate UZAR-S4. Catal. Today 2021, 362, 90–96. https://doi.org/10.1016/j.cattod.2020.03.064.

(28) Vajglová, Z.; Kumar, N.; Mäki-Arvela, P.; Eränen, K.; Peurla, M.; Hupa, L.; Nurmi, M.; Toivakka, M.; Murzin, D. Y. Synthesis and Physicochemical Characterization of Shaped Catalysts of β and Y Zeolites for Cyclization of Citronellal. Ind. Eng. Chem. Res. 2019, 58 (39), 18084–18096. https://doi.org/10.1021/acs.iecr.9b02829.

(29) Yuan, C.; Huayan, L.; Zhang, Z.; Lu, H.-F.; Zhu, Q.; Chen, Y. Alkali-Metal-Modified ZSM-5 Zeolites for Improvement of Catalytic Dehydration of Lactic Acid to Acrylic Acid. Chin. J. Catal. 2015, 36, 1861–1866. https://doi.org/10.1016/S1872-2067(15)60970-6.

(30) Trinh, B. M.; Ogunsona, E. O.; Mekonnen, T. H. Thin-Structured and Compostable Wood Fiber-Polymer Biocomposites: Fabrication and Performance Evaluation. Compos. Part Appl. Sci. Manuf. 2021, 140, 106150. https://doi.org/10.1016/j.compositesa.2020.106150.
(31) Aho, A.; Engblom, S.; Eränen, K.; Russo, V.; Mäki-Arvela, P.; Kumar, N.; Wärnå, J.; Salmi, T.; Murzin, D. Y. Glucose Transformations over a Mechanical Mixture of ZnO and Ru/C Catalysts: Product Distribution, Thermodynamics and Kinetics. Chem. Eng. J. 2021, 405 (126945). https://doi.org/10.1016/j.cej.2020.126945.
(32) Chatterjee, S.; Venkata Mohan, S. Refining of Vegetable Waste to Renewable Sugars for Ethanol Production: Depolymerization Andfermentation Optimization. Bioresour. Technol. 2021, 340, 125650. https://doi.org/10.1016/j.biortech.2021.125650.
(33) Ott, J.; Gronemann, V.; Pontzen, F.; Fiedler, E.; Grossmann, G.; Kersebohm, D. B.; Weiss, G.; Witte, C. Methanol. In Ullmann's Encyclopedia of Industrial Chemistry; Wiley, 2012. https://doi.org/10.1002/14356007.a16_465.pub3.
(34) Eta, V.; Mäki-Arvela, P.; Salminen, E.; Salmi, T.; Murzin, D. Y.; Mikkola, J. P. The Effect of Alkoxide Ionic Liquids on the Synthesis of Dimethyl Carbonate from CO_2 and Methanol over ZrO_2–MgO. Catal Lett. 2011, 141, 1254–1261. https://doi.org/10.1007/s10562-011-0666-3.
(35) Askari, M. B.; Beheshti-Marnani, A.; Seifi, M.; Rozati, S. M.; Salarizadeh, P. Fe3O4@MoS2/RGO as an Effective Nano-Electrocatalyst toward Electrochemical Hydrogen Evolution Reaction and Methanol Oxidation in Two Settings for Fuel Cell Application. J. Colloid Interface Sci. 2019, 537, 186–196. https://doi.org/10.1016/j.jcis.2018.11.019.
(36) Kohli, K.; Prajapati, R.; Sharma, B. K. Bio-Based Chemicals from Renewable Biomass for Integrated Biorefineries. Energies 2019, 12 (2), 233. https://doi.org/10.3390/en12020233.
(37) Jiang, Y.; Lyu, X.; Chen, H.; Wei, X.; Zhang, Z.; Lu, X. Catalytic Conversion of High Fructose Corn Syrup to Methyl Lactate with CoO@silicalite-1. Catalysts 2022, 12 (4), 442. https://doi.org/10.3390/catal12040442.
(38) Mäki-Arvela, P.; Aho, A.; Murzin, D. Yu. Heterogeneous Catalytic Synthesis of Methyl Lactate and Lactic Acid from Sugars and Their Derivatives. ChemSusChem 2020, 13 (18), 4833–4855. https://doi.org/10.1002/cssc.202001223.
(39) Holm, M. S.; Saravanamurugan, S.; Taarning, E. Conversion of Sugars to Lactic Acid Derivatives Using Heterogeneous Zeotype Catalysts. Science 2010, 328 (5978), 602–605. https://doi.org/10.1126/science.1183990.
(40) Murzin, D. Y. Engineering Catalysis. In Engineering Catalysis; De Gruyter, 2020. https://doi.org/10.1515/9783110614435.
(41) Catalysis. Wikipedia; 2023.
(42) Cheng, X.; Lei, A.; Mei, T.-S.; Xu, H.-C.; Xu, K.; Zeng, C. Recent Applications of Homogeneous Catalysis in Electrochemical Organic Synthesis. CCS Chem. 2022, 4 (4), 1120–1152. https://doi.org/10.31635/ccschem.021.202101451.
(43) Li, B.; Wang, T.; Le, Q.; Qin, R.; Zhang, Y.; Zeng, H. C. Surface Reconstruction, Modification and Functionalization of Natural Diatomites for Miniaturization of Shaped Heterogeneous Catalysts. Nano Mater. Sci. 2022. https://doi.org/10.1016/j.nanoms.2022.05.001.
(44) Zeolites - BZA. http://www.bza.org/zeolites/ (accessed 2023-05-20).
(45) Baerlocher, C.; McCusker, L. B.; Olson, D. H. Atlas of Zeolite Framework Types; Elsevier, 2007.

(46) Chen, L.-H.; Sun, M.-H;, Wang, Z.; Yang, W.; Xie, X.; Su, B.-L. Chem. Rev. 2020, 120 (20), 11194-11294 DOI: 10.1021/acs.chemrev.0c00016.
(47) Villa, C.; Ayala Valencia, G.; López-Córdoba, A.; Ortega-Toro, R.; Ahmed, S.; Gutiérrez, T. Zeolites for Food Applications: A Review. Food Biosci. 2022, 46, 101577. https://doi.org/10.1016/j.fbio.2022.101577.
(48) Mäki-Arvela, P.; Kumar, N.; Nieminen, V.; Sjöholm, R.; Salmi, T.; Murzin, D. Yu. Cyclization of Citronellal over Zeolites and Mesoporous Materials for Production of Isopulegol. J. Catal. 2004, 225 (1), 155–169. https://doi.org/10.1016/j.jcat.2004.03.043.
(49) Cui, W.; Zhu, D.; Tan, J.; Chen, N.; Fan, D.; Wang, J.; Han, J.; Wang, L.; Tian, P.; Liu, Z. Synthesis of Mesoporous High-Silica Zeolite Y and Their Catalytic Cracking Performance. Chin. J. Catal. 2022, 43, 1945–1954. https://doi.org/10.1016/S1872-2067(21)64043-3.
(50) Jin, J.; Ye, X.; Li, Y.; Wang, Y.; Li, L.; Gu, J.; Zhao, W.; Shi, J. Synthesis of Mesoporous Beta and Sn-Beta Zeolites and Their Catalytic Performances. Dalton Trans. 2014, 43 (22), 8196–8204. https://doi.org/10.1039/C4DT00567H.
(51) Li, G.; Pidko, E. A.; Hensen, E. J. M. Synergy between Lewis Acid Sites and Hydroxyl Groups for the Isomerization of Glucose to Fructose over Sn-Containing Zeolites: A Theoretical Perspective. Catal. Sci. Technol. 2014, 4 (8), 2241–2250. https://doi.org/10.1039/C4CY00186A.
(52) Kusema, B. T.; Faba, L.; Kumar, N.; Mäki-Arvela, P.; Díaz, E.; Ordóñez, S.; Salmi, T.; Murzin, D. Yu. Hydrolytic Hydrogenation of Hemicellulose over Metal Modified Mesoporous Catalyst. Catal. Today 2012, 196 (1), 26–33. https://doi.org/10.1016/j.cattod.2012.02.031.
(53) Hendriks, F. C.; Valencia, D.; A. Bruijnincx, P. C.; M. Weckhuysen, B. Zeolite Molecular Accessibility and Host–Guest Interactions Studied by Adsorption of Organic Probes of Tunable Size. Phys. Chem. Chem. Phys. 2017, 19 (3), 1857–1867. https://doi.org/10.1039/C6CP07572J.
(54) Dapsens, P. Y.; Mondelli, C.; Jagielski, J.; Hauert, R.; Pérez-Ramírez, J. Hierarchical Sn-MFI Zeolites Prepared by Facile Top-down Methods for Sugar Isomerisation. Catal. Sci. Technol. 2014, 4 (8), 2302–2311. https://doi.org/10.1039/C4CY00172A.
(55) Cho, H. J.; Dornath, P.; Fan, W. Synthesis of Hierarchical Sn-MFI as Lewis Acid Catalysts for Isomerization of Cellulosic Sugars. ACS Catal. 2014, 4 (6), 2029–2037. https://doi.org/10.1021/cs500295u.
(56) Taarning, E.; Saravanamurugan, S.; Spangsberg Holm, M.; Xiong, J.; West, R. M.; Christensen, C. H. Zeolite-Catalyzed Isomerization of Triose Sugars. ChemSusChem 2009, 2 (7), 625–627. https://doi.org/10.1002/cssc.200900099.
(57) Graauw, C. F. de; Peters, J. A.; Bekkum, H. van; Huskens, J. Meerwein-Ponndorf-Verley Reductions and Oppenauer Oxidations: An Integrated Approach. Synthesis 1994, 1994 (10), 1007–1017. https://doi.org/10.1055/s-1994-25625.
(58) Wang, L.; Liu, Y.; Xie, W., Wu, H.; Li, X.; He, M.; Wu, P., J. Phys. Chem. C 2008 112 (15), 6132-6138 DOI: 10.1021/jp712155k
(59) Guo, Q.; Ren, L.; M. Alhassan, S.; Tsapatsis, M. Glucose Isomerization in Dioxane/Water with Sn-β Catalyst: Improved Catalyst Stability and Use for HMF Production. Chem. Commun. 2019, 55 (99), 14942–14945. https://doi.org/10.1039/C9CC07842H.
(60) Perego, C.; Villa, P. Catalyst Preparation Methods. Catal. Today 1997, 34 (3), 281–305. https://doi.org/10.1016/S0920-5861(96)00055-7.

(61) Wu, K. J.; Edmund, C. M.; Shang, C.; Guo, Z. Nucleation and growth in solution synthesis of nanostructures–from fundamentals to advanced applications. Progress in Materials Science 2022, 123, 100821.
(62) Stockmayer, W. H. Theory of Molecular Size Distribution and Gel Formation in Branched-Chain Polymers. J. Chem. Phys. 2004, 11 (2), 45–55. https://doi.org/10.1063/1.1723803.
(63) Shumilov, V.; Kirilin, A.; Tokarev, A.; Boden, S.; Schubert, M.; Hampel, U.; Hupa, L.; Salmi, T.; Murzin, D. Yu. Preparation of γ-Al2O3/α-Al2O3 Ceramic Foams as Catalyst Carriers via the Replica Technique. Catal. Today 2022, 383, 64–73. https://doi.org/10.1016/j.cattod.2020.09.019.
(64) Kumar, N.; Leino, E.; Mäki-Arvela, P.; Aho, A.; Käldström, M.; Tuominen, M.; Laukkanen, P.; Eränen, K.; Mikkola, J.-P.; Salmi, T.; Murzin, D. Yu. Synthesis and Characterization of Solid Base Mesoporous and Microporous Catalysts: Influence of the Support, Structure and Type of Base Metal. Microporous Mesoporous Mater. 2012, 152, 71–77. https://doi.org/10.1016/j.micromeso.2011.12.004.
(65) Shcherban, N. D.; Filonenko, S. M.; Yaremov, P. S.; Sergiienko, S. A.; Ilyin, V. G.; Murzin, D. Yu. Carbothermal Synthesis of Porous Silicon Carbide Using Mesoporous Silicas. J. Mater. Sci. 2017, 52 (7), 3917–3926. https://doi.org/10.1007/s10853-016-0652-7.
(66) Tsao, K. C.; Yang, H. Oxygen Reduction Catalysts on Nanoparticle Electrodes. In Encyclopedia of Interfacial Chemistry; Elsevier, 2018; pp. 796–811. https://doi.org/10.1016/B978-0-12-409547-2.13334-7.
(67) Zolotoyabko, E. Basic Concepts of X-Ray Diffraction; John Wiley & Sons, 2014, pp.312.
(68) Kholkina, E.; Kumar, N.; Eränen, K.; Peurla, M.; Palonen, H.; Salonen, J.; Lehtonen, J.; Murzin, D. Yu. Ultrasound Irradiation as an Effective Tool in Synthesis of the Slag-Based Catalysts for Carboxymethylation. Ultrason. Sonochem. 2021, 73, 105503. https://doi.org/10.1016/j.ultsonch.2021.105503.
(69) Ul-Hamid, A. A beginners' guide to scanning electron microscopy. Cham, Switzerland: Springer International Publishing. 2018, 1, 402.
(70) Zhou, W.; Apkarian, R. P.; Wang, Z. L.; Joy, D. Fundamentals of Scanning Electron Microscopy. Scanning Microscopy for Nanotechnology: Techniques and Applications, 2007, 1-40.
(71) Shindo, D.; Oikawa, T. Energy Dispersive X-Ray Spectroscopy. In Analytical Electron Microscopy for Materials Science; Shindo, D., Oikawa, T. Eds.; Springer Japan: Tokyo, 2002; pp 81–102. https://doi.org/10.1007/978-4-431-66988-3_4.
(72) Fourier-Transform Infrared Spectroscopy. Wikipedia; 2023.
(73) Thommes, M.; Cychosz, K. A. Physical Adsorption Characterization of Nanoporous Materials: Progress and Challenges. Adsorption 2014, 20 (2), 233–250. https://doi.org/10.1007/s10450-014-9606-z.
(74) Thommes, M.; Kaneko, K.; Neimark, A.; Olivier, J.; Rodriguez-Reinoso, F.; Rouquerol, J.; Sing, K. Physisorption of gases, with special reference to the evaluation of surface area and pore size distribution (IUPAC Technical Report). Pure Appl. Chem. 2015, 87(9-10), 1051-1069. https://doi.org/10.1515/pac-2014-1117.
(75) Bertier, P.; Schweinar, K.; Stanjek, H.; Ghanizadeh, A.; Clarkson, C. R.; Busch, A.; Kampman, N.; Prinz, D.; Amann-Hildebrand, A.; Krooss, B. M.; Pipich, V. On the Use and Abuse of N2 Physisorption for the Characterization of the Pore Structure of Shales; CMS workshop Lett. 2016, 21, 151–161. https://doi.org/10.1346/CMS-WLS-21.12.
(76) Duer, M. J. Solid State NMR Spectroscopy: Principles and Applications; John Wiley & Sons, 2008, pp. 592.

(77) Morozzi, P.; Ballarin, B.; Arcozzi, S.; Brattich, E.; Lucarelli, F.; Nava, S.; Gómez-Cascales, P. J.; Orza, J. A. G.; Tositti, L. Ultraviolet–Visible Diffuse Reflectance Spectroscopy (UV–Vis DRS), a Rapid and Non-Destructive Analytical Tool for the Identification of Saharan Dust Events in Particulate Matter Filters. Atmos. Environ. 2021, 252, 118297. https://doi.org/10.1016/j.atmosenv.2021.118297.

(78) Ishii, T.; Kyotani, T. Chapter 14 - Temperature Programmed Desorption. In Materials Science and Engineering of Carbon; Inagaki, M.; Kang, F. Eds.; Butterworth-Heinemann, 2016; pp 287–305. https://doi.org/10.1016/B978-0-12-805256-3.00014-3.

(79) Canepari, S.; Perrino, C.; Olivieri, F.; Astolfi, M. L. Characterisation of the Traffic Sources of PM through Size-Segregated Sampling, Sequential Leaching and ICP Analysis. Atmos. Environ. 2008, 42 (35), 8161–8175. https://doi.org/10.1016/j.atmosenv.2008.07.052.

(80) Zhang, X.; Vajglova, Z.; Mäki-Arvela, P.; Peurla, M.; Palonen, H.; Murzin, D. Yu.; Tungatarova, S. A.; Baizhumanova, T. S.; Aubakirov, Y. A. Mono- and Bimetallic Ni−Co Catalysts in Dry Reforming of Methane. ChemistrySelect 2021, 6 (14), 3424–3434. https://doi.org/10.1002/slct.202100686.

(81) Marafi, M.; Stanislaus, A. Spent Catalyst Waste Management: A Review: Part I—Developments in Hydroprocessing Catalyst Waste Reduction and Use. Resour. Conserv. Recycl. 2008, 52 (6), 859–873. https://doi.org/10.1016/j.resconrec.2008.02.004.

(82) Jimenez-Martin, J. M.; Orozco-Saumell, A.; Hernando, H.; Linares, M.; Mariscal, R.; López Granados, M.; García, A.; Iglesias, J. Efficient Conversion of Glucose to Methyl Lactate with Sn-USY: Retro-Aldol Activity Promotion by Controlled Ion Exchange. ACS Sustain. Chem. Eng. 2022, 10 (27), 8885–8896. https://doi.org/10.1021/acssuschemeng.2c01987.

(83) Pethő, D.; Kurusta, T.; Kristály, F.; Mikó, T.; Gácsi, Z. The Effect of Ball to Powder Ratio on the Processing of a Novel Mo-Cu-Al2O3 Composite. Int. J. Refract. Met. Hard Mater. 2021, 101, 105657. https://doi.org/10.1016/j.ijrmhm.2021.105657.

(84) Kholkina, E.; Kumar, N.; Eränen, K.; Russo, V.; Rahkila, J.; Peurla, M.; Wärnå, J.; Lehtonen, J.; Murzin, D. Yu. Carboxymethylation of Cinnamylalcohol with Dimethyl Carbonate over the Slag-Based Catalysts. React. Kinet. Mech. Catal. 2021, 133 (2), 601–630. https://doi.org/10.1007/s11144-021-02021-9.

(85) Emeis, C. A. Determination of integrated molar extinction coefficients for infrared absorption bands of pyridine adsorbed on solid acid catalysts. J. Catal. 1993, 141(2), 347-354.

(86) Jeanjean, J.; Aouali, L.; Delafosse, D.; Dereigne, A. Crystal Structure of Different Dealuminated Y-Type Zeolites Determination of Framework Vacancies and Non-Framework Species. J. Chem. Soc. Faraday Trans. 1 Phys. Chem. Condens. Phases 1989, 85 (9), 2771–2783. https://doi.org/10.1039/F19898502771.

(87) Baur, W. H.; Khan, A. A. Rutile-Type Compounds. IV. SiO2, GeO2 and a Comparison with Other Rutile-Type Structures. Acta Crystallogr. B. 1971, 27 (11), 2133–2139. https://doi.org/10.1107/S0567740871005466.

(88) Amin, Dr. G.; Asif, M.; Zainelabdin, A.; Zaman, S.; Nur, O.; Willander, M. Influence of PH, Precursor Concentration, Growth Time, and Temperature on the Morphology of ZnO Nanostructures Grown by the Hydrothermal Method. J. Nanomater. 2011, 5-5, https://doi.org/10.1155/2011/269692.

(89) Chu, Y.; Chen, S.; Zheng, J.; Li, Z. Elimination of Oxidation and Decomposition by SnCl2 in the SERS Study of Pyridoxine on a Roughened Au Electrode. J. Raman Spectrosc. 2009, 40 (2), 229–233. https://doi.org/10.1002/jrs.2117.

(90) Iyoki, K.; Itabashi, K.; Okubo, T. Progress in Seed-Assisted Synthesis of Zeolites without Using Organic Structure-Directing Agents. Micropor. Mesop. Mater. 2014, 189, 22–30. https://doi.org/10.1016/j.micromeso.2013.08.008.
(91) Zhang, X.; Tang, D.; Zhang, M.; Yang, R. Synthesis of NaX Zeolite: Influence of Crystallization Time, Temperature and Batch Molar Ratio SiO2/Al2O3 on the Particulate Properties of Zeolite Crystals. Powder Technol. 2013, 235, 322–328. https://doi.org/10.1016/j.powtec.2012.10.046.
(92) Wei, C.; Zhang, G.; Zhao, L.; Gao, J.; Xu, C. Effect of Metal–Acid Balance and Textual Modifications on Hydroisomerization Catalysts for n-Alkanes with Different Chain Length: A Mini-Review. Fuel 2022, 315, 122809. https://doi.org/10.1016/j.fuel.2021.122809.
(93) Chu, N. T. H.; Ngo, Q. L. D.; Le, H. T. T. Synthesis of Ordered Mesoporous Carbon from Vietnam Natural Kaolin Clay for Supercapacitor Application. Mater. Sci. Forum 2020, 985, 124–136. https://doi.org/10.4028/www.scientific.net/MSF.985.124.
(94) Ren, L.; Wang, B.; Lu, K.; Peng, R.; Guan, Y.; Jiang, J.; Xu, H.; Wu, P. Selective Conversion of Methanol to Propylene over Highly Dealuminated Mordenite: Al Location and Crystal Morphology Effects. Chin. J. Catal. 2021, 42 (7), 1147–1159. https://doi.org/10.1016/S1872-2067(20)63726-3.
(95) Lee, M.-H.; Nagaraja, B. M.; Natarajan, P.; Truong, N. T.; Lee, K. Y.; Yoon, S.; Jung, K.-D. Effect of Potassium Addition on Bimetallic PtSn/θ-Al2O3 Catalyst for Dehydrogenation of Propane to Propylene. Res. Chem. Intermed. 2016, 42 (1), 123–140. https://doi.org/10.1007/s11164-015-2370-1.
(96) Mäki-Arvela, P.; Kumar, N.; Diáz, S. F.; Aho, A.; Tenho, M.; Salonen, J.; Leino, A.-R.; Kordás, K.; Laukkanen, P.; Dahl, J.; Sinev, I.; Salmi, T.; Murzin, D. Yu. Isomerization of β-Pinene Oxide over Sn-Modified Zeolites. J. Mol. Catal. Chem. 2013, 366, 228–237. https://doi.org/10.1016/j.molcata.2012.09.028.
(97) González-Cortés, S. L.; Rugmini, S.; Xiao, T.; Green, M. L. H.; Rodulfo-Baechler, S. M.; Imbert, F. E. Deep Hydrotreating of Different Feedstocks over a Highly Active Al2O3-Supported NiMoW Sulfide Catalyst. Appl. Catal. Gen. 2014, 475, 270–281. https://doi.org/10.1016/j.apcata.2014.01.045.
(98) Zhang, H.; Shao, S.; Xiao, R.; Shen, D.; Zeng, J. Characterization of Coke Deposition in the Catalytic Fast Pyrolysis of Biomass Derivates. Energy Fuels 2014, 28 (1), 52–57. https://doi.org/10.1021/ef401458y.
(99) Wang, K.; Yang, Z.; Ma, Y.; Zhao, W.; Sun, J.; Lu, T.; He, H. Recent advances in the utilization of glycerol for the production of lactic acid by catalysis. Biofuels, Bioproducts and Biorefining 2022, 16(5), 1428-1454.
(100) He, J.; Li, H.; Saravanamurugan, S.; Yang, S. Catalytic Upgrading of Biomass-Derived Sugars with Acidic Nanoporous Materials: Structural Role in Carbon-Chain Length Variation. ChemSusChem 2019, 12 (2), 347–378. https://doi.org/10.1002/cssc.201802113.
(101) Liu, G.; Jiang, J.-G.; Yang, B.; Fang, X.; Xu, H.; Peng, H.; Xu, L.; Liu, Y.; Wu, P. Hydrothermal Synthesis of MWW-Type Stannosilicate and Its Post-Structural Transformation to MCM-56 Analogue. Micropor. Mesop. Mater. 2013, 165, 210–218. https://doi.org/10.1016/j.micromeso.2012.08.025.
(102) Chon, H.; Woo, S. I.; Park, S.-E. Recent Advances and New Horizons in Zeolite Science and Technology; Studies in surface science and catalysis. Taejon, Elsevier, 1996.
(103) Palčić, A.; Valtchev, V. Analysis and Control of Acid Sites in Zeolites. Appl. Catal. Gen. 2020, 606, 117795. https://doi.org/10.1016/j.apcata.2020.117795.

(104) Martínez, C.; Corma, A. Inorganic Molecular Sieves: Preparation, Modification and Industrial Application in Catalytic Processes. Coord. Chem. Rev. 2011, 255 (13), 1558–1580. https://doi.org/10.1016/j.ccr.2011.03.014.
(105) Iglesias, J.; Moreno, J.; Morales, G.; A. Melero, J.; Juárez, P.; López-Granados, M.; Mariscal, R.; Martínez-Salazar, I. Sn–Al-USY for the Valorization of Glucose to Methyl Lactate: Switching from Hydrolytic to Retro-Aldol Activity by Alkaline Ion Exchange. Green Chem. 2019, 21 (21), 5876–5885. https://doi.org/10.1039/C9GC02609F.
(106) Kubička, D.; Kumar, N.; Venäläinen, T.; Karhu, H.; Kubičková, I.; Österholm, H.; Murzin, D. Y. Metal− support interactions in zeolite-supported noble metals: Influence of metal crystallites on the support acidity. J. Phys. Chem. B 2006, 110(10), 4937-4946.
(107) Al-Nayili, A.; Albdiry, M.; Salman, N. Dealumination of zeolite frameworks and Lewis acid catalyst activation for transfer hydrogenation. Arab. J. Sci. Eng., 2021, 46, 5709-5716.
(108) Sohn, H. Fabrication of porous materials (metal, metal oxide and semiconductor) through an aerosol-assisted route. PhD Thesis, University of California, Los Angeles. 2021, p. 200.
(109) Mäki-Arvela, P.; Murzin, D. Yu. Effect of Catalyst Synthesis Parameters on the Metal Particle Size. Appl. Catal. Gen. 2013, 451, 251–281. https://doi.org/10.1016/j.apcata.2012.10.012.
(110) Ishihara, A.; Matsuura, S.; Hayashi, F.; Suemitsu, K.; Hashimoto, T. Estimation of Catalytic Cracking of Vacuum Gas Oil by a Y Zeolite-Containing Two-Layered Catalyst and a Novel Three-Layered Hierarchical Catalyst Using a Curie Point Pyrolyzer Method. Energy Fuels 2020, 34 (6), 7448–7454. https://doi.org/10.1021/acs.energyfuels.0c00957.
(111) Wang, Y.; Yokoi, T.; Namba, S.; Tatsumi, T. . Effects of dealumination and desilication of beta zeolite on catalytic performance in n-hexane cracking. Catalysts 2016, 6(1), 8.
(112) Corma, A.; Iborra, S.; Velty, A. Chemical routes for the transformation of biomass into chemicals. Chem. Rev. 2007, 107(6), 2411-2502.
(113) Ma, Q.; Fu, T.; Li, H.; Cui, L.; Li, Z. Insight into the Selection of the Post-Treatment Strategy for ZSM-5 Zeolites for the Improvement of Catalytic Stability in the Conversion of Methanol to Hydrocarbons. Ind. & Engn Chem. Res. 2020, 59(24), 11125-11138.
(114) Vishal, V.; Chandra, D.; Bahadur, J.; Sen, D.; Hazra, B.; Mahanta, B.; Mani, D. Interpreting pore dimensions in gas shales using a combination of SEM imaging, small-angle neutron scattering, and low-pressure gas adsorption. Energy & Fuels, 2019, 33(6), 4835-4848.
(115) Kumar, N.; Nieminen, V.; Demirkan, K.; Salmi, T.; Yu. Murzin, D.; Laine, E. Effect of Synthesis Time and Mode of Stirring on Physico-Chemical and Catalytic Properties of ZSM-5 Zeolite Catalysts. Appl. Catal. Gen. 2002, 235 (1), 113–123. https://doi.org/10.1016/S0926-860X(02)00258-2.
(116) Bodachivskyi, I.; Kuzhiumparambil, U.; Williams, D. B. G. A Systematic Study of Metal Triflates in Catalytic Transformations of Glucose in Water and Methanol: Identifying the Interplay of Brønsted and Lewis Acidity. ChemSusChem 2019, 12 (14), 3263–3270. https://doi.org/10.1002/cssc.201900292.
(117) Taghavi, S.; Ghedini, E.; Menegazzo, F.; Mäki-Arvela, P.; Peurla, M.; Zendehdel, M.; Cruciani, G.; Di Michele, A.; Murzin, D. Yu.; Signoretto, M. CuZSM-5@HMS Composite as an Efficient Micro-Mesoporous Catalyst for Conversion of Sugars into Levulinic Acid. Catal. Today 2022, 390–391, 146–161. https://doi.org/10.1016/j.cattod.2021.11.038.
(118) Azadi, P.; Carrasquillo-Flores, R.; J. Pagán-Torres, Y.; I. Gürbüz, E.; Farnood, R.; A. Dumesic, J. Catalytic Conversion of Biomass Using Solvents Derived from Lignin. Green Chem. 2012, 14 (6), 1573–1576. https://doi.org/10.1039/C2GC35203F.

(119) Saab, R.; Polychronopoulou, K.; Anjum, D. H.; Charisiou, N. D.; Goula, M. A.; Hinder, S. J.; Baker, M. A.; Schiffer, A. Effect of SiO2/Al2O3 Ratio in Ni/Zeolite-Y and Ni-W/Zeolite-Y Catalysts on Hydrocracking of Heptane. Mol. Catal. 2022, 528, 112484. https://doi.org/10.1016/j.mcat.2022.112484.
(120) Murzin, D. Y.; Salmi, T. Catalytic Kinetics; Elsevier, 2005, pp. 492.
(121) Kubička, D.; Kumar, N.; Mäki-Arvela, P.; Tiitta, M.; Niemi, V.; Salmi, T.; Murzin, D. Y. Ring Opening of Decalin over Zeolites: I. Activity and Selectivity of Proton-Form Zeolites. J. Catal. 2004, 222 (1), 65–79. https://doi.org/10.1016/j.jcat.2003.10.027.
(122) Zhang, H.; Hu, Y.; Qi, L.; He, J.; Li, H.; Yang, S. Chemocatalytic Production of Lactates from Biomass-Derived Sugars. Int. J. Chem. Eng. 2018, 1-18. https://doi.org/10.1155/2018/7617685.
(123) Hu, W.; Chi, Z.; Wan, Y.; Wang, S.; Lin, J.; Wan, S.; Wang, Y. Synergetic Effect of Lewis Acid and Base in Modified Sn-β on the Direct Conversion of Levoglucosan to Lactic Acid. Catal. Sci. Technol. 2020, 10 (9), 2986–2993. https://doi.org/10.1039/D0CY00089B.
(124) Guo, Q.; Fan, F.; Pidko, E. A.; Van Der Graaff, W. N.; Feng, Z.; Li, C.; Hensen, E. J. Highly Active and Recyclable Sn-MWW Zeolite Catalyst for Sugar Conversion to Methyl Lactate and Lactic Acid. ChemSusChem 2013, 6(8), 1352-1356.
(125) Yue, X.-Y.; Ren, H.-F.; Wu, C.; Xu, J.; Li, J.; Liu, C.-L.; Dong, W.-S. Highly Efficient Conversion of Glucose to Methyl Lactate over Hierarchical Bimetal-Doped Beta Zeolite Catalysts. J. Chem. Technol. Biotechnol. 2021, 96 (8), 2238–2248. https://doi.org/10.1002/jctb.6748.
(126) Guo, Q.; Fan, F.; Pidko, E. A.; van der Graaff, W. N. P.; Feng, Z.; Li, C.; Hensen, E. J. M. Highly Active and Recyclable Sn-MWW Zeolite Catalyst for Sugar Conversion to Methyl Lactate and Lactic Acid. ChemSusChem 2013, 6 (8), 1352–1356. https://doi.org/10.1002/cssc.201300160.
(127) Yang, X.; Wang, Y.; Yunlai, su; Zhou, L. Influence of Sn Content in Sn-β on Selective Production of Methyl Lactate from Glucose. Catal. Lett. 2022, 153, 1–13. https://doi.org/10.1007/s10562-022-04101-4.
(128) Zhang, W.; Xu, S.; Xiao, Y.; Qin, D.; Li, J.; Hu, C. The Insights into the Catalytic Performance of Rare Earth Metal Ions on Lactic Acid Formation from Biomass via Microwave Heating. Chem. Eng. J. 2021, 421, 130014. https://doi.org/10.1016/j.cej.2021.130014.
(129) Wang, G.; Lv, K.; Chen, T.; Chen, Z.; Hu, J. Immobilizing of Palladium on Melamine Functionalized Magnetic Chitosan Beads: A Versatile Catalyst for p-Nitrophenol Reduction and Suzuki Reaction in Aqueous Medium. Int. J. Biol. Macromol. 2021, 184, 358–368. https://doi.org/10.1016/j.ijbiomac.2021.06.055.
(130) Saldanha, L. A. S.; Santos, N. T.; Das G.; Tomaz, E. Photocatalytic Ethylbenzene Degradation Associated with Ozone (TiO2/UV/O3) under Different Percentages of Catalytic Coating Area: Evaluation of Process Parameters. Sep. Purif. Technol. 2021, 263, 118344. https://doi.org/10.1016/j.seppur.2021.118344.
(131) Vizcaíno, A.; Arena, P.; Baronetti, G.; Carrero, A.; Calles, J.; Laborde, M. A.; Amadeo, N. Ethanol Steam Reforming on Ni/Al2O3 Catalysts: Effect of Mg Addition. Int. J. Hydrog. Energy 2008, 33, 3489–3492. https://doi.org/10.1016/j.ijhydene.2007.12.012.
(132) Mastroianni, L.; Vajglová, Z.; Eränen, K.; Peurla, M.; Di Serio, M.; Yu. Murzin, D.; Russo, V.; Salmi, T. Microreactor Technology in Experimental and Modelling Study of Alcohol Oxidation on Nanogold. Chem. Eng. Sci. 2022, 260, 117920. https://doi.org/10.1016/j.ces.2022.117920.

(133) Liu, L.; Lopez-Haro, M.; Lopes, C. W.; Li, C.; Concepcion, P.; Simonelli, L.; Calvino, J. J.; Corma, A. Regioselective Generation and Reactivity Control of Subnanometric Platinum Clusters in Zeolites for High-Temperature Catalysis. Nat. Mater. 2019, 18 (8), 866–873. https://doi.org/10.1038/s41563-019-0412-6.
(134) Zhang, Y.; Luo, H.; Zhao, X.; Zhu, L.; Miao, G.; Wang, H.; Li, S.; Kong, L. Continuous Conversion of Glucose into Methyl Lactate over the Sn-Beta Zeolite: Catalytic Performance and Activity Insight. Ind. Eng. Chem. Res. 2020, 59 (39), 17365–17372. https://doi.org/10.1021/acs.iecr.0c01770.
(135) Tang, B.; Dai, W.; Wu, G.; Guan, N.; Li, L.; Hunger, M. Improved Postsynthesis Strategy to Sn-Beta Zeolites as Lewis Acid Catalysts for the Ring-Opening Hydration of Epoxides. ACS Catal. 2014, 4 (8), 2801–2810. https://doi.org/10.1021/cs500891s.
(136) Li, S.; Zheng, A.; Su, Y.; Fang, H.; Shen, W.; Yu, Z.; Chen, L.; Deng, F. Extra-Framework Aluminium Species in Hydrated Faujasite Zeolite as Investigated by Two-Dimensional Solid-State NMR Spectroscopy and Theoretical Calculations. Phys. Chem. Chem. Phys. 2010, 12 (15), 3895–3903. https://doi.org/10.1039/B915401A.
(137) Deng, F.; Yue, Y.; Ye, C. Observation of Nonframework Al Species in Zeolite β by Solid-State NMR Spectroscopy. J. Phys. Chem. B 1998, 102(27), 5252-5256.
(138) Mäki-Arvela, P.; Kaka khel, T. A.; Azkaar, M.; Engblom, S.; Murzin, D. Y. Catalytic Hydroisomerization of Long-Chain Hydrocarbons for the Production of Fuels. Catalysts 2018, 8 (11), 534. https://doi.org/10.3390/catal8110534.
(139) Villegas, J. I.; Kumar, N.; Heikkilä, T.; Lehto, V.-P.; Salmi, T.; Murzin, D. Yu. Isomerization of N-Butane to Isobutane over Pt-Modified Beta and ZSM-5 Zeolite Catalysts: Catalyst Deactivation and Regeneration. Chem. Eng. J. 2006, 120 (1), 83–89. https://doi.org/10.1016/j.cej.2006.03.011.
(140) Mäki-Arvela, P.; Aho, A.; Murzin, D. Y. Heterogeneous catalytic synthesis of methyl lactate and lactic acid from sugars and their derivatives. ChemSusChem, 2020, 13(18), 4833-4855.
(141) Cain, J.; Laskin, A.; Kholghy, M. R.; Thomson, M. J.; Wang, H. Molecular characterization of organic content of soot along the centerline of a coflow diffusion flame. Phys. Chem. Chem. Phys. 2014, 16(47), 25862-25875.
(142) Yan, H.; Yang, Y.; Tong, D.; Xiang, X.; Hu, C. Catalytic Conversion of Glucose to 5-Hydroxymethylfurfural over SO42−/ZrO2 and SO42−/ZrO2–Al2O3 Solid Acid Catalysts. Catal. Commun. 2009, 10 (11), 1558–1563. https://doi.org/10.1016/j.catcom.2009.04.020.

2. Appendix A:

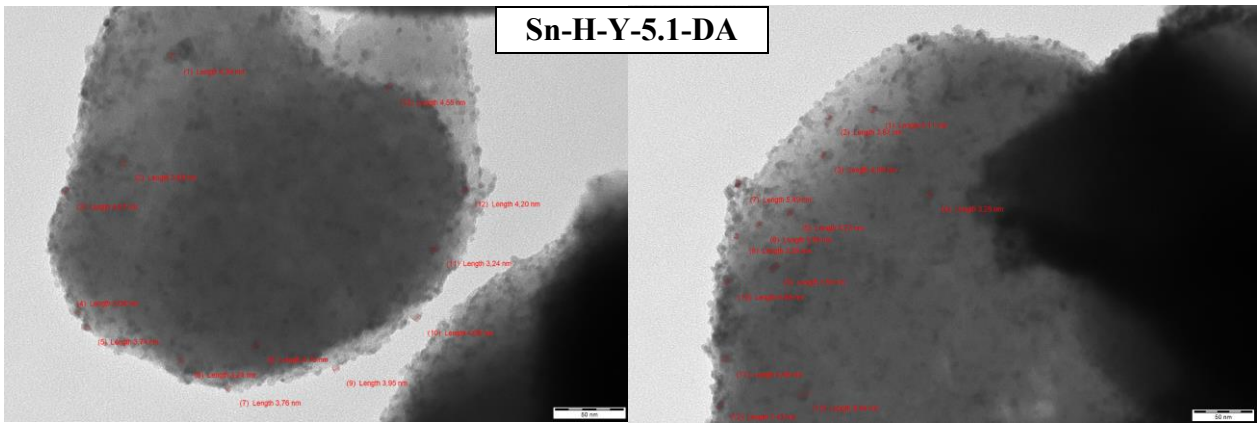

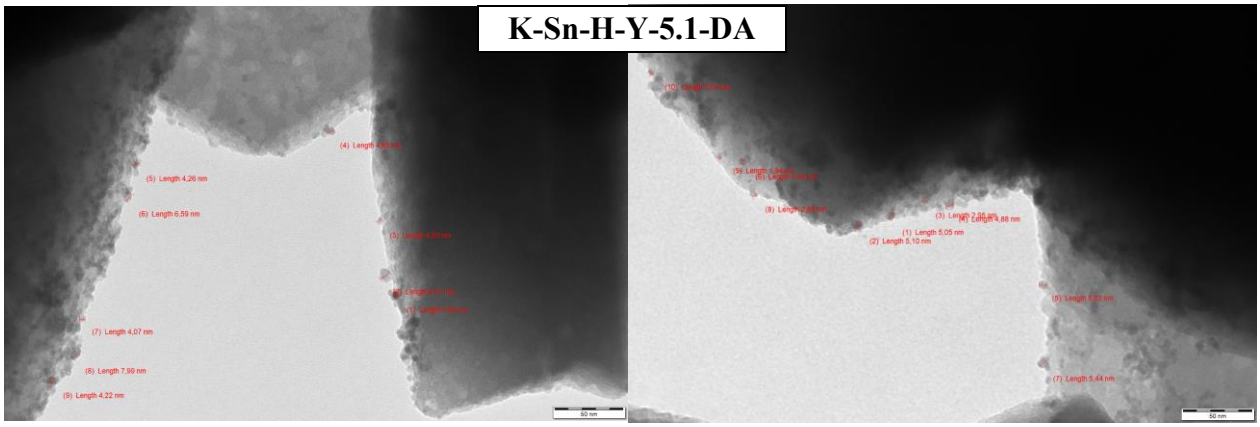

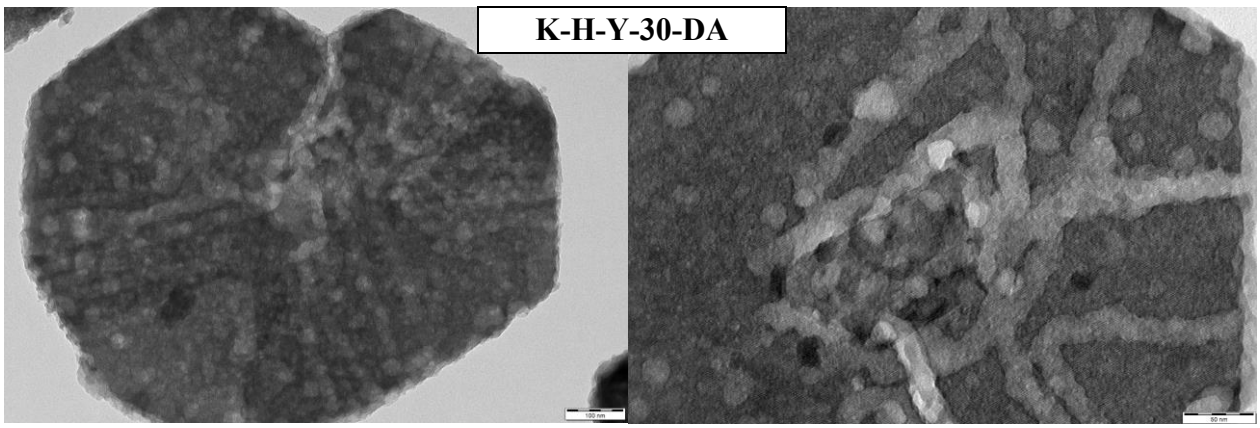

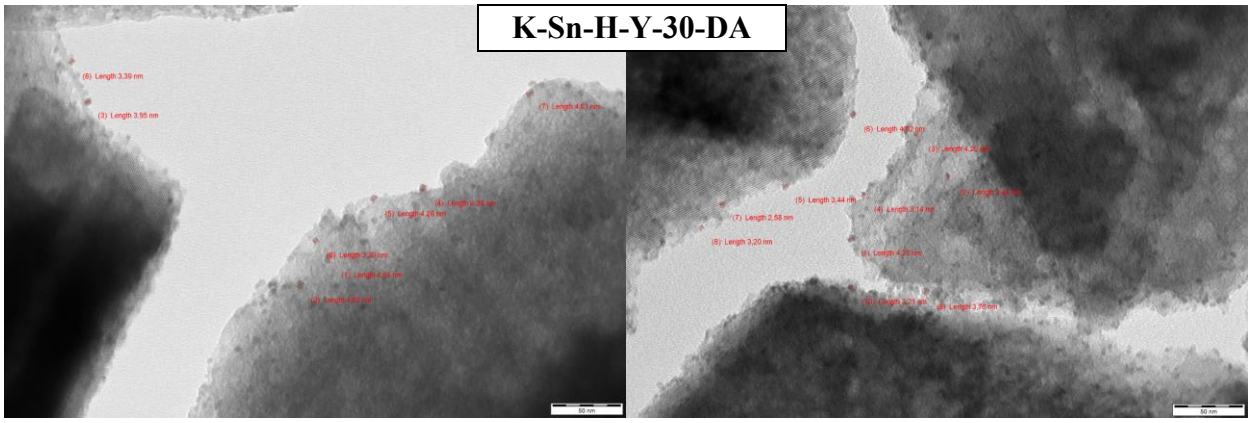
K-Sn-H-Y-30-DA

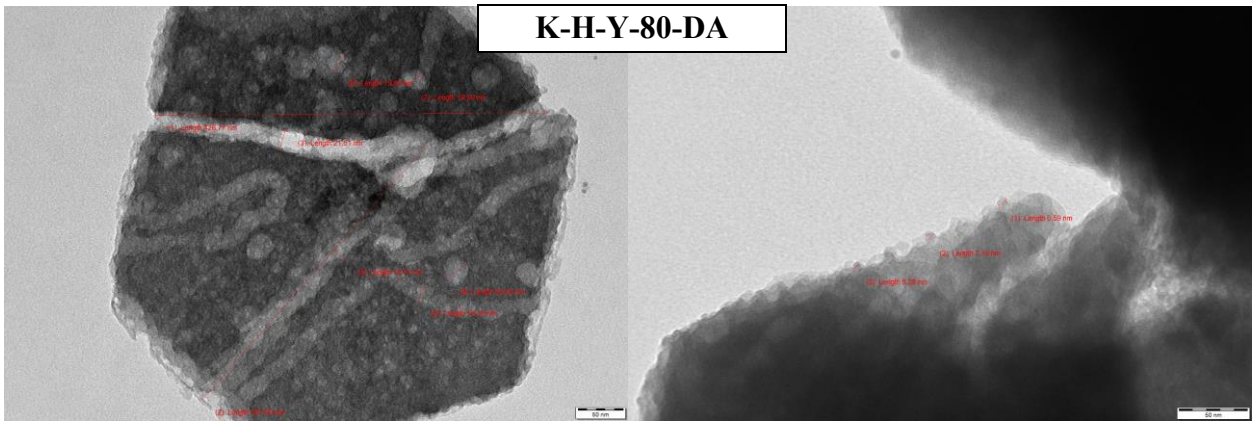
K-H-Y-80-DA

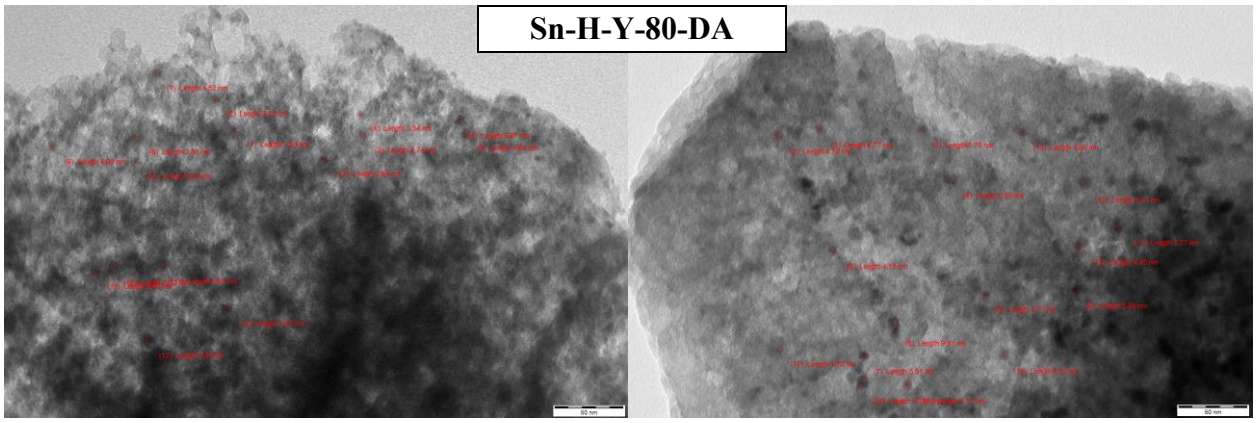
Sn-H-Y-80-DA

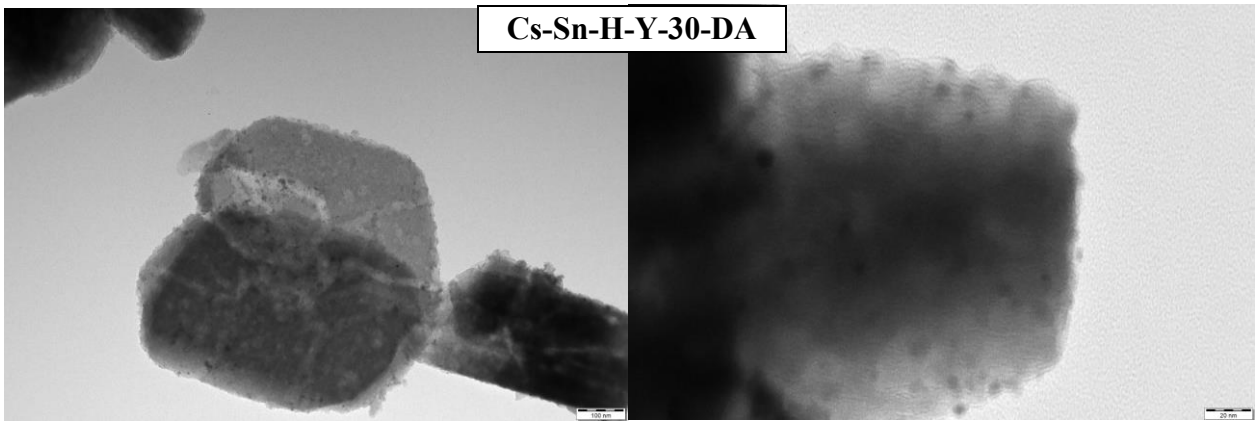
Cs-Sn-H-Y-30-DA

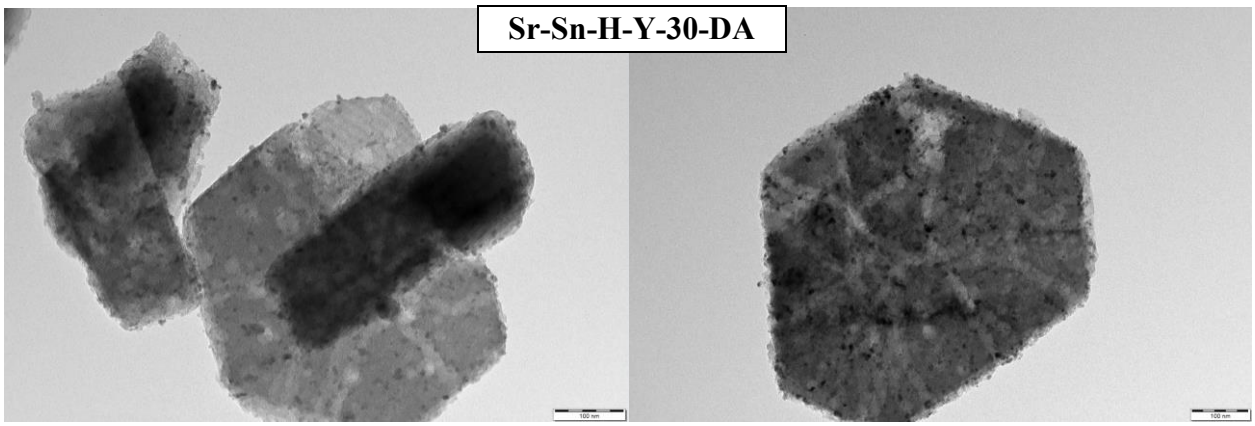
Sr-Sn-H-Y-30-DA

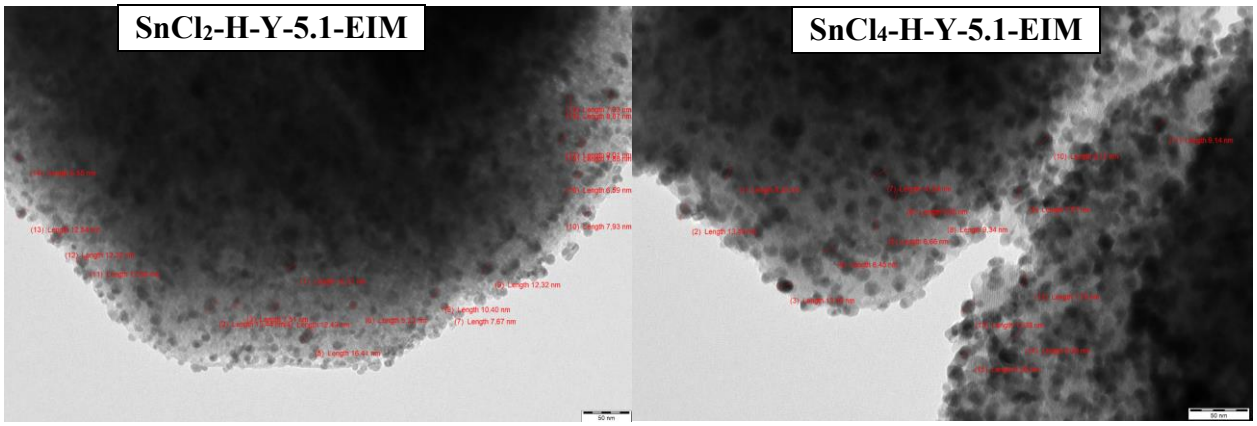
SnCl2-H-Y-5.1-EIM
SnCl4-H-Y-5.1-EIM

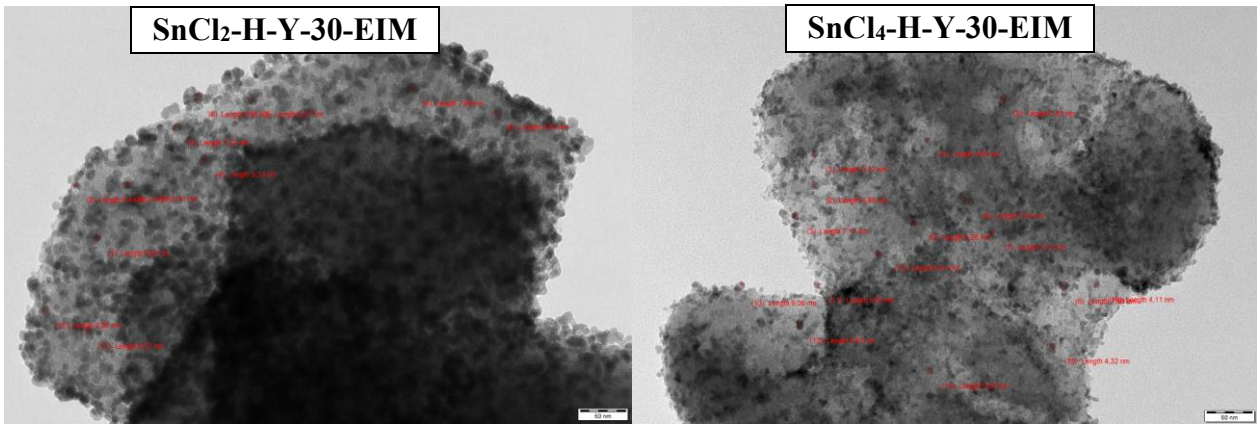
SnCl2-H-Y-30-EIM
SnCl4-H-Y-30-EIM

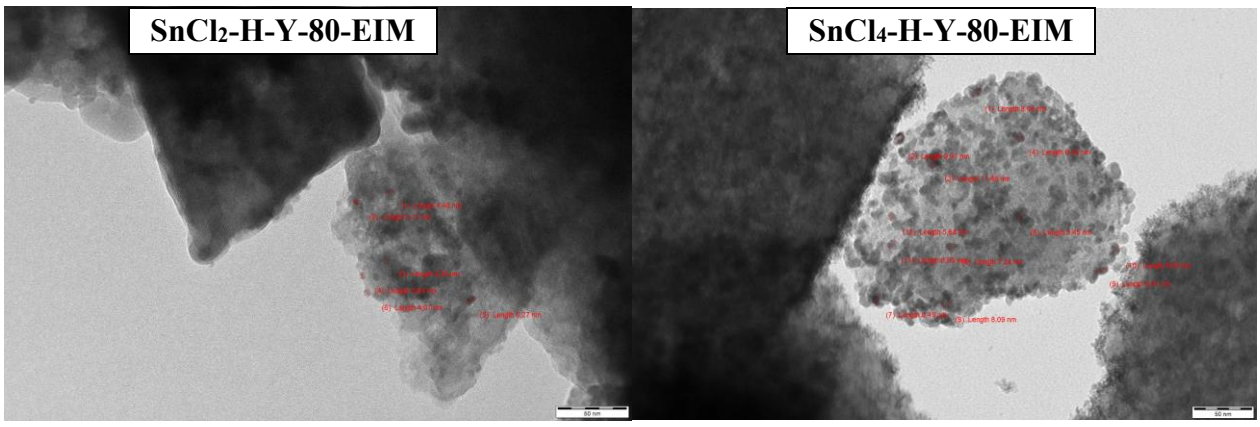
SnCl2-H-Y-80-EIM
SnCl4-H-Y-80-EIM

3. Appendix B: SEM images

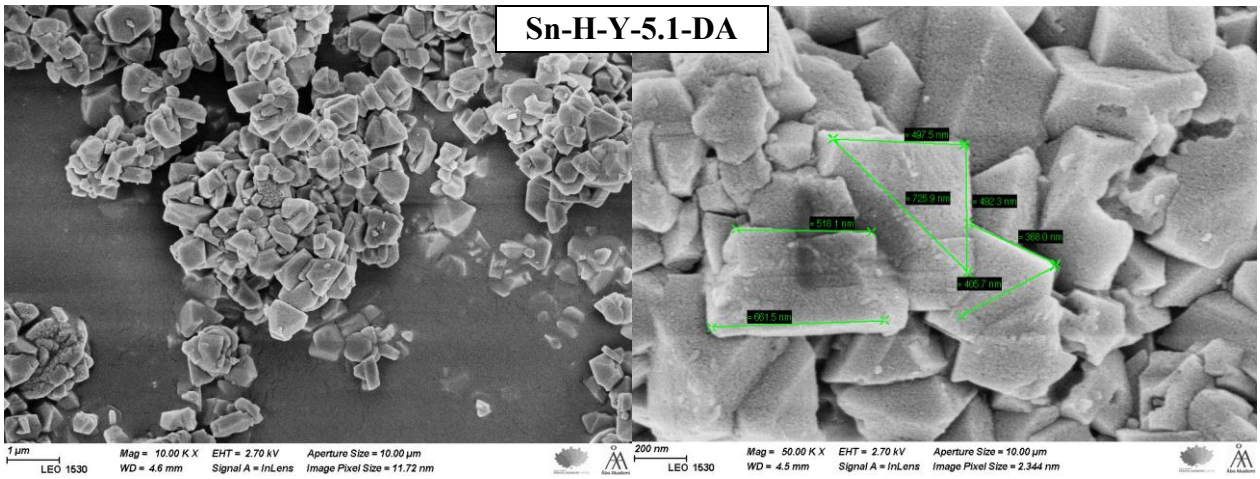

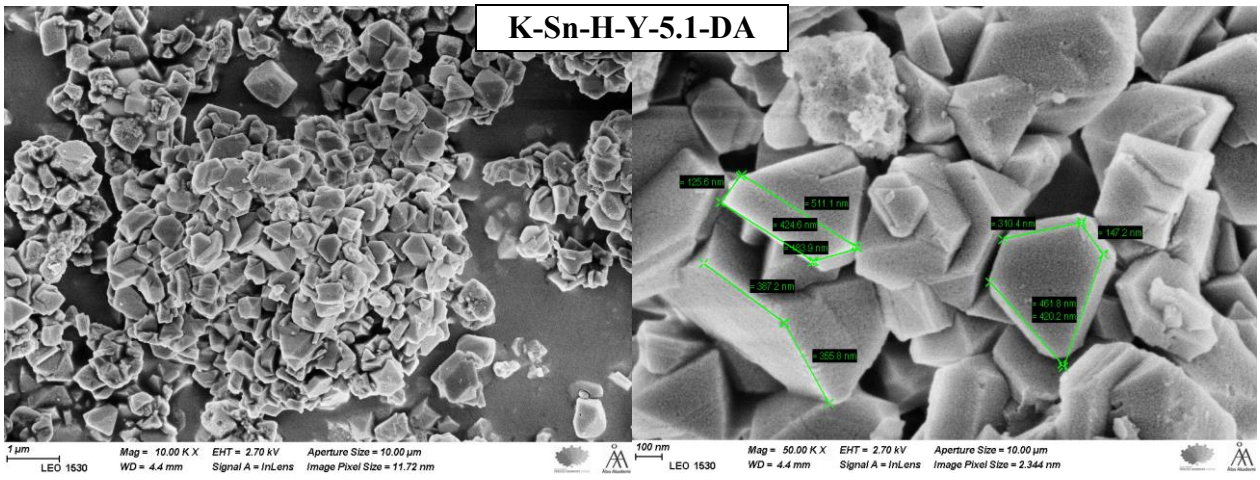

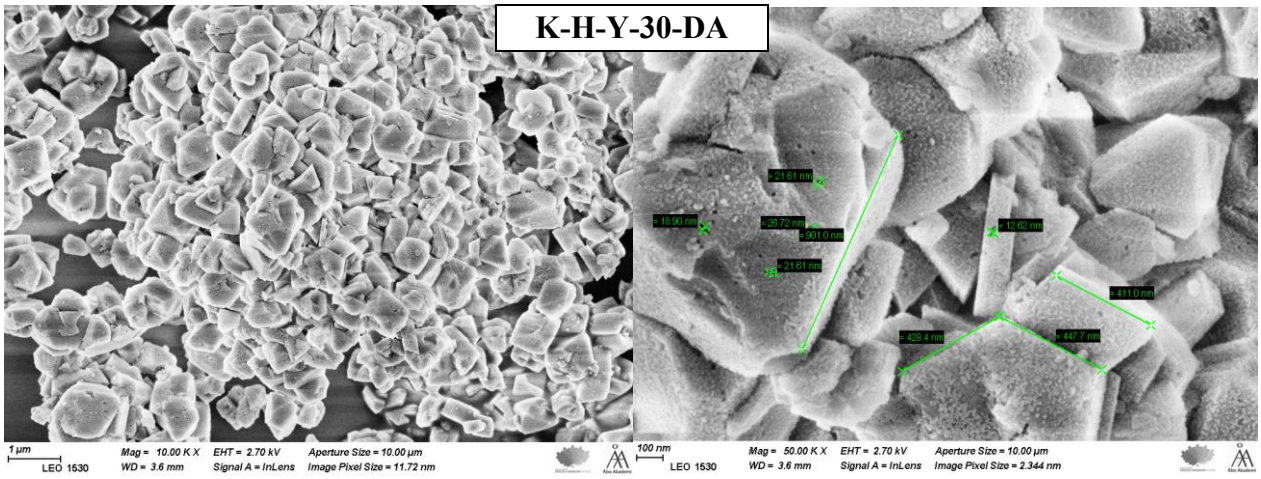

K-Sn-H-Y-30-DA

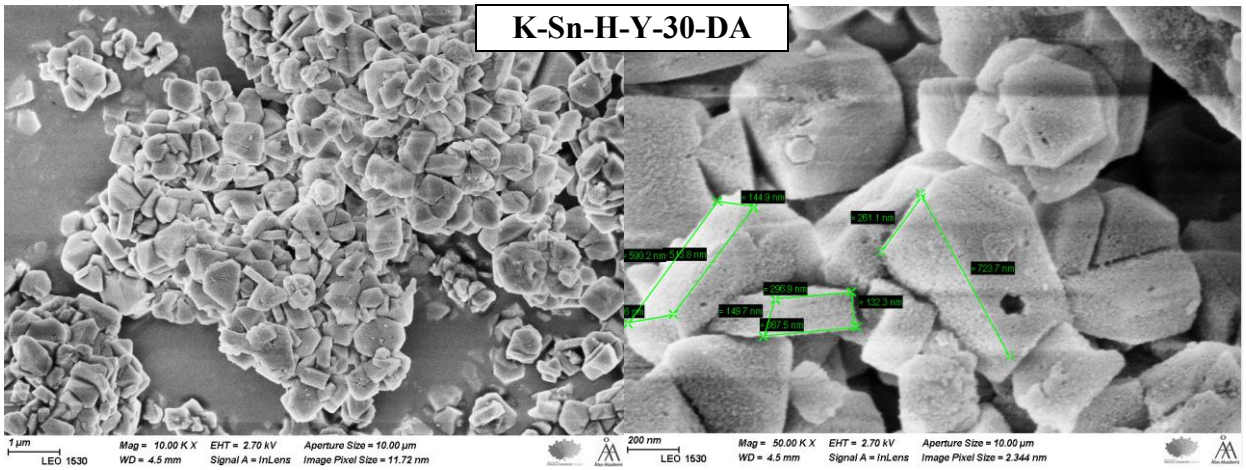

K-H-Y-80-DA

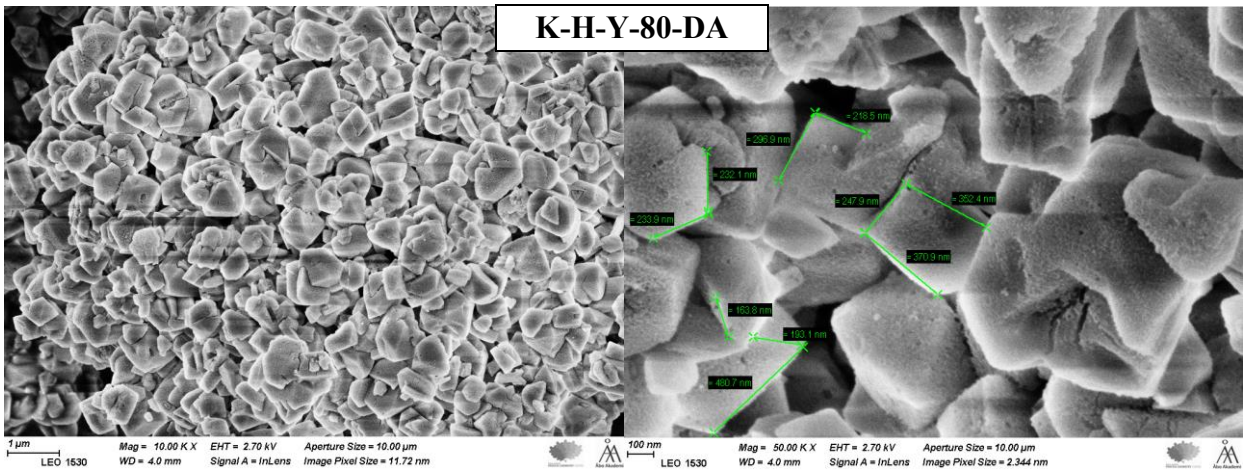

K-Sn-H-Y-80-DA

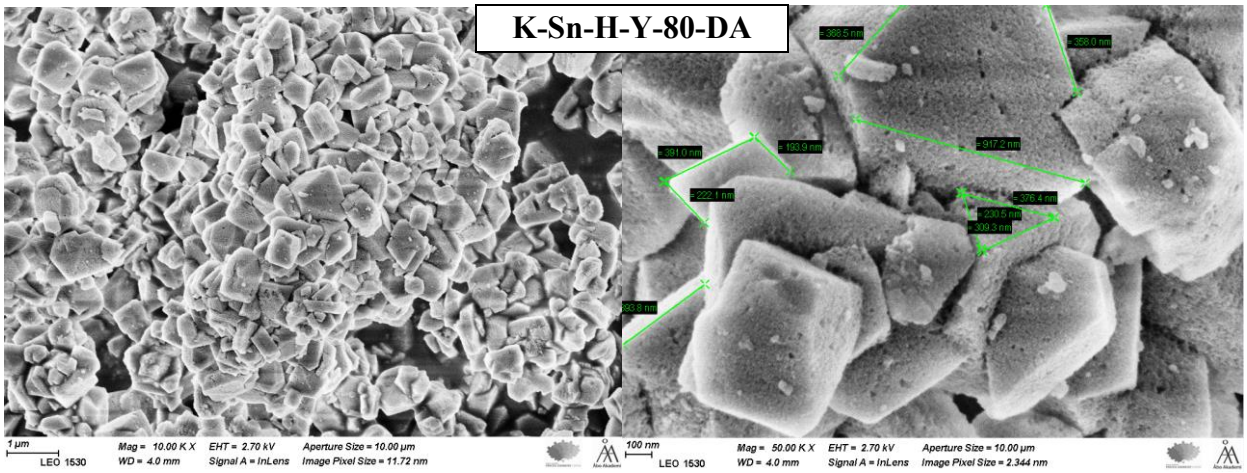

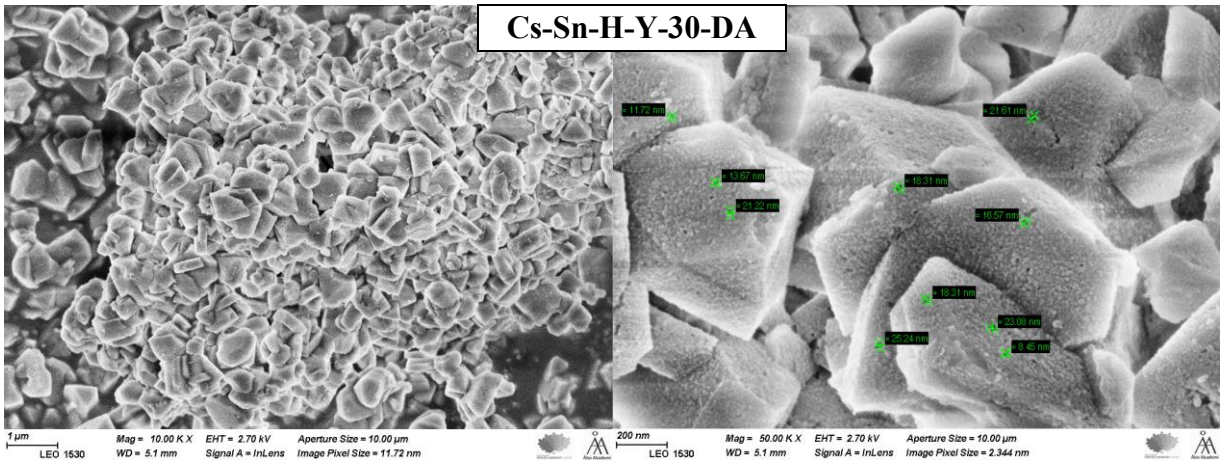
Cs-Sn-H-Y-30-DA
1 µm
LEO 1530
Mag = 10.00 K X
WD = 5.1 mm
EHT = 2.70 kV
Signal A = InLens
Aperture Size = 10.00 µm
Image Pixel Size = 11.72 nm
200 nm
LEO 1530
Mag = 50.00 K X
WD = 5.1 mm
EHT = 2.70 kV
Signal A = InLens
Aperture Size = 10.00 µm
Image Pixel Size = 2.344 nm

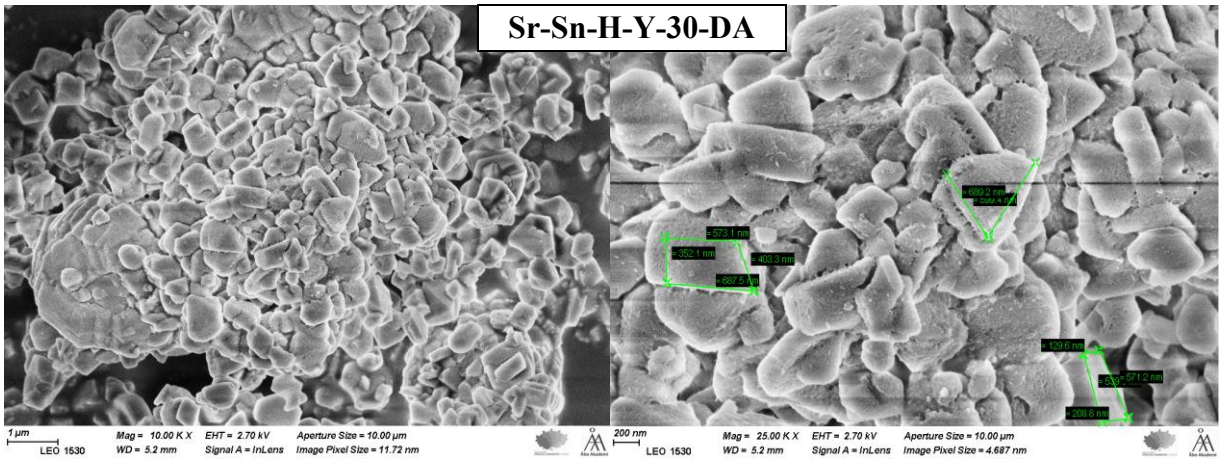
Sr-Sn-H-Y-30-DA
1 µm
LEO 1530
Mag = 10.00 K X
WD = 5.2 mm
EHT = 2.70 kV
Signal A = InLens
Aperture Size = 10.00 µm
Image Pixel Size = 11.72 nm
200 nm
LEO 1530
Mag = 25.00 K X
WD = 5.2 mm
EHT = 2.70 kV
Signal A = InLens
Aperture Size = 10.00 µm
Image Pixel Size = 4.687 nm

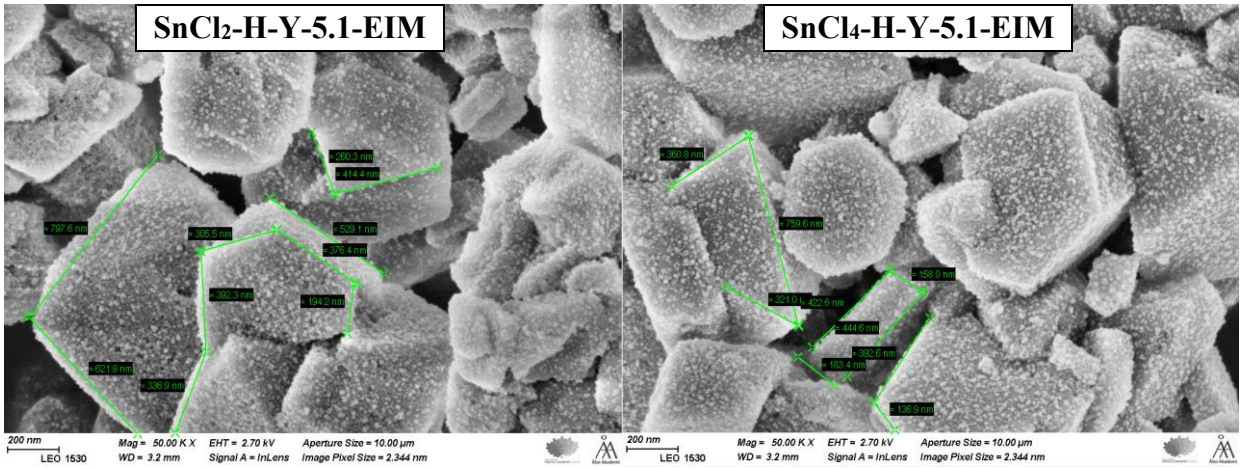
SnCl2-H-Y-5.1-EIM
SnCl4-H-Y-5.1-EIM
200 nm
LEO 1530
Mag = 50.00 K X
WD = 3.2 mm
EHT = 2.70 kV
Signal A = InLens
Aperture Size = 10.00 µm
Image Pixel Size = 2.344 nm
200 nm
LEO 1530
Mag = 50.00 K X
WD = 3.2 mm
EHT = 2.70 kV
Signal A = InLens
Aperture Size = 10.00 µm
Image Pixel Size = 2.344 nm

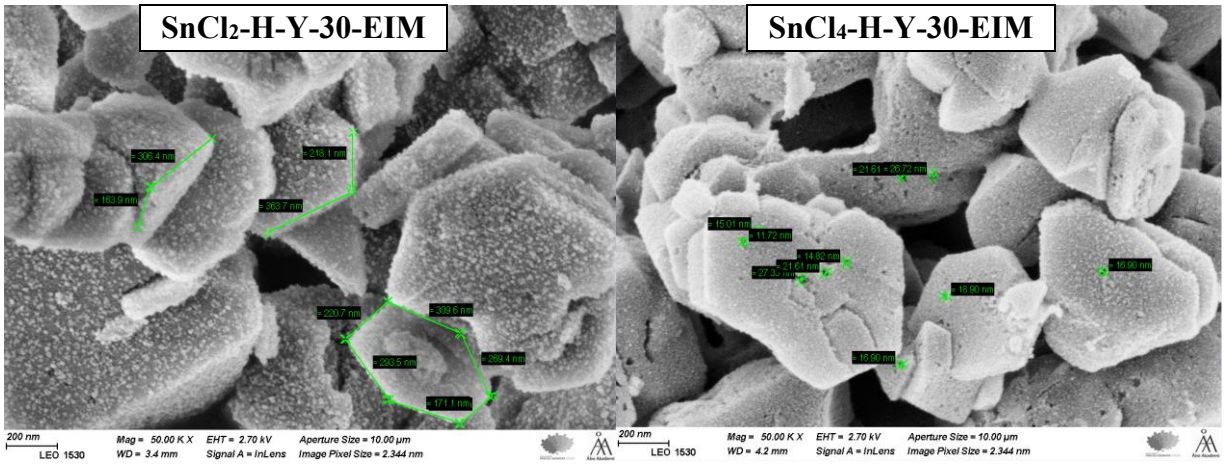
SnCl2-H-Y-30-EIM
SnCl4-H-Y-30-EIM
200 nm
LEO 1530
Mag = 50.00 K X
EHT = 2.70 kV
Aperture Size = 10.00 µm
WD = 3.4 mm
Signal A = InLens
Image Pixel Size = 2.344 nm
200 nm
LEO 1530
Mag = 50.00 K X
EHT = 2.70 kV
Aperture Size = 10.00 µm
WD = 4.2 mm
Signal A = InLens
Image Pixel Size = 2.344 nm

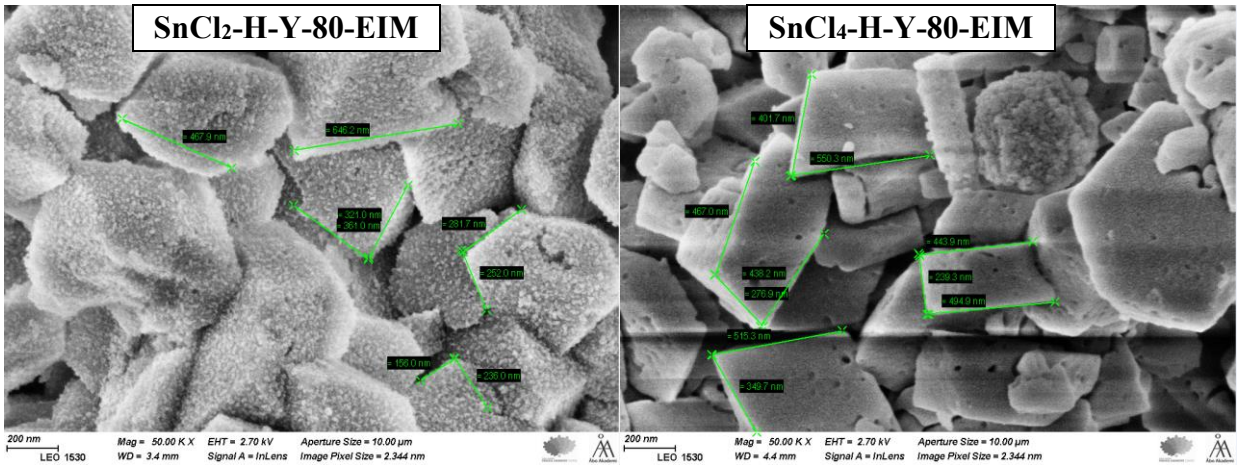
SnCl2-H-Y-80-EIM
SnCl4-H-Y-80-EIM
200 nm
LEO 1530
Mag = 50.00 K X
EHT = 2.70 kV
Aperture Size = 10.00 µm
WD = 3.4 mm
Signal A = InLens
Image Pixel Size = 2.344 nm
200 nm
LEO 1530
Mag = 50.00 K X
EHT = 2.70 kV
Aperture Size = 10.00 µm
WD = 4.4 mm
Signal A = InLens
Image Pixel Size = 2.344 nm

4. Appendix C: Liquid nitrogen physisorption results

H-Y-30-DA (790 m^2/g)

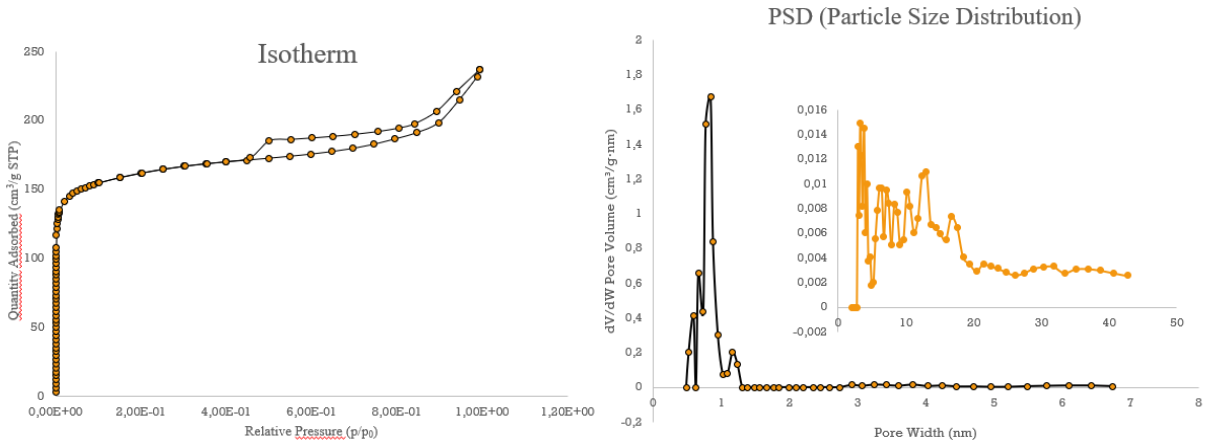

Sn-H-Y-30-DA (710 m^2/g)

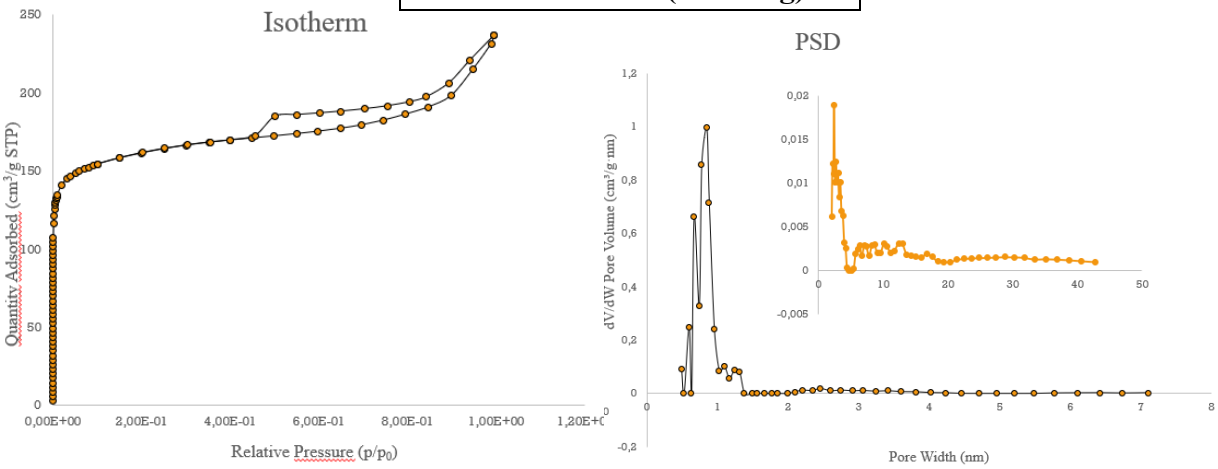

K-Sn-H-Y-30-DA (550 m^2/g)

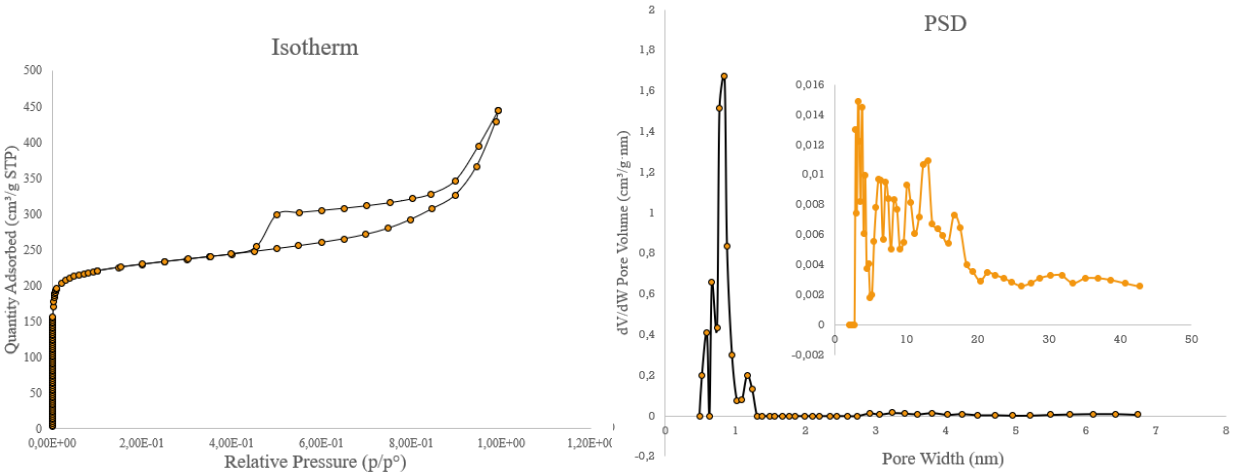

Spent-K-Sn-H-Y-30-DA (510 m^2/g)

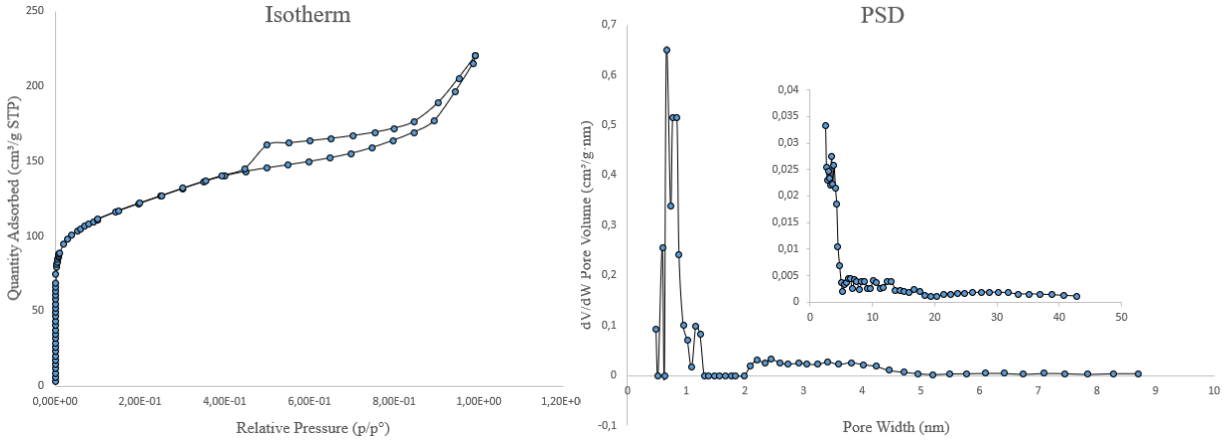

H-Y-80-DA (590 m^2/g)

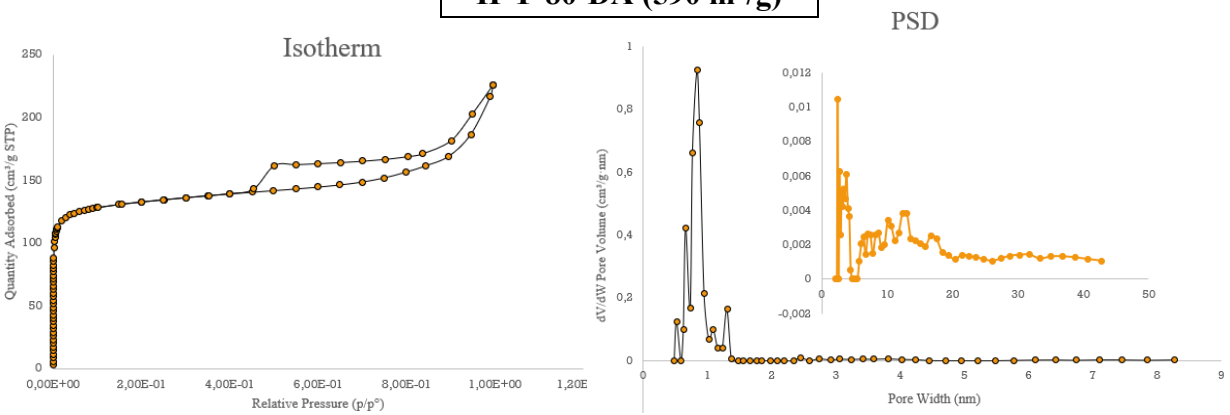

Sn-H-Y-80-DA (600 m^2/g)

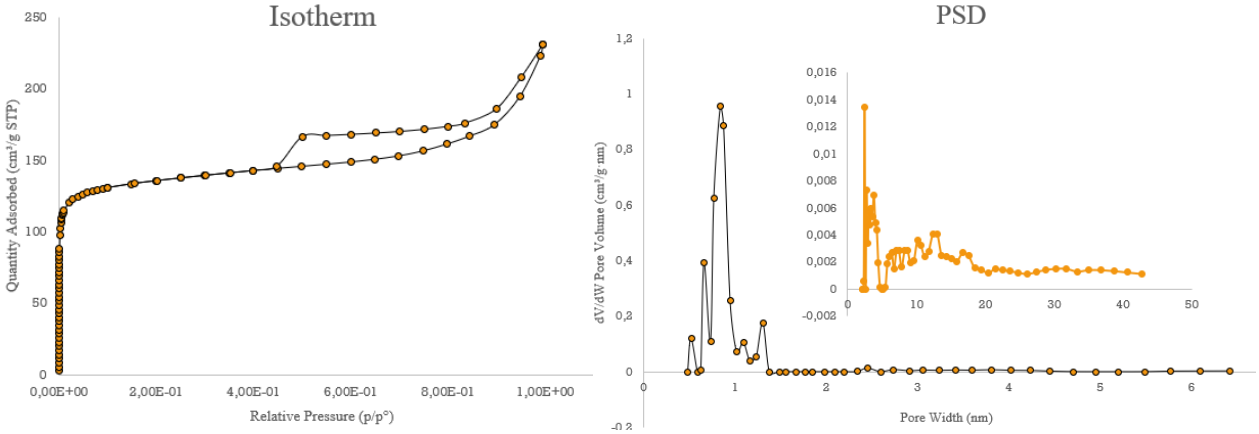

K-Sn-H-Y-80-DA (580 m^2/g)

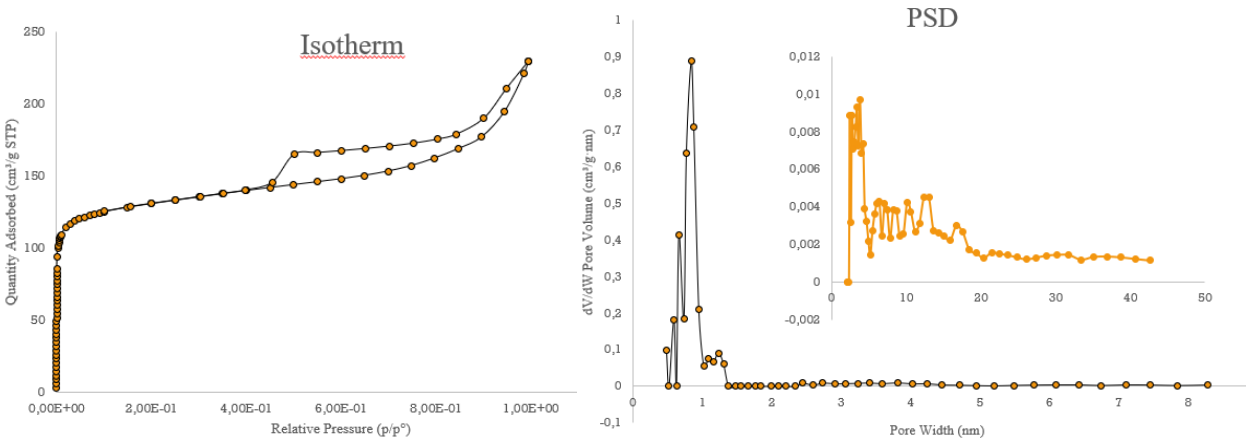

Spent-K-Sn-H-Y-80-DA (510 m^2/g)

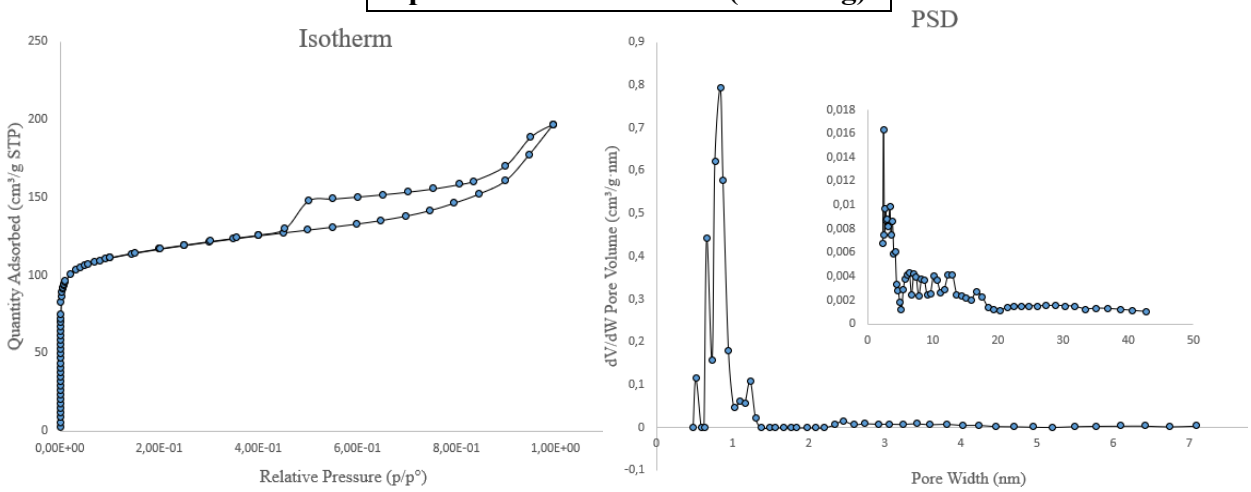

Cs-Sn-H-Y-80-DA (760 m^2/g)

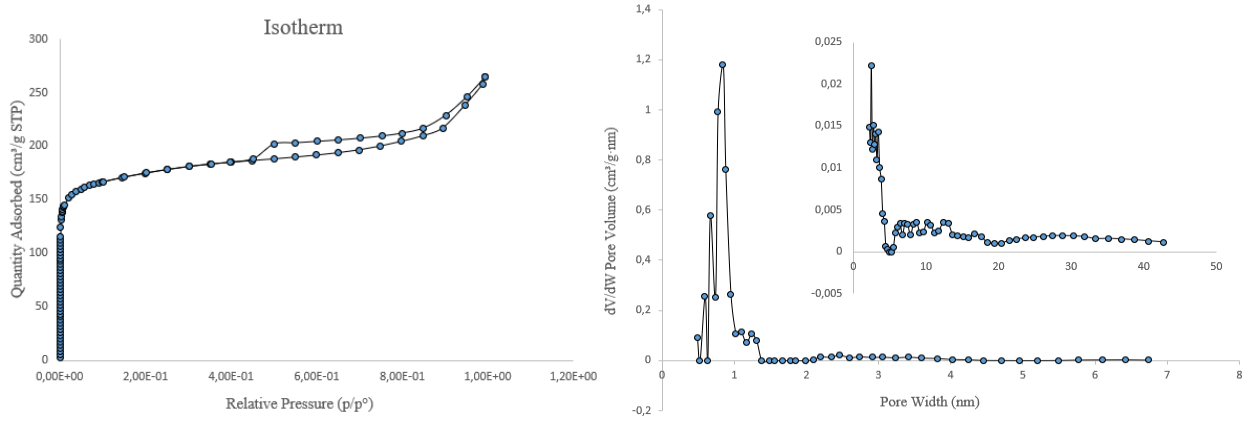

Sr-Sn-H-Y-80-DA (720 m^2/g)

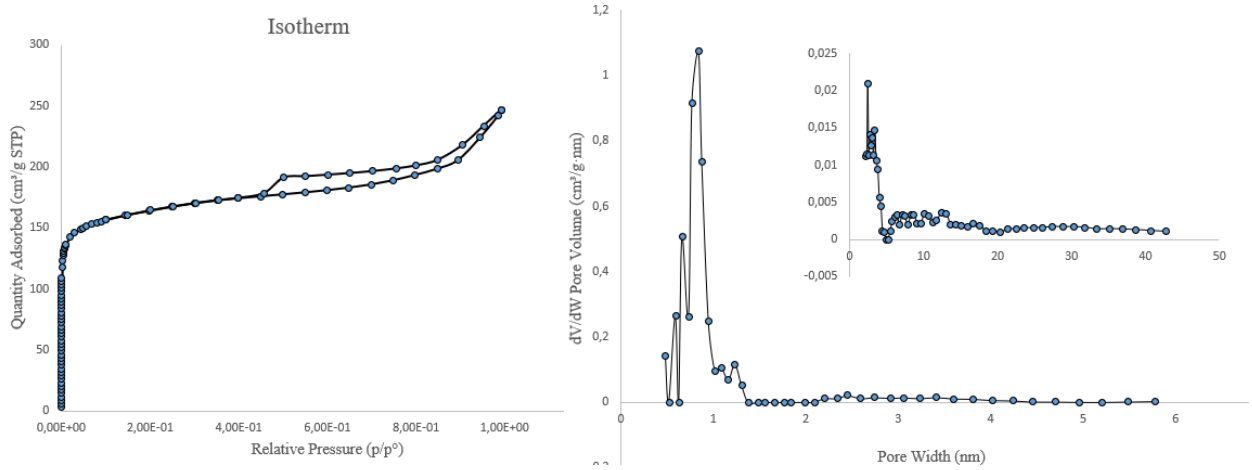

Sn-H-Y-30-EIM (530 m^2/g)

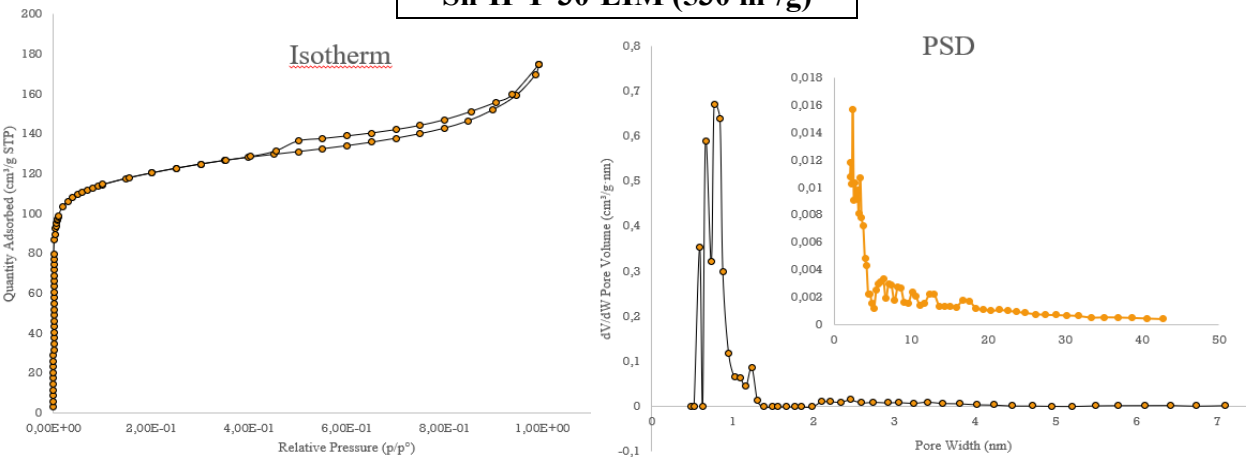

Sn-H-Y-80-EIM (510 m^2/g)

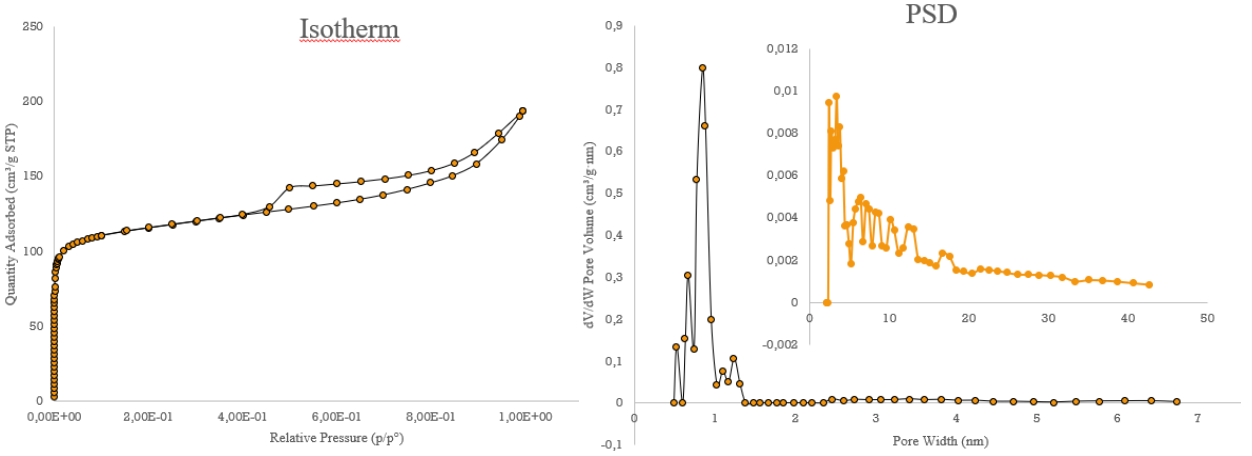

5. Appendix D: The method of extraction

Methanol in 0.2 g of product sample from 24 h reaction was purged by N_2 flow at 50 °C. Then 2 ml of deionized water and 1 ml of dichloromethane (DCM) was added following by shaking for 5 minutes to make sure that the chemicals are homogeneously mixed in the breaker. Furthermore, the beaker was put in cold room for few minutes until the DCM and water phases were separated. Thus, separating DCM phase, the sample was taken from water phase and analyzed on GC.

6. Appendix E: The method of silylation

Methanol in 0.1 ml of product sample from 24 h reaction was purged by N_2 flow at 50 °C followed by further evaporation in Heraeus equipment for 20 mins. Afterwards, 100 µm of internal standard (BSTFA), 20 µl of trimethylclorosilane (TMCS) and 20 µl of pyridine was added followed by mixing until the chemicals are uniformly distributed within the solution. Furthermore, the solution was kept in an oven for one hour at 70 °C, then the sample was taken and analyzed in GC and GC-MS.